THREE-DIMENSIONAL THERMAL ANALYSIS OF HEAT SINKS WITH CIRCULAR MICROCHANNELS

BY

CHRISTOPHER J. KROEKER

A Thesis
Presented to the Faculty of Graduate Studies
In Partial Fulfilment of the Requirements for the Degree of

MASTER OF SCIENCE

Department of Mechanical and Industrial Engineering
University of Manitoba
Winnipeg, Manitoba

THE UNIVERSITY OF MANITOBA

FACULTY OF GRADUATE STUDIES

*****

COPYRIGHT PERMISSION PAGE

THREE-DIMENSIONAL THERMAL ANALYSIS OF HEAT SINKS WITH CIRCULAR MICROCHANNELS

BY

Christopher J. Kroeker

A Thesis/Practicum submitted to the Faculty of Graduate Studies of The University

of Manitoba in partial fulfillment of the requirements of the degree

of

Master of Science

ABSTRACT

Hydrodynamic and heat transfer characteristics of fluid flow through heated microchannel heat sinks are analyzed. Developing fluid flow and heat transfer in the microchannel are assumed, and are modelled in three dimensions throughout the heat sink. Fluid flow is laminar and incompressible throughout the channel, and constant heat flux is applied at the outer surface of the microchannel heat sink. All other outer boundaries are adiabatic. The conventional Navier-Stokes equations and energy equations are solved using CFX-TASCflow: a computer code which uses a finite volume method of solution and is based on a finite element approach for representing the geometry. The main focus of this thesis is on obtaining overall thermal resistance of heat sinks with varying geometries, thermal conductivities, and Reynolds numbers. Results for the axial variation of fluid heat input and fluid bulk temperature, the angular distribution of fluid heat flux, isotherm plots in the heat sink solid, and heat sink surface temperature are also presented. Dimensionless parameters are derived to facilitate presentation of all results in a generalized format.

Results are obtained for thirty-six different cases which consist of models with three different microchannel separation distance to diameter ratios (1.2, 1.6 and 2), three different heat sink height to diameter ratios (2, 3 and 4), two different heat sink solid thermal conductivities to fluid thermal conductivity ratios (668.3 and 247.9), and two different Reynolds number cases (500 and 1000). Water is the working fluid ($Pr \approx 7$) for all cases, all channels are equidistant between the top and bottom heat sink surfaces, and the length to diameter ratio is fixed at 20 for all cases. The microchannel heat sink design

parameters of preferred constant surface temperature and minimal temperature variation throughout the heat sink are used to further evaluate the effect of varying the geometry, Reynolds number, and heat sink thermal conductivity. A brief comparison of rectangular and circular microchannel geometries with respect to thermal performance and pumping power is also presented.

Varying the microchannel separation distance to diameter ratio was found to have the largest impact on the overall heat sink resistance with the lowest values producing the lowest resistance. Increasing the Reynolds number also significantly reduced the overall thermal resistance in the heat sinks. Changing the height to diameter ratios marginally changed the overall thermal resistance. Increasing the heat sink height to diameter ratio, the separation distance to diameter ratio, and the thermal conductivity produced lower temperature variation at the top heat sink surface and in the overall solid in the axial (flow) direction. Reynolds number was found to have a negligible effect on the heat sink surface and overall temperature variation.

Heat sinks with rectangular microchannels were found to have less overall thermal resistance than circular microchannels under conditions of equal hydraulic diameter and equal mean velocity. The overall thermal resistance in the rectangular microchannels also decreased with increasing aspect ratio. However, the pumping power required for rectangular microchannel heat sinks was consistently higher than that required for circular microchannel heat sinks. Circular microchannel heat sinks allowed more heat transfer per unit pumping power than rectangular microchannel heat sinks.

ACKNOWLEDGEMENTS

I would like to thank Dr. Scott Ormiston and Dr. Hassan Soliman for their invaluable help with all aspects of this thesis as well as with my graduate coursework. I would also like to thank Dr. Cyrus Shafai for his participation on the examining committee. This thesis would not have been possible had it not been for my loving wife and family's understanding and unwavering support throughout. Thank you to Him through whom all things are completed.

TABLE OF CONTENTS

List of Figures

LIST OF TABLES

NOMENCLATURE

A	area [m^2]
B	width of cross-sectional cell containing one microchannel [m]
C_p	specific heat [J/kg•K]
D	diameter of microchannel [m]
f	friction factor defined by Eq. (5.3)
H	thickness of heat sink [m]
k	thermal conductivity [W/m•K]
L	length of heat sink [m]
$\dot{m}$	mass flow rate [kg/s]
N	node location along microchannel heat sink in axial (flow) direction with N = 1 for the inlet and N = (final mesh seed plus one) for the outlet
Nu_z	local Nusselt number as defined by Eq. (5.8)
P	dimensionless pressure defined by Eq. (3.7c)
p	pressure [Pa]
Pr	Prandtl number defined by Eq. (3.7d)
P_{WR}	pumping power [W]
q	input heat flux [W/m^2]
q_z	heat rate gained by coolant per unit length [W/m]
$R_{t,out}$	overall thermal resistance as defined by Eq. (5.5)
Re	Reynolds number defined by Eq. (3.7d)
S	distance between centreline of microchannel and heated top surface
T	temperature [K]
U	dimensionless velocity component in the x direction defined by Eq. (3.7b)
u	velocity component in the x direction [m/s]
V	dimensionless velocity component in the y direction defined by Eq. (3.7b)
v	velocity component in the y direction [m/s]

W dimensionless velocity component in the z direction defined by Eq. (3.7b)

w velocity component in the z direction [m/s]

X dimensionless Cartesian coordinate defined by Eq. (3.7a)

x Cartesian coordinate [m]

Y dimensionless Cartesian coordinate defined by Eq. (3.7a)

y Cartesian coordinate [m]

Z dimensionless Cartesian coordinate defined by Eq. (3.7a)

z Cartesian coordinate [m]

Greek Symbols

α aspect ratio as defined by Eq. (6.18)

Γ overall thermal resistance defined by Eq. (6.8) [K/W]

θ dimensionless temperature defined by Eq. (3.7c)

μ dynamic viscosity [$N \cdot s/m^2$]

ρ density [kg/m^3]

φ angle [radians]

Subscripts

b bulk

circle circular microchannel

f fluid

h hydraulic

i interface between solid and fluid

in at inlet of microchannel

m mean value

out at outlet of microchannel

R ratio of copper-water to silicon-water

rect rectangular microchannel

s solid

t thermal

Superscripts

* dimensionless

Chapter 1

INTRODUCTION

Since the pioneering work of Tuckerman (1984), considerable focus has been directed towards the problem of convective heat transfer through microchannels. The impetus for this attention has been the trend for the size of technologies to continuously decrease with continuously increasing heat outputs. For example, as computer-processing power continues to increase, so too does the heat generated from the microchips themselves. The size of microchips continues to decrease due to advances in manufacturing and to produce faster computations. The microchips are sensitive to excessive temperature, and performance will degrade if the thermal energy created is not dissipated at a quick enough rate. Therefore, current computer designs and those in the foreseeable future will benefit from microchannels which remove large amounts of heat from small spaces. Other technologies that require large amounts of heat removal from the smallest possible footprint include fuel cells, air conditioning, and biotechnologies.

The problem of microchannel heat exchanger analysis is still relatively new, thus major landmarks are still being made, albeit difficult to identify them (Kandlikar and Grande, 2003). Generally, however, microchannel analysis and design began in the early 1980's with the continuation of increased computer processing power and therefore heat output. Early research included pressure drop measurements through microchannels, measuring the effects on performance of various microchannel geometries, and measuring the effects on performance of changing flow rates through the channels. Towards the 1990's, computer models were used to predict microchannel heat sink behavior.

As computer models were employed, a debate ensued about the appropriate mathematical model to be used. Results obtained using computer codes based on the classic Navier-Stokes equations for fluid flow seemed not to match experimental data. Various mathematical models were used to try to more accurately predict microchannel heat sink performance, including coarse medium models and classical fin approximation models. As computer processing power increased, so too has the complexity of computer code-based solutions. Three-dimensional thermal and hydraulic analyses of microchannels became possible. Size effect was investigated numerically, along with two-phase experiments in microchannels.

Of the work that has been done in the past twenty years, the bulk of it has been with rectangular microchannels with data presented dimensionally. To the author's best knowledge, no studies have been completed that give a dimensionless analysis of microchannel performance data, specifically for circular channel geometries. Three-dimensional analyses of heat transfer and fluid flow have been performed on microchannels, but again, only rectangular geometries were explored. No studies have investigated multiple geometry effects on circular microchannel thermal performance.

The goal of this work is to use a numerical code to generate thermal and hydraulic data from numerous circular microchannel heat exchanger geometry cases and to present a dimensionless analysis of the thermal performance. The effects of geometry coupled with the effects of Reynolds numbers and the heat sink thermal conductivity will be presented to show both performance trends and design parameters for circular

microchannel heat exchangers. Rectangular channel performance will also be compared with circular microchannel geometries.

Specifically, water will be used as the working fluid ($Pr = 6.97$), with Reynolds numbers of 500 and 1000, microchannel thickness to diameter ratios of be 1.2, 1.6 and 2, microchannel separation distance to diameter ratios of 2, 3 and 4, and two heat sink thermal conductivity to fluid conductivity ratios of 668.3 and 247.9 (copper/water and silicon/water). An overall look at how these parameters affect surface temperature and other microchannel thermal aspects will also be analyzed to aid in heat sink design.

Chapter 2

LITERATURE REVIEW

2.1 Overview

This literature review presents the latest developments in single-phase three-dimensional rectangular microchannel heat sink analyses, single-phase circular shaped microchannel experiments, and single-phase size effect analyses. Two-dimensional analyses of microchannels have been performed; however, this review will focus mainly on three-dimensional analyses. This review will also show the natural progression from existing research to the research presented in this thesis.

2.2 Three-Dimensional Rectangular Microchannel Analyses

Fedorov and Viskanta (2000) presented an analysis of a heat sink with rectangular microchannels. Both the thermal and hydraulic analyses were completed in three-dimensions using a computer algorithm that solved the Navier-Stokes and energy conservation equations. A three-dimensional analysis was used because completely developed flow was not assumed at the inlet. This fact is important in microchannels since the developing region can represent a considerable portion of the entire microchannel due to the characteristic short lengths of microchannel heat sinks. Only one geometry was used for the entire experiment, and it was based on the Kawano et al. (1998) experiments. Fedorov and Viskanta (2000) presented the bulk of their data (i.e., friction coefficients, isotherms, distances, heat fluxes, bulk temperatures, and heat flux coefficients) in dimensional format.

Fedorov and Viskanta (2000) found that their hydraulic and thermal computer model predictions were very close to experimental results (see Figures 5.9 and 5.10). The largest discrepancy was observed in the fluid analysis at low Reynolds numbers (i.e., less than 100). As the hydraulic diameter for this experiment was on the order of 87 micrometers, one can conclude that the Navier-Stokes equations are valid for this size of microchannel and higher to predict both thermal and hydraulic characteristics of microchannel heat sinks.

Qu and Mudawar (2002) used the Kawano et al. (1998) geometry and performed a similar analysis to that of Fedorov and Viskanta (2000). Again, good agreement between numerically predicted thermal and hydraulic performances and experimental data was achieved. Qu and Mudawar (2002) discovered that the thermal conductivity of the heat sink marginally affected the heat transfer effects of the fluid, however, with decreased thermal conductivity, increased heat sink surface temperature occurred. Further experimentation revealed that an often-used simplified analysis based on fin heat transfer had shortcomings when applied to microchannels, and could result in significant errors in heat transfer predictions. The most significant finding of Qu and Mudawar (2002) was that the temperature in the direction of fluid flow can be approximated as linear in the heat sink solid and fluid regions, except at the microchannel inlet region where very high heat fluxes occur due to the minimal thermal boundary layer. Qu and Mudawar (2002) also reported that higher Reynolds number flows increase the developing region of the microchannel, thus justifying a three-dimensional hydraulic analysis.

Toh et al. (2002) looked at three-dimensional numerical computation of laminar fluid flow and heat transfer in microchannels; however, their analyses were limited to rectangular microchannels. Four different geometries were used but no trending was presented. Their work focused on using a computer code based on the Navier-Stokes equations to successfully predict heat sink thermal and hydraulic behavior. All the hydraulic diameters of the heat sinks involved were less than or equal to 104 micrometers. At the outlets of the microchannels, zero gradient conditions were imposed on not only the temperature, but the transverse velocities as well (fully-developed flow). The transverse velocities of the inlet flows were also assumed to be zero.

2.3 Scale Effects of Microchannels

Scale effects, or relating how the geometry of a microchannel heat sink affects heat transfer and fluid flow, have been investigated as well for mainly rectangular-shaped microchannels.

Ambatipudi and Rahman (2000) looked at how changing the aspect ratio of a rectangular microchannel heat sink affected heat transfer performance. The web thickness between the microchannels and the length of the microchannels were the main parameters that were varied. No variation of the width to height ratio was made, nor was there any variation of total heat sink height to microchannel height variation for all experiments. As the number of microchannels in the heat sink increased (decreased web thickness), the local Nusselt number increased as well. Nusselt numbers were much higher at the channel inlets due to the developing thermal boundary layer. Ambatipudi and Rahman

(2000) also looked at pressure drop through the microchannels while varying channel length to change the Reynolds number (the velocity was kept constant at the inlet for each case).

Gao et al. (2002) examined scale effects on hydrodynamics and heat transfer in a two-dimensional analysis of minichannels and microchannels. Their experiments were concerned with accurately predicting Nusselt number using a two-dimensional analysis apparatus (the single microchannel width was much greater than microchannel height) based on experimental results obtained with their apparatus. Only the height of the rectangular microchannel was varied for all experiments while the width remained constant which created different aspect ratios. Gao et al. (2002) concluded that explaining their findings was difficult as their predictions for local Nusselt number varied significantly from theoretical values. Measured Nusselt values were much lower than theoretical values at small microchannel heights.

A numerical optimization of the thermal performance of a microchannel heat sink was presented by Ryu et al. (2002), and again, only rectangular microchannels were analyzed. The flow was assumed to be hydrodynamically fully developed, and the aspect ratio of the microchannels was fixed at 10 and was not varied throughout the experiments. Ryu et al. (2002) stressed that thermal entrance effects should not be neglected and that channel width appears to be the most important variable for influencing heat transfer performance. They also indicated that microchannel web thickness has an almost equal significance.

Guo and Li (2003) produced size effect results for circular microchannels. Nusselt numbers were found to be much lower than experimental values due to a one-dimensional model for thermal resistance that assumed no axial heat conduction in the channel wall. The Nusselt numbers changed marginally with increased ratios of channel thickness to channel diameter; however, a numerical solution presented indicated that increasing the channel diameter ratio (increasing the amount of material surrounding the microchannel) increased the Nusselt numbers.

2.4 Circular Microchannel Experiments

The bulk of the experiments and analyses with microchannel heat sinks are based on rectangular microchannels; however, some circular single-phase microchannel heat sink data are available.

Bowers and Mudawar (1994) investigated boiling in minichannel and microchannel heat sinks. Although most of their data were produced with two-phase flow, some data were presented for single-phase, laminar flow through circular heat sinks. No conclusions were drawn for single-phase flow. These data were used for code verification purposes as described later in Chapter 5.

Adams et al. (1998) experimented with single-phase forced convection in microchannels. The microchannel geometry was circular, flow was turbulent, and the main goals were to obtain Nusselt correlations and to analyze microchannel diameter effects for a small

range of diameters. The findings presented were for a microchannel diameter range of 0.102 mm to 1.09 mm, a Reynolds number range of 2600 to 23000, and a Prandtl number range of 1.53 to 6.43. Adams et al. (1998) concluded that heat transfer performance increased with decreasing microchannel diameter and increased Reynolds number. They also reported that Nusselt values obtained experimentally were higher than what traditional Nusselt correlation formulas predicted.

2.5 Concluding Remarks

From the above investigations, it is clear that there exists a significant amount of information on rectangular-shaped microchannels. Circular microchannel experiments and analyses for single-phase flow are relatively rare, possibly due to the popularity of the etching technique used to create microchannels, which is better suited to producing rectangular geometries.

Three-dimensional analyses have been mainly on rectangular geometries. Heat sinks must be analyzed in three-dimensions to avoid significant thermal and hydraulic performance prediction inaccuracies. Developing flow in the channel and three-dimensional heat flow through the solid must be taken into account to capture the physics of the problem.

Significant efforts have been put into scale effect analyses of rectangular microchannel heat sinks. Some studies have concentrated on the microchannel web thickness, and some have concentrated on the aspect ratio of the microchannel, but none has looked at how the

proximity of circular microchannels and the amount of material between the heated surfaces and the circular microchannels affect thermal performance.

The main goal of this thesis is to present new data for circular microchannels, using a three-dimensional analysis to predict both thermal and hydraulic behavior. Specifically, this thesis will show the effects of varying the circular microchannel proximity, the amount of material between the microchannels and the heated surface, the thermal conductivity of the material, and the Reynolds numbers. A secondary goal of this thesis is to analyze circular microchannel strengths and weaknesses in regards to performance compared to those of rectangular microchannels.

Chapter 3

MODEL DESCRIPTION

3.1 Statement of the Problem

The geometry that is the subject of this thesis is that of rectangular heat sinks with multiple circular microchannels running through the entire length. The microchannels are equidistant between the top and bottom surfaces of the heat sink for all analyses. Figure 3.1 shows the geometry of the heat sink with length L and total width B_T.

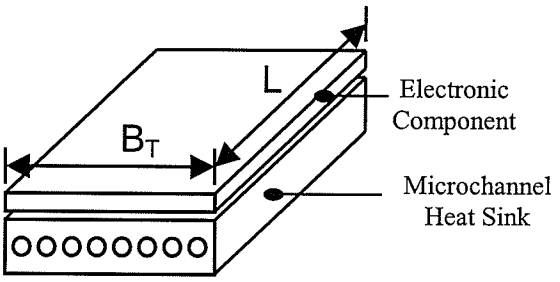

Figure 3.1 Schematic Diagram of Heat Sink

Because of symmetry, the analysis need only to be done on a unit cell, as shown in Figure 3.2. Moreover, x = 0 is also a symmetry plane so that only half of the cell shown in Figure 3.2 needs to be solved. The relevant parameters are height H, unit cell width B, uniform heat flux q'', channel diameter D, and distance from the top surface of the heat sink to the centre of the microchannel S. Coordinates of x and y were assigned to directions along the heat sink width and height respectively. The coordinate z was assigned to the direction along the microchannel length (into the page, not shown).

The fluid flowing through the microchannels was water for all cases studied. Two different heat sink materials were used, copper and silicon (see Appendix A for material

properties), to analyze the effect of varying thermal conductivity in the solid on thermal performance.

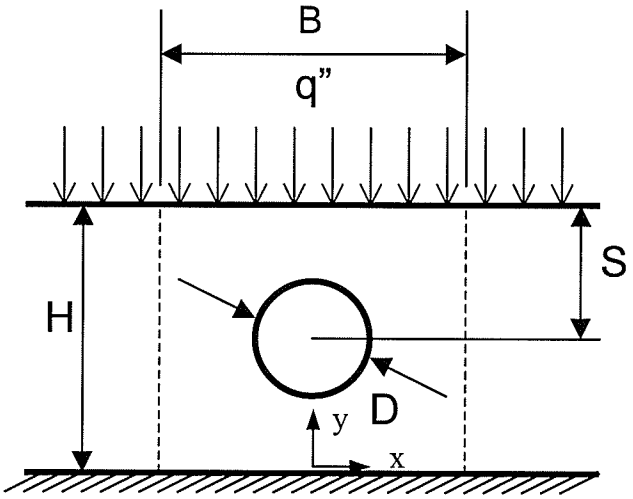

Figure 3.2 Schematic Diagram of a Unit Cell

3.2 Physical Boundary Conditions

Water entering the microchannels had uniform temperature and velocity profiles. The value of the inlet velocity was dependent on the Reynolds number. Physical properties for the water were taken at 290 K and 101.3 kPa.

A uniform heat flux was applied to the entire top surface of the microchannel. The bottom and all other outer boundaries were set to be adiabatic. A section of channel was added to the end of the heat sink to allow for developing flow at the outlet of the channel, and a specified average pressure was applied at the end. The length of this channel ($2L/D$) will be justified in Section 5.1.2.

3.3 Assumptions

- Laminar flow

- Incompressible Newtonian fluid
- Constant physical properties for fluid and heat sink materials
- Negligible viscous dissipation and body forces
- Steady state with respect to time

3.4 Mathematical Model

3.4.1 Governing Equations

Using the assumptions in Section 3.3, the non-dimensional governing equations in the fluid are:

Mass Conservation Equation:

$$\frac{\partial U}{\partial X}+\frac{\partial V}{\partial Y}+\frac{\partial W}{\partial Z}=0 \tag{3.1}$$

Momentum Equations:

$$U\frac{\partial U}{\partial X}+V\frac{\partial U}{\partial Y}+W\frac{\partial U}{\partial Z}=-\frac{1}{2}\frac{\partial P}{\partial X}+\left(\frac{1}{\mathrm{Re}}\right)\left(\frac{\partial^2 U}{\partial X^2}+\frac{\partial^2 U}{\partial Y^2}+\frac{\partial^2 U}{\partial Z^2}\right) \tag{3.2}$$

$$U\frac{\partial V}{\partial X}+V\frac{\partial V}{\partial Y}+W\frac{\partial V}{\partial Z}=-\frac{1}{2}\frac{\partial P}{\partial Y}+\left(\frac{1}{\mathrm{Re}}\right)\left(\frac{\partial^2 V}{\partial X^2}+\frac{\partial^2 V}{\partial Y^2}+\frac{\partial^2 V}{\partial Z^2}\right) \tag{3.3}$$

$$U\frac{\partial W}{\partial X}+V\frac{\partial W}{\partial Y}+W\frac{\partial W}{\partial Z}=-\frac{1}{2}\frac{\partial P}{\partial Z}+\left(\frac{1}{\mathrm{Re}}\right)\left(\frac{\partial^2 W}{\partial X^2}+\frac{\partial^2 W}{\partial Y^2}+\frac{\partial^2 W}{\partial Z^2}\right) \tag{3.4}$$

Energy Equation:

$$U\frac{\partial \theta}{\partial X}+V\frac{\partial \theta}{\partial Y}+W\frac{\partial \theta}{\partial Z}=\left(\frac{1}{\mathrm{Re}\,\mathrm{Pr}}\right)\left(\frac{\partial^2 \theta}{\partial X^2}+\frac{\partial^2 \theta}{\partial Y^2}+\frac{\partial^2 \theta}{\partial Z^2}\right) \tag{3.5}$$

The non-dimensional energy equation in the solid is:

$$\frac{\partial^2\theta_s}{\partial X^2}+\frac{\partial^2\theta_s}{\partial Y^2}+\frac{\partial^2\theta_s}{\partial Z^2}=0 \tag{3.6}$$

Where,

$$X=\frac{x}{D},\quad Y=\frac{y}{D},\quad Z=\frac{z}{D} \tag{3.7a}$$

$$U=\frac{u}{w_m},\quad V=\frac{v}{w_m},\quad W=\frac{w}{w_m} \tag{3.7b}$$

$$P=\frac{p-p_{in}}{\frac{1}{2}\rho w_m^2},\quad \theta=\frac{T-T_{in}}{q''B/k_s} \tag{3.7c}$$

$$Re=\frac{\rho w_m D}{\mu},\quad Pr=\frac{\mu C_p}{k} \tag{3.7d}$$

3.4.2 Boundary Conditions

Heat sink inlet and outlet faces are insulated:

$$\frac{\partial\theta_s}{\partial Z}=0 \text{ at } Z=0 \text{ and at } Z = L/D \tag{3.8}$$

Bottom of the heat sink is insulated:

$$\frac{\partial\theta_s}{\partial Y}=0 \text{ at } Y=0 \tag{3.9}$$

Top of the heat sink has a constant heat flux applied:

$$\frac{\partial\theta_s}{\partial Y}=\frac{D}{B} \text{ at } Y=H/D \tag{3.10}$$

No heat flux across symmetry plane ($X=0$):

$$\frac{\partial\theta_s}{\partial X}=\frac{\partial\theta}{\partial X}=0 \text{ at } X=0 \tag{3.11}$$

No heat flux across symmetry plane ($X=B/(2D)$):

$$\frac{\partial \theta_s}{\partial X} = 0 \text{ at } X = B/(2D) \tag{3.12}$$

Fully developed flow at outlet of additional length of microchannel:

$$\frac{\partial U}{\partial Z} = \frac{\partial V}{\partial Z} = \frac{\partial W}{\partial Z} = \frac{\partial \theta}{\partial Z} = 0 \text{ at } Z = 3L/D \tag{3.13}$$

Velocities at fluid-solid interface are zero:

$U = V = W = 0$ at microchannel wall (3.14)

Continuity of temperature at fluid-solid interface:

$\theta_s = \theta$ at microchannel wall (3.15)

Energy conservation at fluid-solid interface is ensured (conjugate heat transfer solution).

3.4.3 Parametric Dependence

With the dimensionless formulation of the governing equations and boundary conditions shown above, the local values of *U, V, W, P* and θ in the fluid and θ_s in the solid at any location (*X, Y, Z*) are functions of:

Re, Pr, B/D, H/D, S/D, L/D, and k_f/k_s

All of these parameters are varied to study their effects on microchannel heat sink performance, except for *S/D* and *L/D* which are held constant for the scope of this thesis.

To conveniently compare differences between heat sinks with different geometries, the above non-dimensional parameters were derived from the governing differential equations. Other non-dimensional parameters will be obtained that quantitatively show how the heat sink is performing in such areas as axial variation of bulk temperature, heat flux distribution in the fluid along the microchannel, and overall thermal resistance.

Chapter 4

NUMERICAL SOLUTION METHOD

4.1 Introduction

In order to obtain a numerical solution to the governing differential equations, the domain was first subdivided into a large number of small control volumes by creating a computational grid. The governing equations developed in Chapter 3 were then integrated over each volume to derive algebraic equations for the temperature at each node in the solid, and for the velocity components, the pressure, and the temperature at each node in the fluid. The nodes were designated by a numbering scheme, and represented average values for the pressure, temperature, or both for the nodal volume. An iterative solution of the linearized algebraic equations was performed in dimensional form, from which the U, V, W, θ, and P solution fields at all nodal points in the fluid and the temperature field in the solid were obtained.

4.2 CFX-TASCflow v2.11

The numerical solver that was used in this work was CFX-TASCflow 2.11, which is distributed by AEA Technology. All grids were generated with CFX-Build 4.4, which is also distributed by AEA Technology, Engineering Software Division.

CFX-TASCflow uses a finite volume method of discretization (Patankar, 1980), but is based on a finite element approach for representing the geometry. For this study, Cartesian velocity components were used on a structured, non-staggered, multi-block grid.

Mass conservation discretization on the non-staggered grid is an adaptation of earlier techniques developed by Patankar (1980), Prakash (1985), and Schneider and Raw (1987). The discretized mass and momentum conservation equations are fully coupled and they were solved simultaneously using an additive correction multi-grid method to accelerate convergence. Double precision in the iterative computations was necessary to obtain convergence. Each run was considered converged when the sum of the absolute dimensionless residuals of the discretized equations was less than 1.0×10^{-7}.

CFX-TASCflow can be accessed through both a graphical user interface (GUI), and a command line user interface. For each run, the grid generated in CFX-Build was imported into the CFX-TASCflow GUI, and boundary conditions, material properties, and solver parameters were then defined. Some parameter changes were completed using the command line interface. Solver parameters in the CFX-TASCflow parameter file (prm) were modified from the default values and are presented in Appendix B.

4.3 CFX-Build v4.4

CFX-Build v4.4 is a grid generation utility that uses MSC-Patran 9.5 (licensed from MSC Software Corp.) for geometry generation, grid generation, and all GUI functions. It is capable of handling direct computer aided design (CAD) geometry imports, geometry creation and editing, automatic and mapped surface and solid meshing, boundary condition and region definition, and results evaluation.

All geometries were created in CFX-Build and were created with the following basic solid modeling steps:

1. Points were created at the heat sink region endpoints and at the centre block of the channel, all at $Z = 0$ (see Figure 4.1), by defining the x, y and z coordinates of these points in space.
2. Curves were created between points to define edges of heat sink block regions and the centre block of the channel (11 curves). The arcs defining the outside wall of the channel regions were created by rotating points in 45 and 90 degree arcs around a co-ordinate created at the centre of the microchannel (3 arcs, see Figure 4.1). Points were created automatically with the rotate function of the program at the ends of the three new curves. Finally, curves between the arc endpoints and the corners of the center rectangle in the channel and between the arc endpoints and the corners of the heat sink at $X = B/D$ were created to define edges of channel and heat sink quadrilateral regions respectively (4 curves).
3. Surfaces (7 in total) were created by interpolating (extruding) between two opposite sides of each quadrilateral region using adjacent curves as guides.
4. Solids were created (7 in total) by extruding all of the surfaces along the z coordinate.

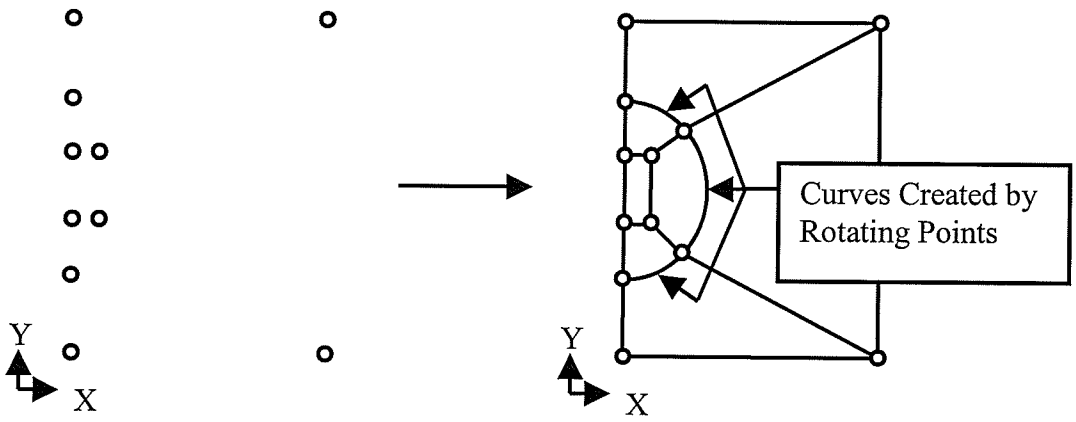

Figure 4.1 Point and Curve Creation of a Microchannel Solid Model

Only node spacings on dimensionally unique edges of the solids were specified since CFX-Build infers the same spacings on corresponding opposite faces of the geometry. For example, node spacings only need to be defined on one edge of the solid in the z direction since all of the other curves in the z direction must have the identical number of nodes to ensure a structured grid. Another example is that for each quadrilateral surface in the x-y plane, nodes only need to be defined on two edges since the opposite edge must have the same number of nodes to ensure a structured grid. If nodes are defined along one edge of a quadrilateral that is adjacent to another, the adjacent quadrilateral nodes on the mating edge will automatically be defined (again to ensure a structured grid). These spacings are used by CFX-Build to define the spacings of all surface and solid meshes throughout the geometry, thus, the initial node spacing specifications are referred to as mesh seeds. Surface meshes (structured two-dimensional elements that overlay all geometry surfaces) were then automatically created using the mesh seed guides, followed by solid meshes using the surface meshes as guides. The solid meshes (structured three-dimensional elements that fill all geometry volumes) were analyzed for negative volumes and proximity, and a final structured mesh was obtained. This mesh was then translated using the "Import CFX-4 Grid" in the CFX-TASClaunch menu into a format compatible with CFX-TASCflow.

After the mesh was created and loaded into CFX-TASCflow, boundary conditions and material properties were assigned, and initial guesses of all of the fields were specified. Finally, the CFX-TASCflow solver was used to obtain solutions to the discretized equations as described above. All of the results generated by the numerical solver were

then viewed, analyzed, and used to calculate relevant performance data, such as Nu_z and fRe (see Chapter 5), using the CFX-TASCtool utility.

Chapter 5

VALIDATION TESTS

5.1 Introduction

To ensure that the results being obtained from the numerical code were accurate, several validation tests were carried out. Data from two different experiments and numerical results for rectangular and circular microchannel heat sinks were compared to those obtained with the present CFD code to understand how well the code predicts the flow phenomena. Mesh independence tests were completed for two extreme heat sink geometries in order to ensure that the final mesh chosen would produce good accuracy. Finally, results obtained for the friction factor and Nusselt numbers in the microchannel are compared with accepted values from the literature (Shah and London, 1978).

5.2 Comparison with Previous Results

5.2.1 Comparison with Experimental Data for Circular Minichannels and Microchannels

Bowers and Mudawar (1994) presented experimental results for boiling two-phase flow in microchannels and minichannels, as mentioned in Chapter 2. Part of their data included single-phase flow, and these data were used in this investigation to examine the ability of the numerical code to predict the thermal performance of circular microchannels and minichannels.

Figure 5.1 illustrates the two geometries used; half of the typical cell was solved due to symmetry. The minichannel and microchannel experiments used 2.54-mm and 0.51-mm diameter channels, respectively, through a 28.6-mm long heat sink. The entire

minichannel heat sink material was copper (see Appendix A for material properties), while the bottom channel portion of the microchannel heat sink was nickel (see Appendix A for material properties). A constant heat flux was applied over a 1 cm centred portion at the top of the heat sink, while all other walls were insulated. The fluid used was R-113 (see Appendix A for material properties) and for our comparison tests flowed at 64 mL/min in total through three minichannels and again at 64 mL/min through 17 microchannels corresponding to Reynolds numbers of 465 and 409, respectively. The fluid entered the channels at 290.35 K, which is 20 K below the saturation temperature corresponding to a pressure of 1.38 bar ($T_{saturation\ @\ 1.38\ bar} = 310.35$ K).

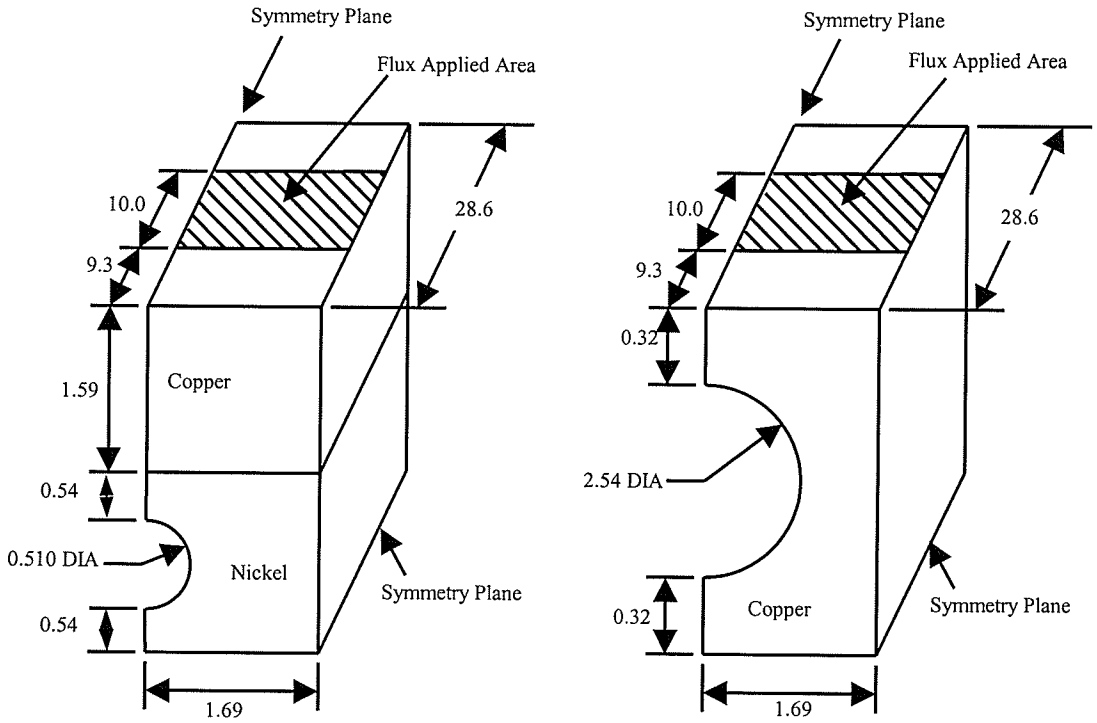

Figure 5.1 Geometries Used in Bowers and Mudawar (1994) Experiments (All dimensions in mm)

Again, because of symmetry, the analysis need only to be done on a unit cell. A section of channel was added to the end of the heat sink to allow for developing flow at the outlet of the channel. The hydraulic entrance length can be estimated using (Incropera and DeWitt, 1996):

$$\left(\frac{z}{D}\right)_{laminar} \approx 0.05\, Re_D \tag{5.1}$$

Calculating the entrance length for the minichannel and microchannel gives us values of 59mm and 10.4mm, respectively. Therefore, it was decided that the additional section of channel added to the end of the heat sink would be 2L, which yields an overall length of 85.8mm which is longer than both of the minichannel and microchannel hydrodynamic entrance lengths. This assumption was further justified by comparing the velocities of the final three points along the centre of the channel in the axial (flow) direction. The values for the minichannel varied by only 0.0008% and by 0.0003% for the microchannel.

The added sections had insulated walls, and had an arbitrary averaged outlet pressure of 0 kPa. Assigning a different pressure at the outlet would have had no effect on the heat transfer or hydrodynamics in the channel save for a different inlet pressure. Two different solids were modeled with the microchannel geometry, copper and nickel (see Appendix A), to match the Bowers and Mudawar experiments as closely as possible.

Mesh independence tests were conducted for both the minichannel and microchannel models. Figure 5.2 outlines the areas where mesh seeds were placed, and Table 5.1 presents the definitions of coarse, medium, and fine meshes. The distance between the

nodes expanded in the direction of fluid flow and contracted towards the walls of the microchannel inside the flow according to the factors also outlined in Table 5.1 where:

$$EndRatio = \frac{\text{Distance Between Last Node and Second Last Node}}{\text{Distance Between First and Second Nodes}} \tag{5.2}$$

An end ratio of 1 indicates uniform grid spacings, while an end ratio of 0.01, for example, indicates contracting grid spacings, with the first grid spacing being 100 times larger than the last grid spacing.

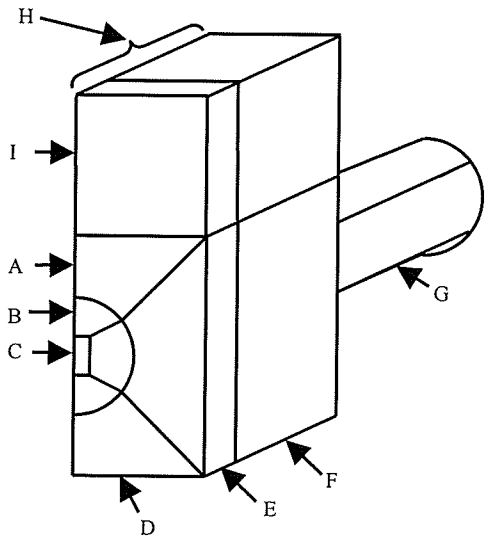

Figure 5.2 Mesh Seed Locations for Bowers and Mudawar (1994) Minichannel and Microchannel (Sections I, E, and F Apply to Microchannel Only, Section H Applies to Minichannel Only)

Figure 5.3 shows the temperature along the top of the circular channel wall in the axial (flow) direction. The medium mesh yields results extremely close to the fine mesh, specifically a θ_s 0.0086% smaller than the fine mesh at the outlet. Figure 5.4 shows the fRe values for the microchannel in the axial (flow) direction, and again, the medium and fine meshes are very similar. The friction factor f is defined by:

$$f = \frac{2 \cdot \Delta p \cdot D}{\rho L w_m^2} \tag{5.3}$$

where Δp is the overall pressure loss across the microchannel, L is the length of the microchannel, and u_m is the mean velocity of the fluid. This equation can be expressed in terms of the dimensionless variables in this work by:

$$f = P_{av}/(4Z) \tag{5.4}$$

where P_{av} is the non-dimensional overall pressure loss across the microchannel using a cross-sectional pressure average. The deviation between the medium and fine meshes has a maximum value of 2.7% at $Z/Re = 0.0001$. Similar mesh-independence results were obtained with the minichannel geometry.

Table 5.1 Grid Spacings for Coarse, Medium, and Fine Grids for Bowers and Mudawar (1994) Minichannel and Microchannel (Refer to Figure 5.2 for Locations)

	Number of Grid Spacings (Mesh Seeds)								
Grid	A	B	C	D	E	F	G	H	I
Coarse	4	25	8	4	N/A	N/A	75	100	N/A
Medium	5	34	12	6	N/A	N/A	100	200	N/A
Fine	6	42	16	8	N/A	N/A	125	300	N/A
End Ratio (Micro)	1	0.1	1	1	N/A	N/A	1	0.01	N/A

Coarse	10	10	8	10	75	150	150	N/A	20
Medium	15	12	12	15	100	200	200	N/A	30
Fine	20	20	20	20	200	300	300	N/A	35
End Ratio (Mini)	1	0.1	1	1	0.01	1	1	N/A	1

Results from the mesh independence tests indicate that the coarse mesh would be acceptable for predicting temperatures in the microchannel heat sink; however, when friction factor data are presented for the coarse, medium, and fine meshes, it is clear that the coarse mesh is unacceptable due to under-predicting the friction factor at small Z/Re values. Therefore, the medium mesh was used for all calculations of the microchannel and minichannel geometries.

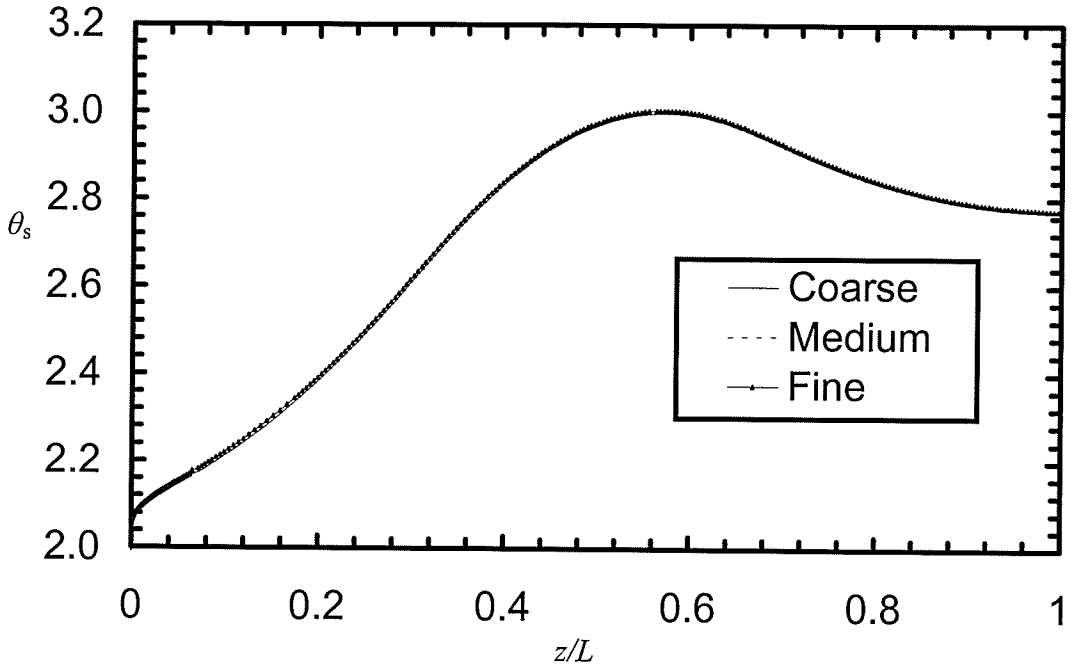

Figure 5.3 Dimensionless Temperature θ_s vs. z/L for Coarse, Medium, and Fine Grids for Bowers and Mudawar (1994) Microchannel Along Top Centre of Channel

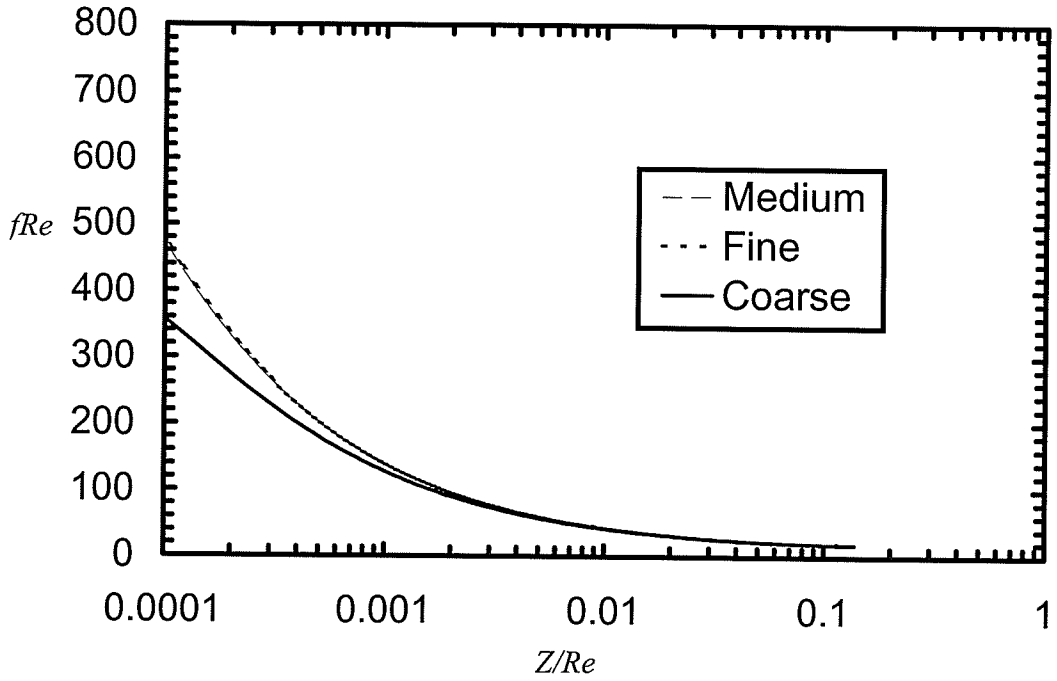

Figure 5.4 Friction Factor *fRe* vs. *Z/Re* for Coarse, Medium, and Fine Meshes for Bowers and Mudawar (1994) Microchannel

Figure 5.5 compares experimental data and numerically predicted results for the Bowers and Mudawar (1994) experiments. The figure shows input heat flux versus the temperature difference between a point on the heat sink located on the top surface and equidistant from all other edges (centre of the heat sink), and the inlet fluid temperature. The numerical results correctly predict the trend of a microchannel heat sink giving better performance (lower temperature rise in the solid) than a minichannel heat sink.

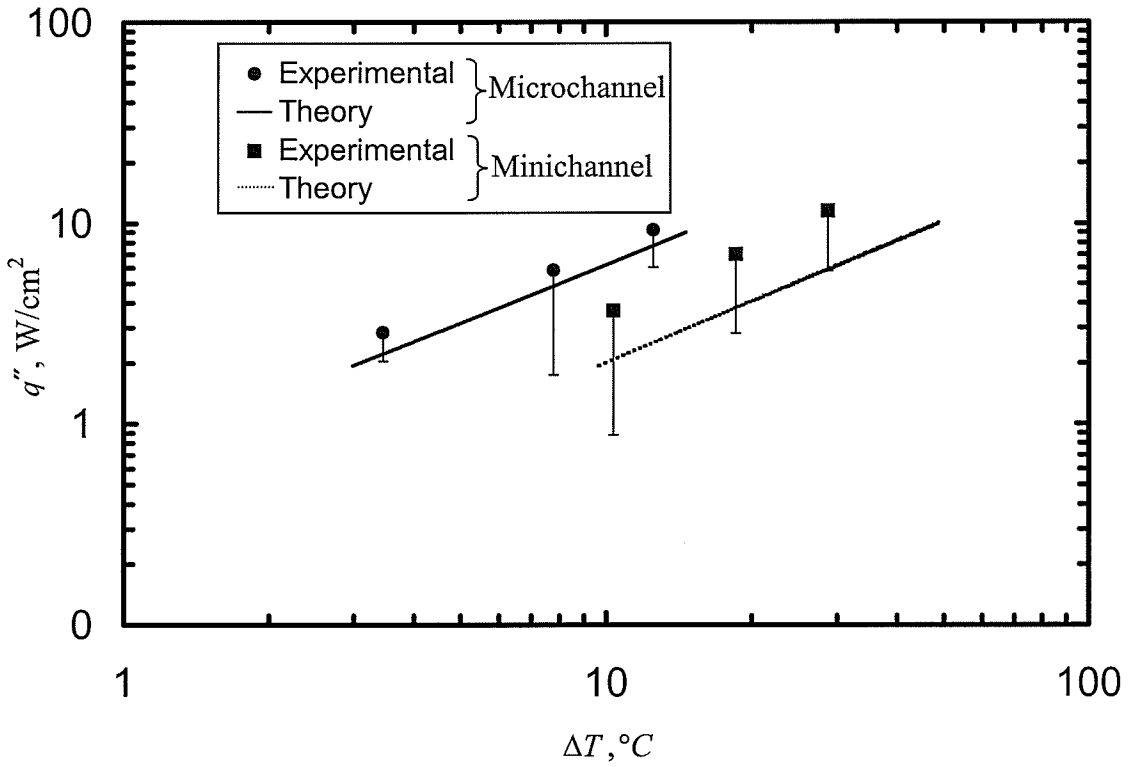

Figure 5.5 Comparison with Bowers and Mudawar (1994)

During a detailed examination of the Bowers and Mudawar (1994) article, a deviation was discovered between the electrical heat input and the sensible heat gained by the liquid. The actual sensible heat gain was calculated from the data presented by Bowers and Mudawar (1994) in their Figure 2(a) for the minichannels and Figure 2(b) for the microchannels. The magnitude of the sensible heat gained by the liquid was found to be

lower than the magnitude of electrical heat input in all cases. For the minichannel heat sink, the deviation was found to be as high as 76% at q" ≈ 4.25 W/cm^2 and it decreased with increasing q" down to 31% at q" ≈ 22 W/cm^2. For the microchannel heat sink the deviation was found to be as high as 80% at q" ≈ 4.9 W/cm^2, however, no trend in the deviation was observed. This information was used in setting the error bars in Figure 5.5.

The present study results in Figure 5.5 under-predict the q" for a given ΔT as defined above specifically by a maximum of 49% for the minichannel and 36% for the microchannel. These under-predictions of q" correspond to higher predicted values of temperature, both in the solid and in the fluid. Temperature over-predictions were also experienced by Fedorov and Viskanta (2000) and Qu and Mudawar (2002). Both parties reported over-predictions in excess of 50% between predicted and measured thermal resistance for rectangular microchannels, specifically at low Reynolds numbers.

The predicted thermal performance curves for both the minichannel and microchannel cases fall within the estimated error bars for the Bowers and Mudawar (1994) data and correlate with trends in at least two other papers, therefore, it was decided that acceptable accuracy for predicting thermal and hydrodynamic performance in circular microchannels can be obtained using the present theoretical approach.

5.2.2 Comparison with Numerical and Experimental Results for a Rectangular Microchannel

To further validate the accuracy of the numerical code, a comparison was made between data obtained experimentally by Kawano et al. (1998) for a heat sink with rectangular

microchannels. Numerical results were also obtained by Fedorov and Viskanta (2000) and Qu and Mudawar (2002) which are also presented here for comparison purposes.

The geometry tested by Kawano et al. (1998) was that of a silicon heat sink (see Appendix A for material properties) consisting of 110 microchannels. A dimensioned unit cell of this geometry is illustrated in Figure 5.6. Water was the working fluid and it entered the heat sink at 293 K (see Appendix A for fluid properties). A heat flux was applied at the top surface of the heat sink and all other exterior boundaries were insulated.

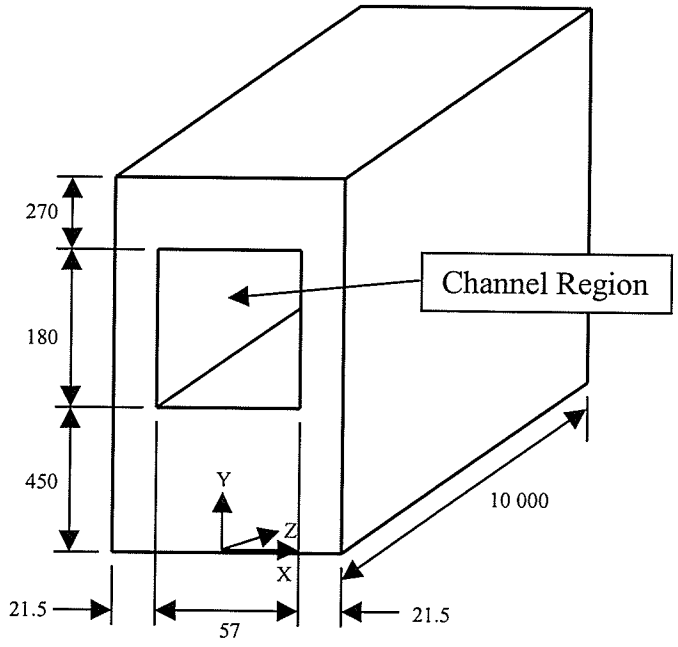

Figure 5.6 Unit Cell from Kawano et al. (1998) Experiments
(All Dimensions in μm, Not to Scale)

Because of symmetry, the problem need only to be modeled on a unit half-cell. Mesh independence was examined using coarse, medium, and fine meshes which are outlined in Table 5.2. Nodes expanded in the direction of fluid flow and contracted towards the walls of the channel inside the channel region according to the factors also outlined in

Table 5.2. All mesh independence tests were done with Re = 140. Arbitrarily, q″ was set at 90 W/cm^2; however, the dimensionless results do not depend on this value. Similar to the previous circular microchannel grids, an extra channel of length 2L was added to the heat sink to allow the developing flow at the heat sink outlet to become fully developed. This added section is roughly 15 times longer than the calculated entrance length of 1.3mm for the highest *Re* tested (300), and in retrospect, probably provided an unnecessary amount of accuracy; however, the 2L length was further justified by comparing the final three values of the maximum velocity at the centreline of the channel in the axial (flow) direction. These final three stations all had the same value.

Table 5.2 Grid Spacings for Coarse, Medium, and Fine Grids for Kawano et al. (1998) Half-Cell

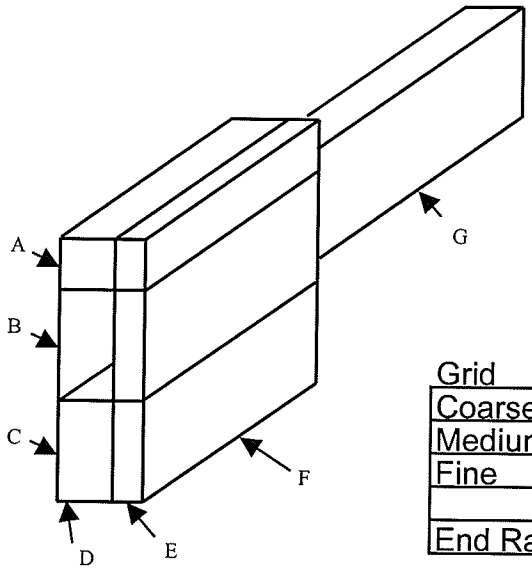

	Number of Grid Spacings (Mesh Seeds)						
Grid	A	B	C	D	E	F	G
Coarse	6	15	8	8	2	150	75
Medium	8	20	10	10	3	200	100
Fine	10	25	12	14	5	300	150
End Ratio	1	0.01	1	0.01	1	100	1

Figure 5.7 shows the dimensionless temperature at the top of the heat sink centred in the axial (flow) direction for the coarse, medium, and fine grids. It is apparent that the medium grid is adequate as the maximum deviation between the medium and the fine values is 0.056% at the outlet. Figure 5.8 shows fRe for the fluid flow in the

microchannel in the axial (flow) direction. While the coarse mesh seems to be adequate for predicting accurate temperatures in the heat sink, the same conclusion cannot be made for predicting accurate pressures in the fluid. The medium mesh appears to be satisfactory as the maximum difference between the fine and medium fRe results is approximately 5% at $Z/Re = 0.001$.

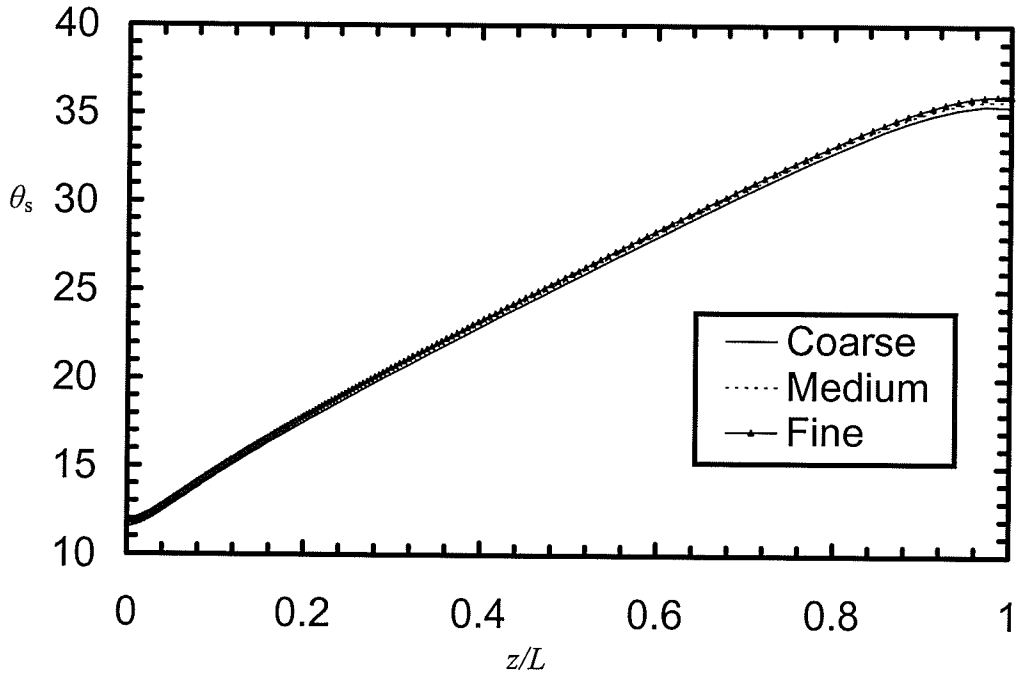

Figure 5.7 Dimensionless Temperature θ_s vs. z/L for Coarse, Medium, and Fine Grids for Kawano et al. (1998) Microchannel Along Top Centre of Heat Sink

Figures 5.9 and 5.10 show plots of $R_{t,out}$ and fRe, respectively, for varying Reynolds numbers with f as defined in Eq. (5.2) (D_h substituted into D), and $R_{t,out}$ defined as:

$$R_{t,out} = \frac{T_s - T_{in}}{q''} \tag{5.5}$$

where T_s is measured at the top surface of the heat sink, at x = 0 at the outlet face. Present results shown in Figures 5.9 and 5.10 exhibit excellent quantitative agreement with Qu and Mudawar (2002), as well as agreement in trend with Fedorov and Viskanta (2000).

All three sets of results are in agreement with the data produced by Kawano et al. (1998) within experimental uncertainty. Figure 5.9 shows a maximum deviation in $R_{t,out}$ occurs at a Reynolds number of approximately 80, with a difference of 18% below results produced by Kawano et al. (1998).

Figure 5.10 shows that a maximum deviation in *fRe* occurs at a Reynolds number of approximately 115 with the presently predicted *fRe* being 5.8% above the value measured by Kawano et al. (1998). Similarly, a maximum variation in $R_{t,out}$ occurs at a Reynolds number of approximately 80, with a difference of 17% above the results produced by Kawano et al. (1998).

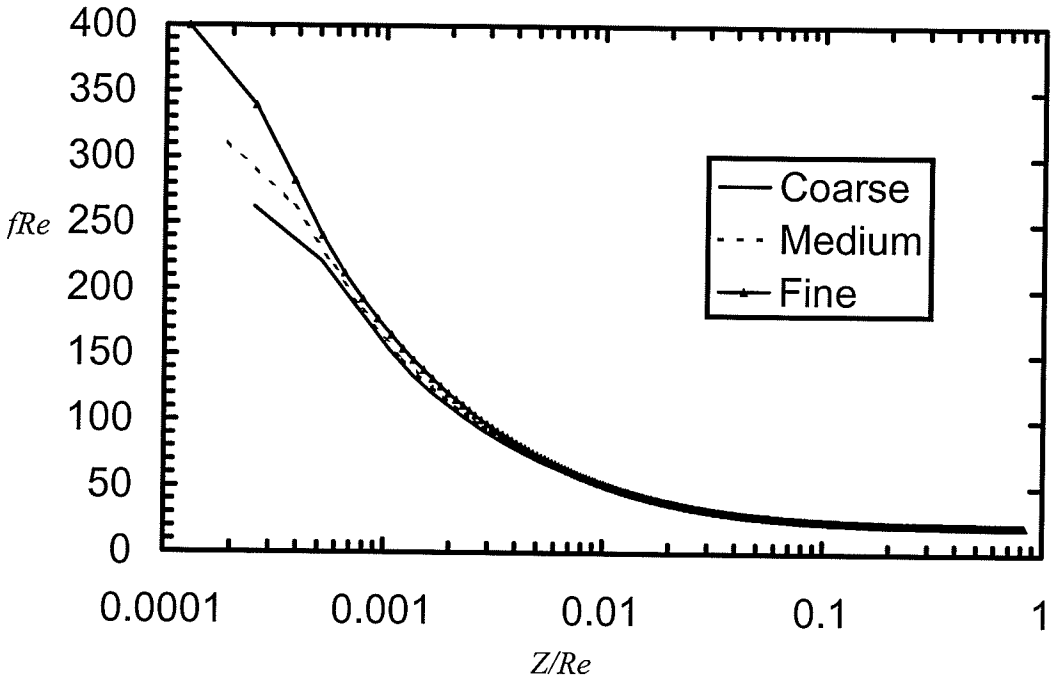

Figure 5.8 Friction Factor *fRe* vs. *Z/Re* for Coarse, Medium, and Fine Meshes for Kawano et al. (1998) Microchannel

It is also interesting to note that Qu and Mudawar (2002) and Fedorov and Viskanta (2000) predict the microchannel bulk temperature along Z differently, as shown in Figure

5.11. The linear result obtained from the code used in this thesis agrees with Qu and Mudawar (2002); however, both Qu and Mudawar (2002) and Fedorov and Viskanta (2000) under-predict the theoretical outlet bulk temperature of 308 K. This temperature can be easily calculated by equating the sensible heat gained by the liquid to the electrical heat input at the top surface, or:

$$q'' A = \dot{m} C_p \left(T_{out} - T_{in}\right) \tag{5.6}$$

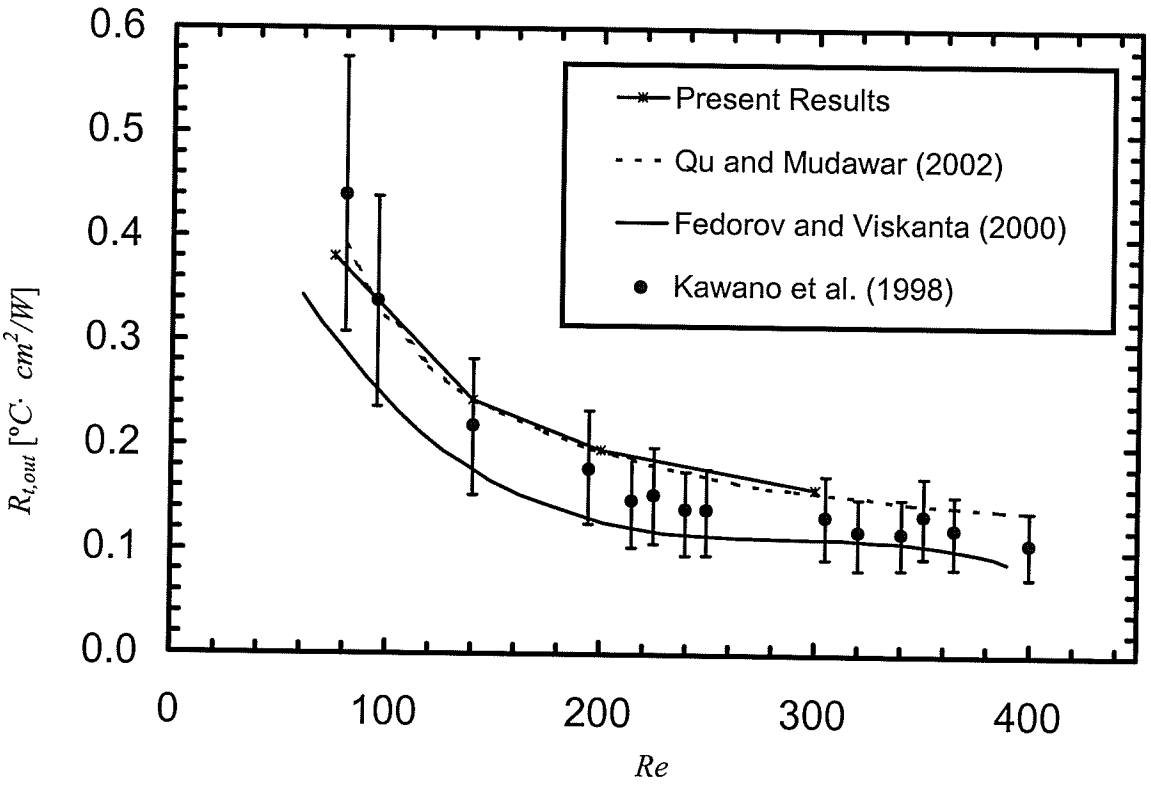

Figure 5.9 Comparison of Overall Outlet Thermal Resistance with the data of Kawano et al. (1998)

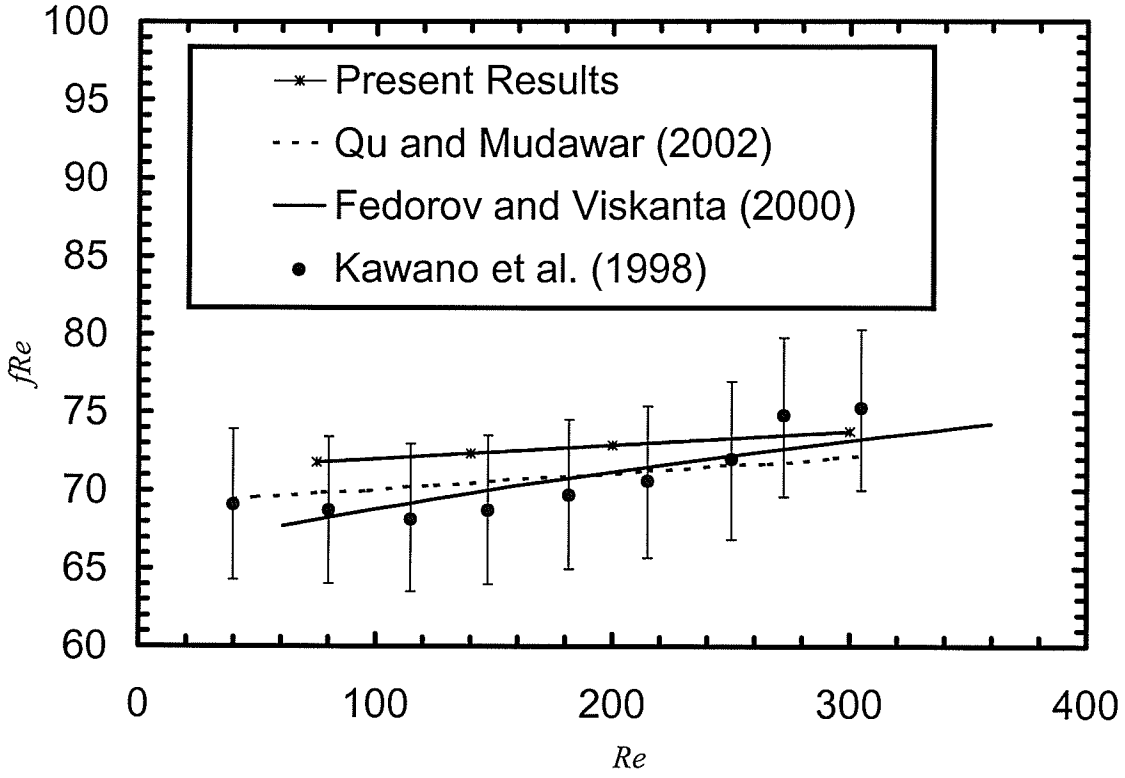

Figure 5.10 Comparison of *fRe* of Kawano et al. (1998) Geometry with Various Solutions

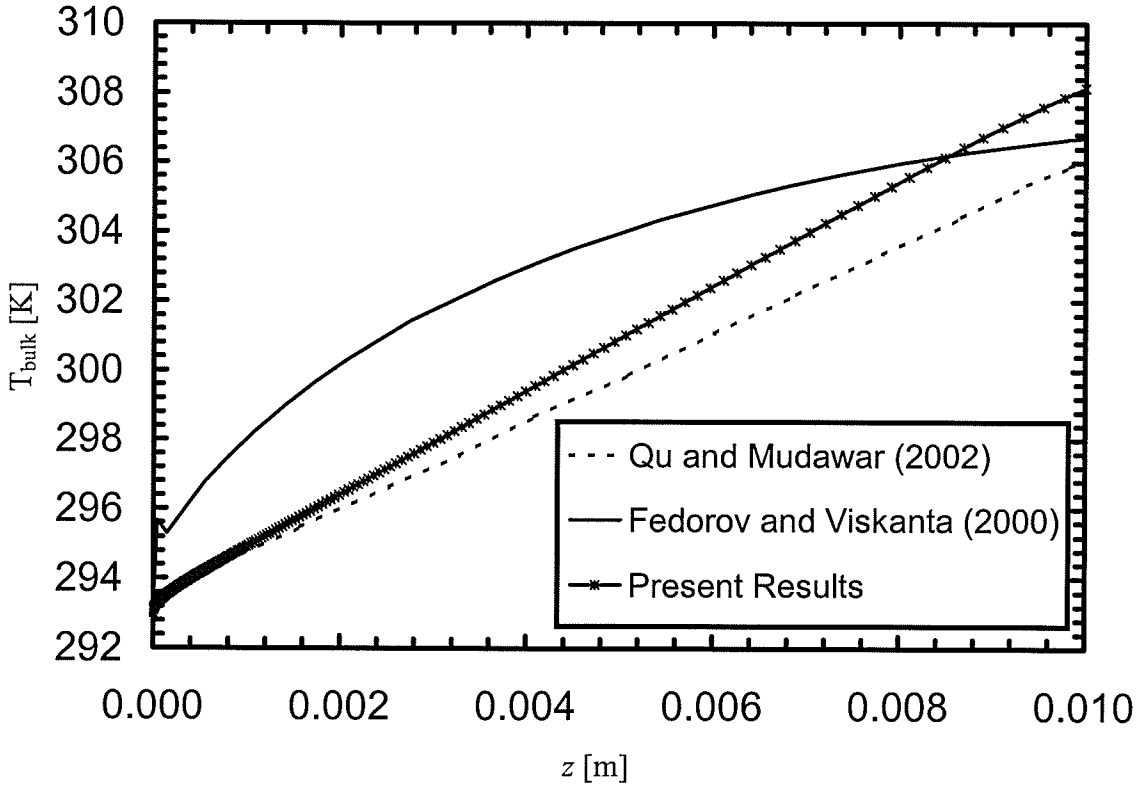

Figure 5.11 Comparison of Bulk Temperature for Kawano et al. (1998) Geometry from Various Solutions

5.3 Code Validation for the Present Geometry

5.3.1 Grid Independence

The geometry of interest in the present investigation is shown in Figures 3.1 and 3.2. The objective of this section is to determine the grid structure that ensures acceptable numerical accuracy. For the purpose of the grid independence tests, two particular heat sink configurations were used. These two configurations correspond to heat sinks with $H/D = 4$ and $B/D = 2$ (largest solid volume) and $H/D = 2$ and $B/D = 1.2$ (smallest solid volume). These tests were conducted with $Re = 500$, $Pr = 6.97$, $L/D = 20$, and $k_s/k_f = 668.3$.

Two dimensionless parameters were used in judging grid independence of the results: θ_s along the top centre of the channel and fRe. By monitoring θ_s, a grid could be selected that ensured the temperatures throughout the solid heat sink and microchannel fluid did not vary with grid size. The grid spacings in the solid were much more coarse than those in the fluid; therefore, if grid independence for θ_s was obtained in the solid, the grid size could be deemed appropriate for predicting temperature in the fluid region due to the consistently smaller meshes in the fluid region. Accurate fluid flow could be assured if the grid size did not affect the fRe values along the microchannel as the value of fRe is strongly dependent upon the velocity profiles and pressures in the fluid.

Table 5.3 shows the variation of grid spacings that define coarse, medium, and fine grids for the present geometries. The definition of the coarse, medium, and fine grids is the same for all independence tests for geometries with largest and smallest volumes. Again,

the distance between the nodes expanded in the direction of fluid flow and contracted towards the walls of the microchannel inside the flow according to the factors also outlined in Table 5.3.

Table 5.3 Grid Spacings for Coarse, Medium, and Fine Grids for Subject Half-Cell Geometry

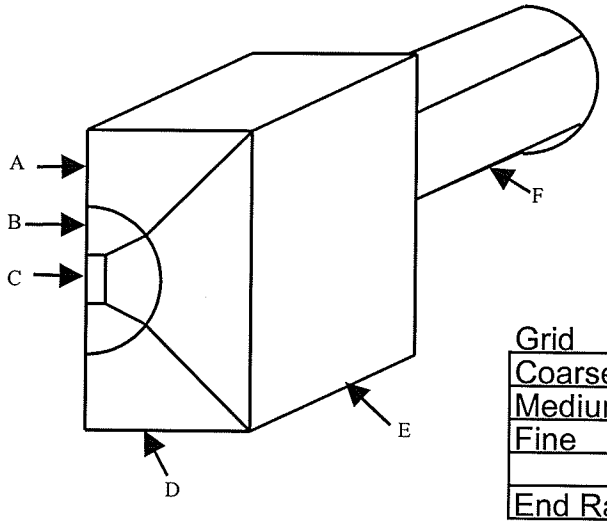

Grid	Number of Grid Spacings (Mesh Seeds)					
	A	B	C	D	E	F
Coarse	5	25	10	4	100	50
Medium	7	34	14	6	200	100
Fine	9	42	16	7	300	125
End Ratio	1	0.1	1	1	100	1

Figures 5.12 and 5.13 show θ_s along the top centre of the channel wall in the axial (flow) direction for the geometries with the largest and smallest solid volumes, respectively, for coarse, medium, and fine meshes. It is clear that the medium and fine meshes overlap for the entire length of the microchannels, thus indicating that the medium mesh is adequate for both cases. The largest deviation in θ_s between the fine and medium mesh results at the microchannel outlet is 0.077% for the largest volume and 0.073% for the smallest volume.

Figure 5.14 shows fRe along the microchannel in the axial (flow) direction for the geometry with the largest and smallest volumes for coarse, medium, and fine meshes. Since Re is identical for both geometries, values of fRe will also be identical. The

medium and fine mesh results do not overlap completely, however the maximum variation between the medium and fine meshes is 4.4% at $Z/Re = 0.0001$.

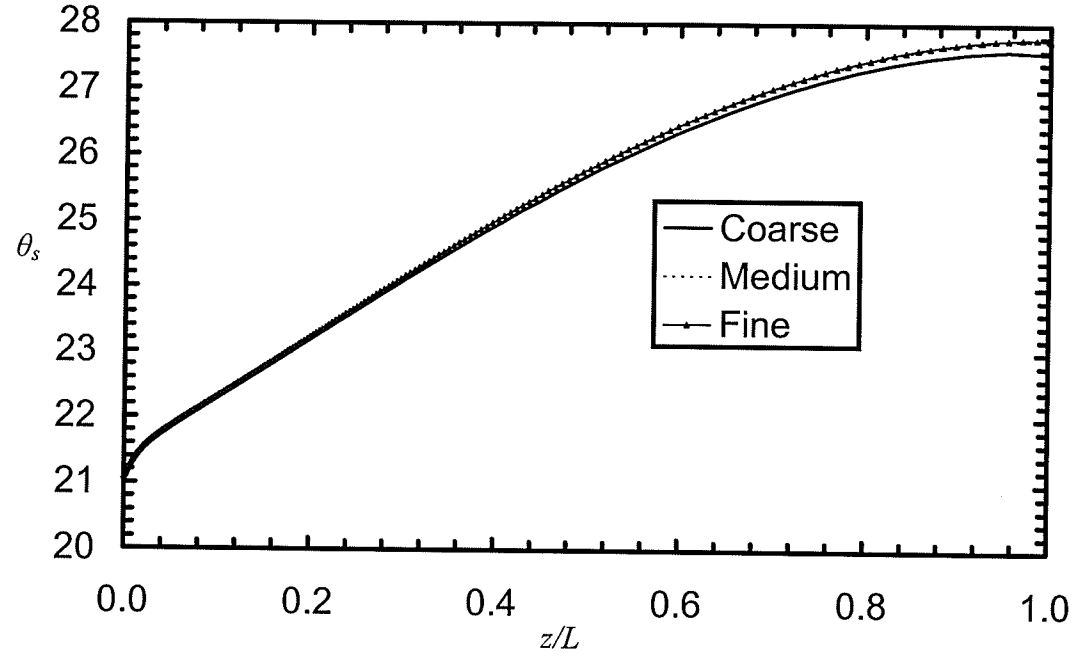

Figure 5.12 Dimensionless Temperature θ_s Along z/L for Coarse, Medium, and Fine Grids for Largest Volume Geometry

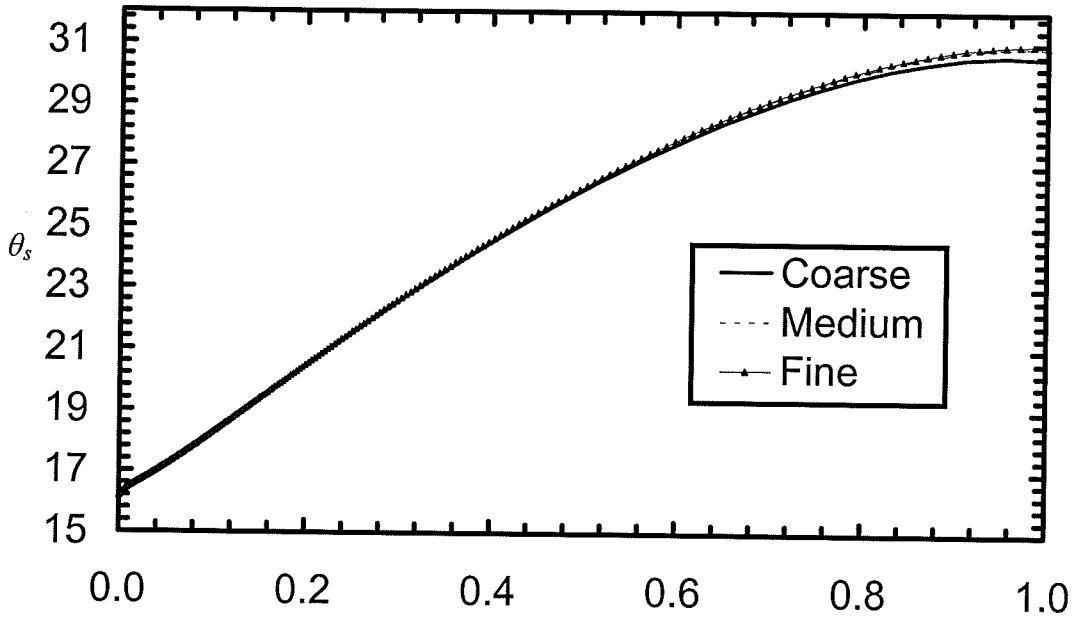

Figure 5.13 Dimensionless Temperature θ_s Along z/L for Coarse, Medium, and Fine Grids for Smallest Volume Geometry

The medium mesh is deemed acceptable for all heat sink configurations due to the relatively low deviations between the fine and medium mesh results for both the θ_s and *fRe* independence tests.

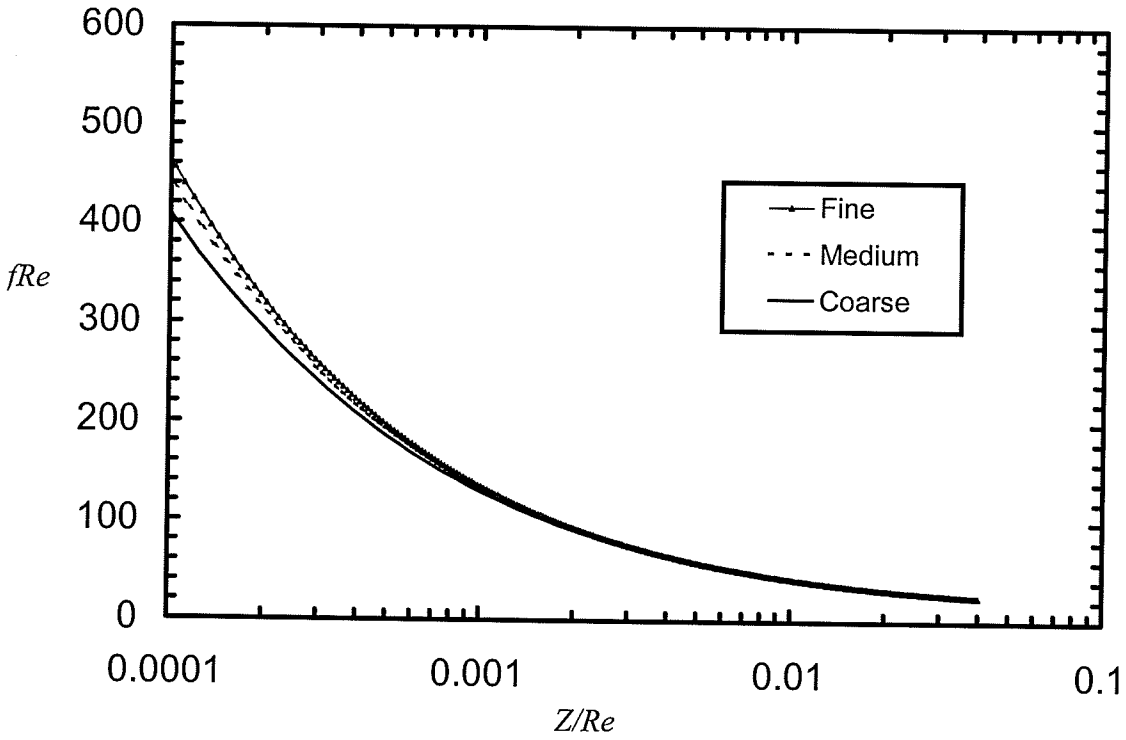

Figure 5.14 Variation of *fRe* Along *Z/Re* for Coarse, Medium, and Fine Meshes for Largest and Smallest Volume Geometries

5.3.2 Detailed Description of the Grid Used for Present Geometries (Medium)

Each grid consisted of eleven different regions: seven in the microchannel heat sink portion, and four in an extended channel section. The extended channel section length was set at 2L which corresponds to a total length that is approximately 17% longer than the calculated entrance length for the highest Reynolds number tested (1000). The length of 2L was further justified by comparing the final three values of the maximum velocity at the centreline of the channel in the axial (flow) direction. These final three stations all had a maximum variation of 0.0009%.

The regions mentioned above are illustrated in Figure 5.15. As shown in Table 5.3, the heat sink solid regions had uniformly spaced meshes in the x-y plane, while the microchannel region had geometrically contracting grid spacings towards the wall. All of the grid spacings expanded in the axial (flow) direction, which is also described in Table 5.3. The heat sink solid consisted of a top region, a side region, and a bottom region.

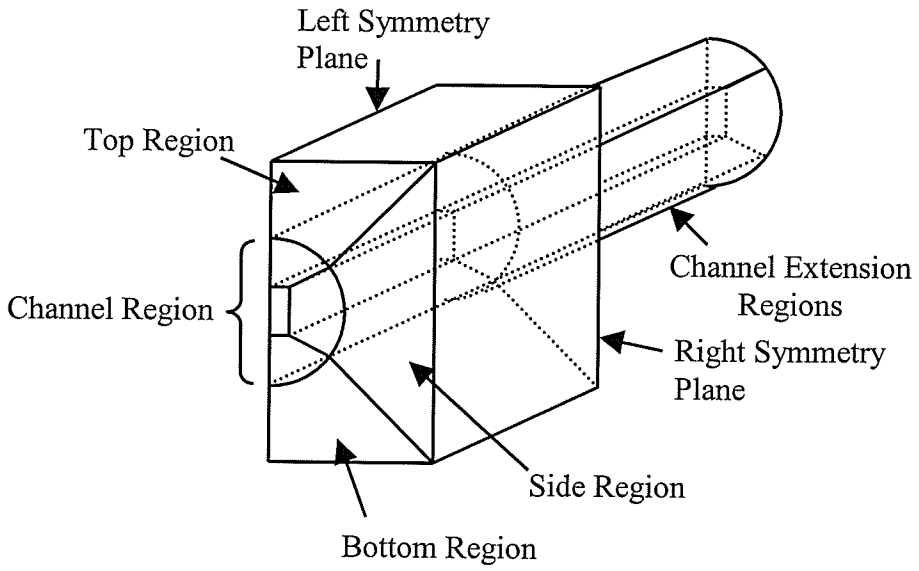

Figure 5.15 Microchannel Grid Regions

Figure 5.16 illustrates the inlet face of the microchannel and heat sink. Both the upper and lower meshes had seven grid spacings in the vertical (y) direction when looking at the left-hand symmetry plane, and six grid spacings along the horizontal (x) direction, perpendicular to this symmetry plane. The side region had seven grid spacings at two sides which matched the seven spacings in the top and bottom regions, and had twelve spacings vertically in the direction of the symmetry planes. All of the heat sink region meshes had 200 grid spacings in the axial (flow) direction which expanded geometrically from the inlet to the outlet with the final spacing being 100 times longer than the first.

The channel portion of the grid consisted of four different regions: top channel, bottom channel, side channel, and centre channel, as shown in Figure 5.17. The centre channel region was rectangular in shape when looking at the inlet face. The height of the rectangle was 0.15mm, and the width was 0.075mm compared to the 0.5mm diameter of the channel. The grid spacings in this rectangular region were uniformly spaced with twelve spacings in the vertical (y) direction, and six in the horizontal (x) direction. The top channel and bottom channel meshes were bounded by the centre rectangular mesh, the wall of the microchannel, the left-hand symmetry plane, and the remaining side channel mesh. Six grid spacings were distributed uniformly in the angular direction, and 34 grid spacings were distributed radially and contracted geometrically towards the microchannel wall with the first spacing being 10 times larger than the last spacing. The side channel region was bounded by the centre rectangle, the microchannel wall, and the two angled boundaries of the top channel and bottom channel regions. Again, 34 grid spacings were distributed radially and contracted geometrically towards the microchannel wall with the first spacing being 10 times larger than the last. All of the microchannel region meshes had two hundred grid spacings in the axial (flow) direction which expanded geometrically, with the final spacing being 100 times larger than the first.

The final three regions of each grid defined the added-on portion to the microchannel which allowed the fluid flow to be developing at the end of the microchannel. The grid spacings in these regions were identical to those in the channel portion in the x-y plane; however, in the axial (flow) direction, there were one hundred uniform spacings.

A total of 1252 two-dimensional elements existed in each cross-section (216 in the heat sink solid and 1036 in the channel), giving a total number of 251 652 three-dimensional elements in each geometry (43 416 in the heat sink solid and 208 236 in the channel).

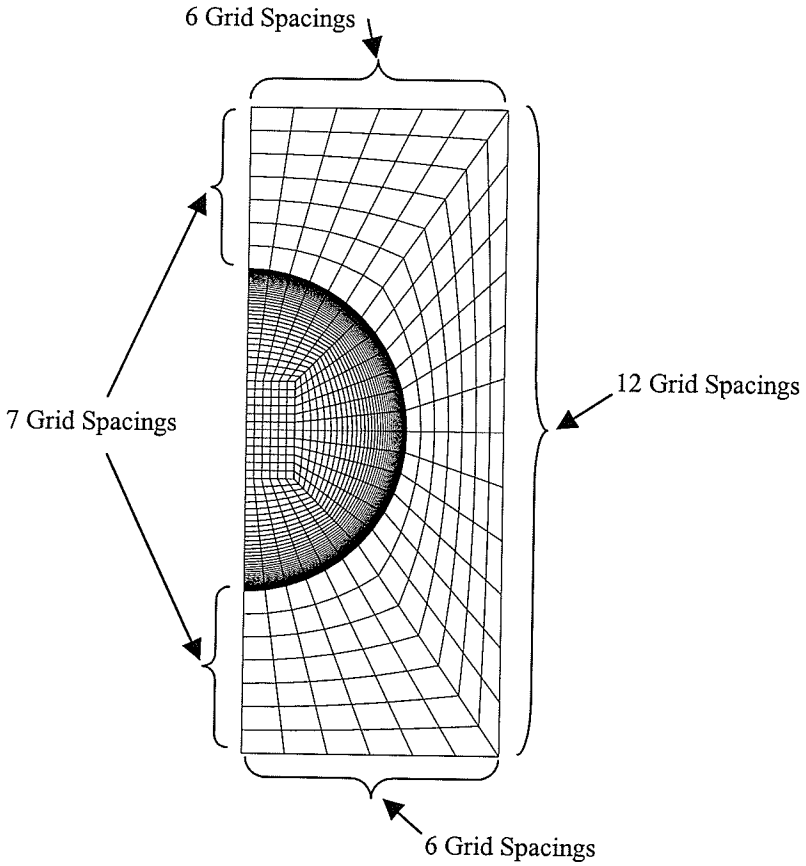

Figure 5.16 Inlet Face of Microchannel and Heat Sink

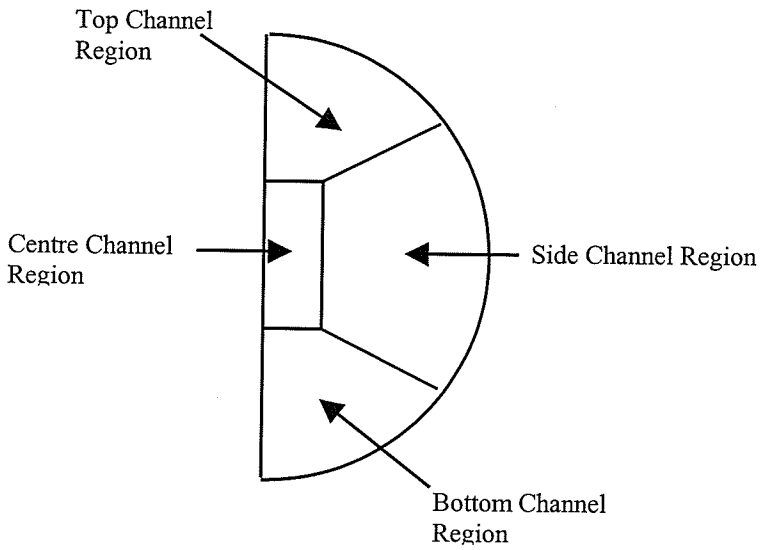

Figure 5.17 Inlet Face of Channel Region

5.3.3 Comparison with Literature Data for *fRe*

Shah and London (1978) outlined a number of different hydrodynamic models for fluid flow in circular channels. The different models adopted different simplifying assumptions and therefore, they produced different results. An equation that was recommended for calculating *fRe* in developing laminar flow in circular tubes is given by:

$$f\,\mathrm{Re} = \frac{3.44}{(Z/Re)^{0.5}} + \frac{16 + \dfrac{1.25}{4(Z/Re)} - \dfrac{3.44}{(Z/Re)^{0.5}}}{1 + \dfrac{0.00021}{(Z/Re)^{2}}} \tag{5.7}$$

This equation was recommended for the entire range of *Z/Re* and *Re* covered in this thesis work.

Shah and London also presented data for *fRe* versus *Z/Re* for developing laminar flow, based on a numerical solution of the complete Navier-Stokes equations. These data are given in Table 5.4.

Table 5.4 Value of fRe as a Function of Z/Re for Laminar Developing Flow in a Circular Duct with Re = 500, as Reported in Shah and London (1978)

Z/Re	fRe
0.0000614	653.6
0.0000946	519.7
0.0001296	434.8
0.0002059	331.8
0.0003387	246.1
0.0005000	194.0
0.0007000	157.9
0.0008625	139.2
0.001056	123.5
0.001579	98.10
0.002167	82.77
0.003076	69.38
0.004019	61.14
0.005000	53.15
0.006610	49.16
0.008165	45.09
0.01050	40.79
0.01439	36.00
0.02217	30.30
0.04550	23.40

Figure 5.18 shows three sets of results for fRe versus Z/Re in a circular duct: Eq. (5.7), Table 5.4, and data obtained numerically for this thesis. The numerically predicted data fall in between the two models and clearly show that the hydrodynamic predictions of the numerical solver are sufficiently accurate.

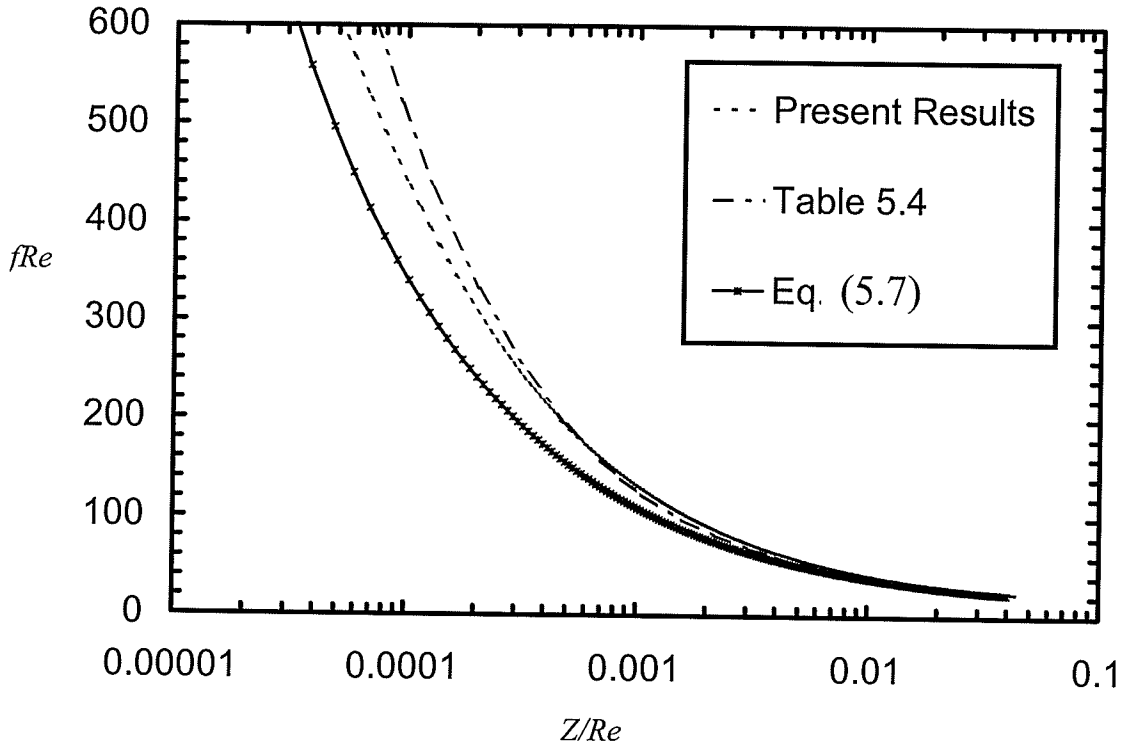

Figure 5.18 Comparison of Predictions for fRe as a Function of Z/Re for $Re = 500$

5.3.4 Comparison with Literature Data for Nu_z

Shah and London (1978) also outlined a number of different thermal models for predicting temperature gradients at the solid-fluid interface in the dimensionless form of Nusselt number in circular channels. The different models adopted different thermal boundary conditions, including constant heat flux on the entire solid-fluid interface and constant temperature on the entire solid-fluid interface. These two conditions lead to the data for Nu_z with varying Z^+ as shown in Table 5.5. The local Nusselt number is defined as:

$$Nu_z = \frac{\overline{q''_{i,z}} \cdot D}{\left(\overline{T_i} - T_b\right)_z \cdot k_f} \tag{5.8}$$

and Z^+ is defined as:

$$Z^+ = \frac{z}{(D \cdot Re \cdot Pr)} \tag{5.9}$$

The data in Table 5.5 (a) are for circular tubes with uniform wall temperature axially and circumferentially, and the data in Table 5.5 (b) are for circular tubes with uniform heat flux axially and circumferentially. Although the present model inlet boundary condition is that of laminar developing flow, these data for fully developed flow are a good approximation since the present case working fluid is water with a value of Pr 7. For Pr = 7, the value of Nu_z for developing flow is very close to the value of Nu_z for fully developed velocity profiles.

For the largest and smallest volumes, Figures 5.19 and 5.20, respectively, show comparisons between the present predictions and the data from Table 5.5. In both figures, the present results exhibit good agreement with the constant wall temperature case. The largest volume case produced a maximum variation below the Table 5.5 (a) data of approximately 5%, and the smallest volume producing a maximum variation of 7% above the Table 5.5 (a) data. The fact that curves for both of the largest and smallest volume cases follow that of Table 5.5 (a) indicates that the boundary condition for most of the solid resembles a constant temperature rather than a constant heat flux.

Owhaib and Palm (2003) studied the heat transfer characteristics of single-phase forced convection through circular microchannels with R-134a as the working fluid and diameters of 1.7mm, 1.2mm, and 0.8mm. They found that the classical correlations for Nusselt number with a constant wall temperature boundary condition were in good agreement with their experimental data in both the turbulent and laminar regions. This

finding suggests further that the microchannel heat sink performance predictions in this thesis are accurate.

5.4 Concluding Remarks

In the above sections the accuracy of the numerical solver and the validity of the problem setup were both tested for accuracy. The numerical solver successfully predicted hydrodynamic and thermal performance data that agreed with existing experimental data for heat sinks with both rectangular and circular microchannels. The code also successfully produced results that matched accepted values of hydrodynamic and thermal performance for circular channels in the form of the product fRe, and Nusselt number, Nu_z. These satisfactory results indicate that the assumptions made to create the governing equations and boundary conditions for each model are valid. Hydrodynamic and thermal results produced from the chosen grid for this thesis did not change significantly with increased resolution and it was therefore deemed accurate. With the numerical solver giving accurate results based on valid governing equations, boundary conditions, and a valid grid, reasonable accuracy of the results can be assumed.

Table 5.5 Nusselt Number Nu_z as a Function of Z/Re for Laminar Fully Developed Flow in a Circular Duct With Re = 500 and (a) Constant Channel Wall Temperature and (b) Constant Wall Heat Flux, as Reported in Shah and London (1978)

(a)

z^+	Nu_z
0.000001	106.538
0.0000015	92.935
0.000002	84.341
0.000003	73.549
0.000004	66.731
0.000005	61.877
0.000006	58.17
0.000007	55.208
0.000008	52.763
0.000009	50.695
0.00001	48.914
0.000015	42.614
0.00002	38.637
0.00003	33.645
0.00004	30.495
0.00005	28.254
0.00006	26.544
0.00007	25.178
0.00008	24.051
0.00009	23.099
0.0001	22.275
0.00015	19.381
0.0002	17.558
0.0003	15.277
0.0004	13.842
0.0005	12.824
0.0006	12.05
0.0007	11.433
0.0008	10.926
0.0009	10.498
0.001	10.13
0.0015	8.8404
0.002	8.0362
0.003	7.0432
0.004	6.4296
0.005	6.0015
0.006	5.6812
0.007	5.4301
0.008	5.2269
0.009	5.0584
0.01	4.9161
0.015	4.4406
0.02	4.1724
0.03	3.8942
0.04	3.7689
0.05	3.71
0.06	3.682
0.07	3.6688
0.08	3.6624
0.09	3.6595
0.1	3.658
0.15	3.6568
0.2	3.6568

(b)

z^+	Nu_z
0.000001	129.203
0.0000015	112.753
0.000002	102.36
0.000003	89.307
0.000004	81.062
0.000005	75.19
0.000006	70.707
0.000007	67.124
0.000008	64.167
0.000009	61.665
0.00001	59.51
0.000015	51.889
0.00002	47.077
0.00003	41.037
0.00004	37.224
0.00005	34.511
0.00006	32.44
0.00007	30.787
0.00008	29.422
0.00009	28.269
0.0001	27.275
0.00015	23.762
0.0002	21.555
0.0003	18.79
0.0004	17.048
0.0005	15.813
0.0006	14.872
0.0007	14.123
0.0008	13.506
0.0009	12.985
0.001	12.538
0.0015	10.967
0.002	9.9863
0.003	8.7724
0.004	8.02
0.005	7.4937
0.006	7.0986
0.007	6.7881
0.008	6.5359
0.009	6.3261
0.01	6.1481
0.015	5.5469
0.02	5.1984
0.03	4.8157
0.04	4.6213
0.05	4.5139
0.06	4.4522
0.07	4.4162
0.08	4.3949
0.09	4.3823
0.1	4.3748
0.15	4.3645
0.2	4.3637

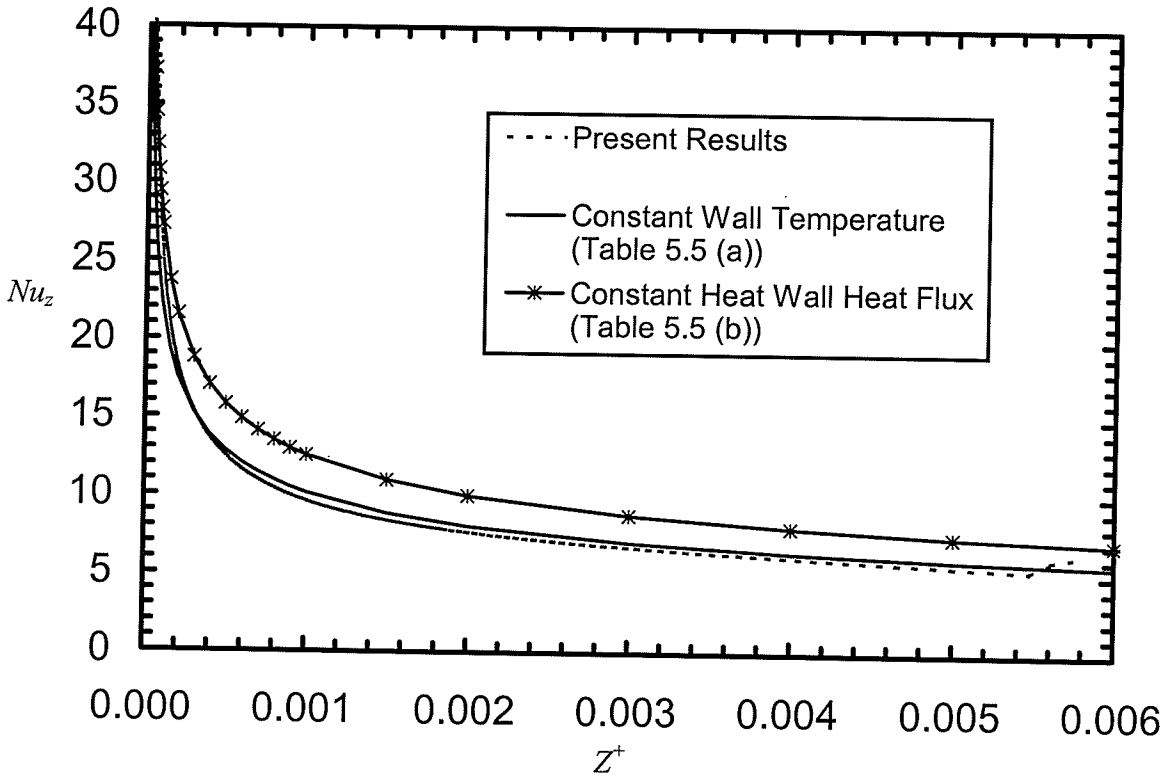

Figure 5.19 Comparison of Predictions for Nu_z Along Z^+ for a Microchannel with $H/D = 4$ and $B/D = 2$ (Largest Volume Case)

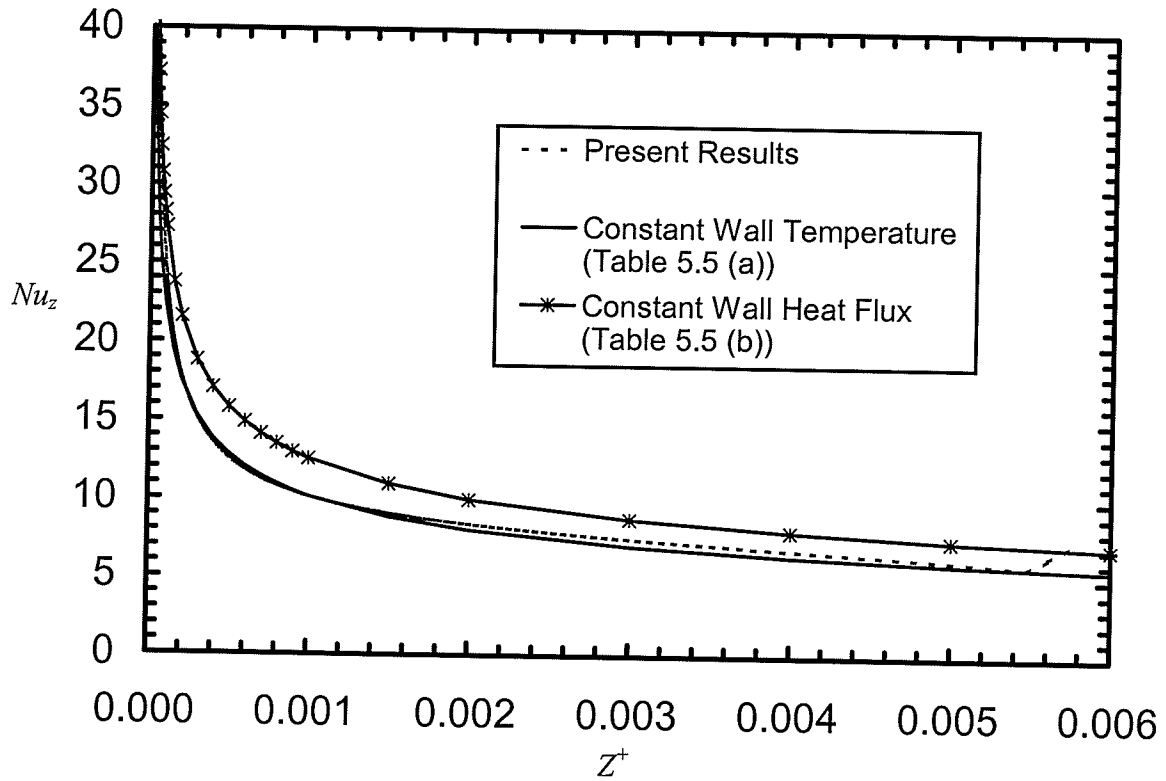

Figure 5.20 Comparison of Predictions for Nu_z Along Z^+ for a Microchannel with $H/D = 2$ and $B/D = 1.2$ (Smallest Volume Case)

Chapter 6

RESULTS AND DISCUSSION

6.1 Introduction and Definitions

This chapter focuses on the effects of geometry, Reynolds number, and solid thermal conductivity on the thermal performance and some important characteristic design features of a heat sink with circular microchannels. A comparison of circular channel heat sink performance with rectangular channel heat sink performance is also presented. The hydrodynamic results are not presented here because velocity and pressure results for single-phase, laminar, developing flow in a pipe have been produced and studied extensively in the past. Accurate predictions of the velocity and pressure correctness are important for proper prediction of temperature distributions, and therefore fRe in the microchannel were examined in Chapter 5 and shown to be of high accuracy.

The effects of geometry were examined by varying the ratios B/D and H/D. The values B/D = 1.2, 1.6, and 2, and H/D = 2, 3, and 4 were considered. The effects of Reynolds number were examined by obtaining results at Re = 500 and 1000. The effects of thermal conductivity were examined by generating results for copper-water (k_s/k_f = 668.3) and silicon-water (k_s/k_f = 247.9). The test matrix with 36 combinations of B/D, H/D, Re, and k_s/k_f is listed in Table 6.1.

An L/D ratio of 20 was used for all cases. Each microchannel centre was placed equidistant between the top and bottom of the heat sink (S/H = 0.5), and the heat sink width to diameter ratio was fixed (B_T/D = 24). All figures in this chapter are for Re = 500 and k_s/k_f = 668.3 (Copper/Water) unless otherwise stated.

Table 6.1 Test Matrix

Case	*H/D*	*B/D*	k_s/k_f	*Re*
1	4	1.2	668.3	500
2	4	1.6	668.3	500
3	4	2	668.3	500
4	3	1.2	668.3	500
5	3	1.6	668.3	500
6	3	2	668.3	500
7	2	1.2	668.3	500
8	2	1.6	668.3	500
9	2	2	668.3	500
10	4	1.2	247.9	500
11	4	1.6	247.9	500
12	4	2	247.9	500
13	3	1.2	247.9	500
14	3	1.6	247.9	500
15	3	2	247.9	500
16	2	1.2	247.9	500
17	2	1.6	247.9	500
18	2	2	247.9	500
19	4	1.2	668.3	1000
20	4	1.6	668.3	1000
21	4	2	668.3	1000
22	3	1.2	668.3	1000
23	3	1.6	668.3	1000
24	3	2	668.3	1000
25	2	1.2	668.3	1000
26	2	1.6	668.3	1000
27	2	2	668.3	1000
28	4	1.2	247.9	1000
29	4	1.6	247.9	1000
30	4	2	247.9	1000
31	3	1.2	247.9	1000
32	3	1.6	247.9	1000
33	3	2	247.9	1000
34	2	1.2	247.9	1000
35	2	1.6	247.9	1000
36	2	2	247.9	1000

The first important design feature for microchannel heat sinks is the variation of the top surface temperature along the heat sink. The top surface of the heat sink is the interface where the object being cooled (usually a microchip) is attached. A surface with a constant temperature is preferable since temperature variations in the heat sink could cause hotspots on the microchip, resulting in damage, failure, or incorrect data. Also, a designer

using a heat sink with a constant surface temperature need not pay attention to chip orientation or placement. However, the present results will show that the top surface temperature increases along the heat sink (in the flow direction) in all cases.

The second design feature that will be used is the temperature variation in the heat sink solid. If the temperature in the solid changes drastically, material stresses will be introduced causing premature mechanical failure of the microchannel. Stresses that occur with each on-off cycle of the fluid, or if the heat sink is restrained on each side, would accelerate a failure of this type. Fedorov and Viskanta (2000) predicted large transverse and longitudinal temperature gradients within the heat sink solid near the inlet of their rectangular channel geometry, and stated that these large gradients create a potential for significant thermal stresses and structural failure of the heat sink.

The dimensionless bulk temperature along the microchannel is defined as:

$$\theta_b = \frac{T_{b,z} - T_{in}}{q'' B / k_s} \tag{6.1}$$

Where $T_{b,z}$ is defined by:

$$T_{b,z} = \frac{\int_0^A wTdA}{w_m (\pi/4) D^2} \tag{6.2}$$

The dimensionless bulk temperature curve has the following fixed values:

$$\theta_b = \theta_{b,in} = 0 \text{ at } Z = 0 \tag{6.3}$$

$$\theta_b = \theta_{b,out} = \frac{\left(\frac{4}{\pi}\right)\left(\frac{L}{D}\right)\left(\frac{k_s}{k_f}\right)}{Re\ Pr} \text{ at } Z = L/D \tag{6.4}$$

The axial distribution of heat input to the fluid is important for studying geometry effects on the heat entering the fluid along the microchannel. Axial distribution plots will show how the heat flows back towards the inlet (referred to as back-heating) due to the smaller thermal boundary layer thickness at this location. Different geometries will create different amounts of back-heating, as well as varied heating along the microchannel. To derive a dimensionless axial heat distribution parameter, begin with an energy balance in the liquid for an axial slice of width *dz*:

$$q_z\, dz = \rho D^2 \frac{\pi}{4} w_m\, C_p\, dT_{b,z} \tag{6.5}$$

where q_z is the heat input to the fluid per unit length at a particular location z. The heat distribution parameter normalizes q_z by the amount of heat added to the solid at the top surface over the same slice to obtain:

$$\frac{q_z}{q''B} = \rho D^2 \frac{\pi}{4} w_m\, C_p \frac{1}{q''B} \frac{dT_{b,z}}{dz} \tag{6.6}$$

which can be written as:

$$\frac{q_z}{q''B} = \frac{\pi}{4} Re \cdot Pr \frac{k_f}{k_s} \frac{d\theta_b}{dZ} \tag{6.7}$$

Ultimately, the overall thermal resistance of the heat sink, or how easily heat is transferred from the heat sink surface to the fluid, is of the most interest. Trends from geometry, Reynolds number, and thermal conductivity changes can easily be seen with

thermal resistances presented with the variation of multiple parameters. The overall thermal resistance (with units of [K/W]) is normally defined as:

$$\Gamma = \frac{\overline{T_s\left(y=H, z=L\right)} - T_{in}}{q'' B_T L} \tag{6.8}$$

The overbar indicates average over x from $x = 0$ to $x = B$. With no change in units, Γ can be written in terms of θ:

$$\Gamma = \frac{B}{k_s L B_T}\left[\overline{\theta_s\left(Y=\frac{H}{D}, Z=\frac{L}{D}\right)}\right] \tag{6.9}$$

A dimensionless form of the overall resistance that can be used to compare heat sinks with different thermal conductivities is:

$$\Gamma^* = k_s L \Gamma = \overline{\theta_s\left(Y=\frac{H}{D}, Z=\frac{L}{D}\right)} \cdot \frac{B}{B_T} \tag{6.10}$$

Heat flux (q_i'') entering the fluid in the microchannel along the wall changes with angle (φ) around the circumference, and changes along the microchannel. The parameter that will be used to present the local heat flux input to the fluid is $\frac{q_i''}{q''} \cdot \frac{\pi}{(B/D)}$, which varies between $\varphi = 0$ (top of microchannel) and $\varphi = \pi$ (bottom of microchannel) at a given axial location.

6.2 Effect of Varying *B/D*

From Figures 6.1 and 6.2 we can see the effect of varying the web thickness between microchannels, or *B/D*. Figure 6.1 shows the axial heat input to the fluid along the microchannel for varying *B/D*, and a fixed *H/D* of 4. The heat sink with a *B/D* of 2

experiences higher back-heating than the heat sink with *B/D* of 1.2. Eventually both heat sinks reach a point where the input heat flux ratio is identical, and can be seen as an intersection on the graph ($Z \approx 6$). For greater than 6, the $q_z/(q'' \cdot B)$ is higher for the lower *B/D* heat sink because the total amount of energy supplied to the heat sink is the same in all three cases.

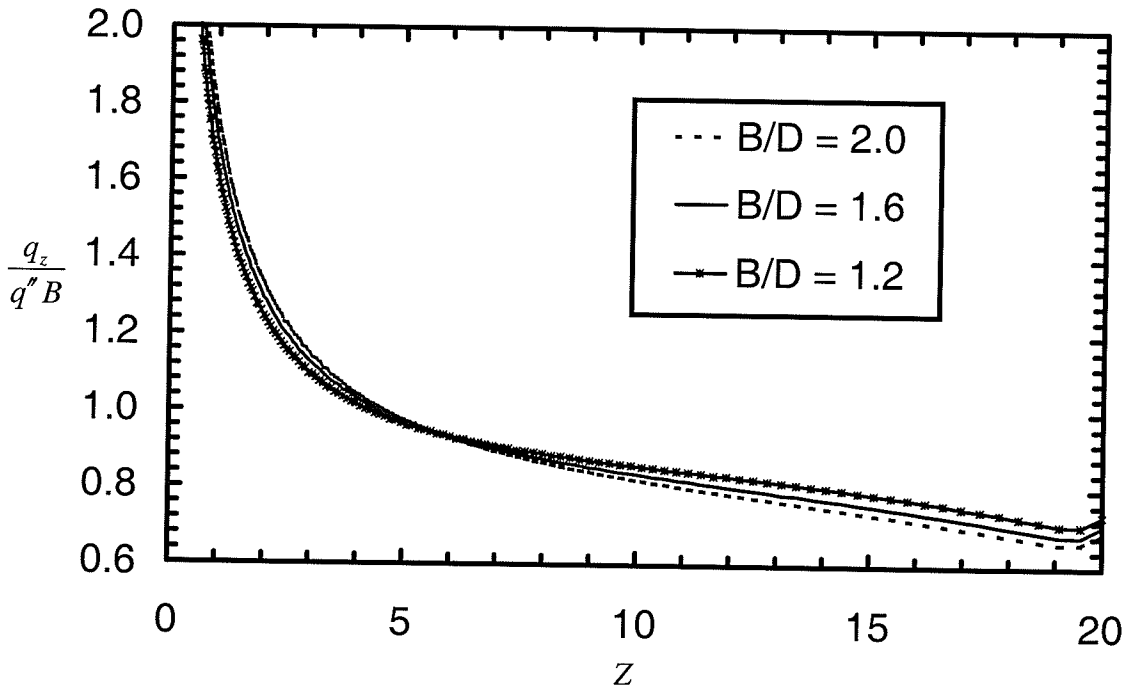

Figure 6.1 Effect of *B/D* on the Axial Variation of q_z for *H/D* = 4

Figure 6.2 shows the dimensionless bulk temperature variation along the microchannel with varying *B/D*. Both the inlet and outlet temperatures are identical (as outlined above in Eqs. (6.3) and (6.4)); however, the intermediate temperatures show variation with *B/D*, specifically that the temperature in the fluid increases with increasing *B/D*. The dimensionless bulk temperature and axial heat input distribution trends were found to be similar for all *H/D* cases tested.

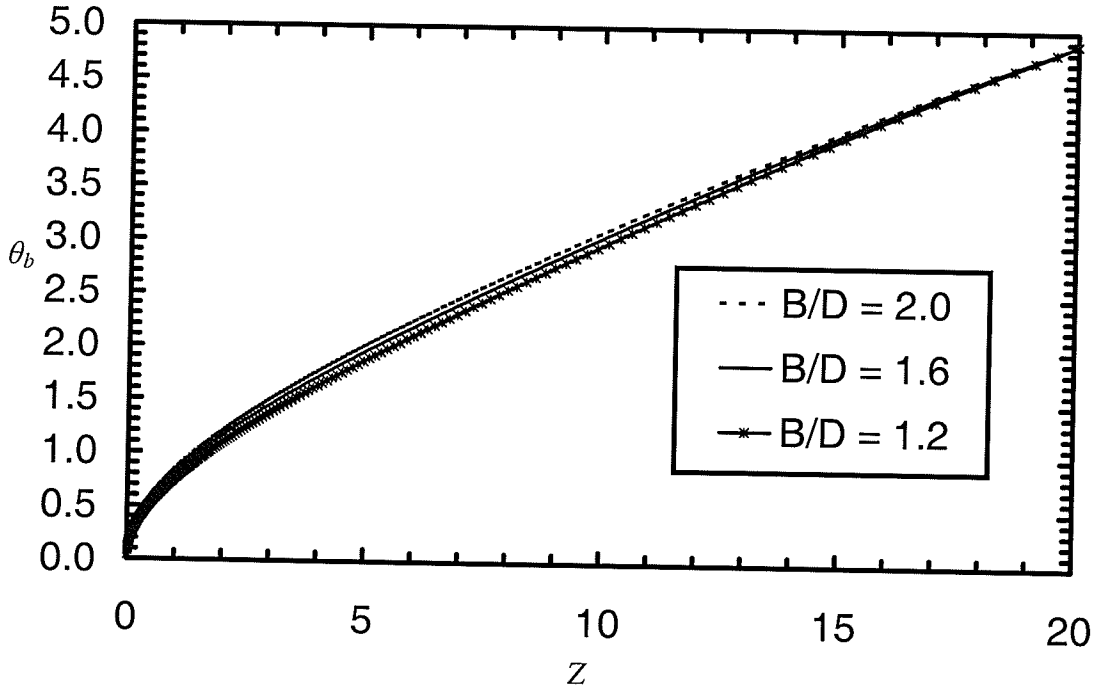

Figure 6.2 Effect of *B/D* on θ_b at *H/D = 4*

Figures 6.3 to 6.9 show the effects of varying *B/D* on different aspects of the thermal performance. Note that in all plots like Figures 6.4 to 6.7, a mirror image of the solution is plotted to show the whole heat sink cross-section. The angular variation of the local heat flux at various locations along the microchannel is presented in Figure 6.3 (see Appendix C for the relationship between N and *z/L*). It is apparent that the angular variation of the heat flux is reduced along the axial direction, particularly away from the inlet of the microchannel. The magnitude of the inlet heat flux ratio increases with increasing *B/D*, however, and is consistent with the axial heat input plot of Figure 6.1 where a higher rate of heat input is seen near the inlet of the microchannel than at the outlet. Note that in Figure 6.3, N=100 corresponds to $z/L \approx 0.09$.

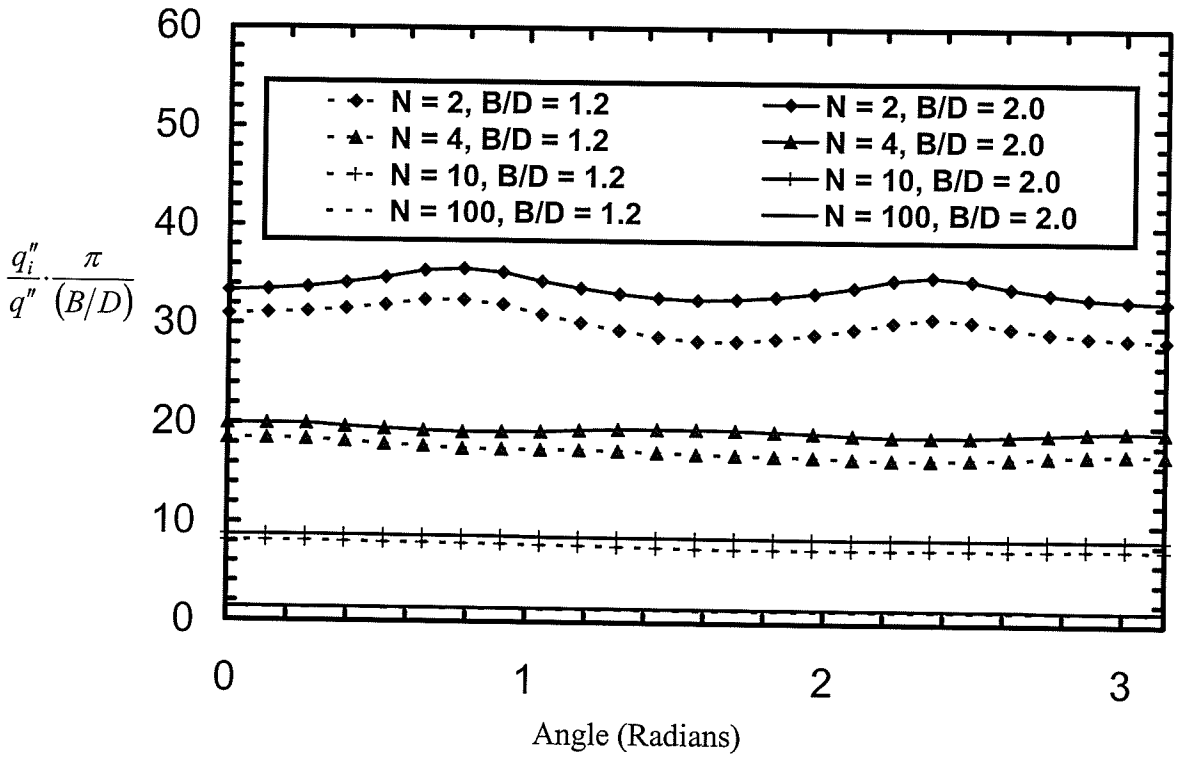

Figure 6.3 Effect of *B/D* on Angular Distribution of Input Heat Flux Around Microchannel at Various Locations Along Heat Sink for H/D = 4 (Angle = 0 at Top of Channel)

Figures 6.4 and 6.5 show isotherms in the heat sink near the inlet and near the outlet in the x-y plane, respectively, for B/D = 1.2 and H/D = 4, while Figures 6.6 and 6.7 show the same for B/D = 2 and H/D = 4 (see Appendix C for the relationship between N and z/L). Isotherms are not shown within the channel for clarity, however, all isotherms entering the channel trace the top wall tightly, and match up with the corresponding isotherm value on the opposite side of the heat sink. Temperature variation in the solid near the inlet of the B/D = 1.2 heat sink is higher than the B/D = 2 case. A change in θ_s of 2.62 between bottom and top isotherms is seen in the B/D = 1.2 case compared to a change of 1.12 for the B/D = 2 case. This relatively small difference in θ_s indicates a more uniform temperature distribution in the B/D = 2 near sink solid at the inlet. Near the outlet, the B/D = 2 heat sink continues to have a more uniform temperature distribution

than the heat sink with B/D = 1.2, having a 0.93 change in θ_s compared to a change of 2.43 for the B/D = 2 case. Isotherm values for the B/D = 2 case are higher than for B/D = 1.2 near the inlet, and the reverse occurs at the outlet, matching the results presented in Figure 6.1. Higher values of q_i'' at the solid-fluid interface for the B/D = 2 case at the inlet correspond to higher temperatures at the inlet. It can be seen from Figures 6.4 to 6.8 that lines of constant heat flux (not shown) which are perpendicular to the isotherms, indicate that heat enters the top of the channel relatively straight down from the surface. Lines of constant heat flux turn into the microchannel on the sides and bottom after travelling straight down from the surface. This trend is similar for all B/D cases.

From a design point of view, Figure 6.8 shows that increasing B/D decreases the average temperature variation across the top heat sink surface. The B/D = 1.2 case has a variation of 8.6 in $\overline{\theta_s}$ while the B/D = 2 case has a variation of 5.8 in $\overline{\theta_s}$. The B/D = 1.2 case also has the lowest value of θ_s over most of the heat sink except for $Z < 5$.

From Figures 6.9 and 6.10 it is evident that higher B/D values decrease the magnitude of temperature variation over the entire heat sink. The solid variation in θ_s in the y-z plane from the bottom of the heat sink to the top surface of the B/D = 1.2 case is approximately 2.80, while the same variation in the B/D = 2 case is approximately 1.49. Qualitatively, the isotherms are also much closer together in the axial (flow) direction for the B/D = 1.2 case which further indicates a larger temperature variation in the solid. Therefore, to create a lower and more constant surface temperature, as well as less internal stress due to temperature variation, a designer should choose a high B/D ratio.

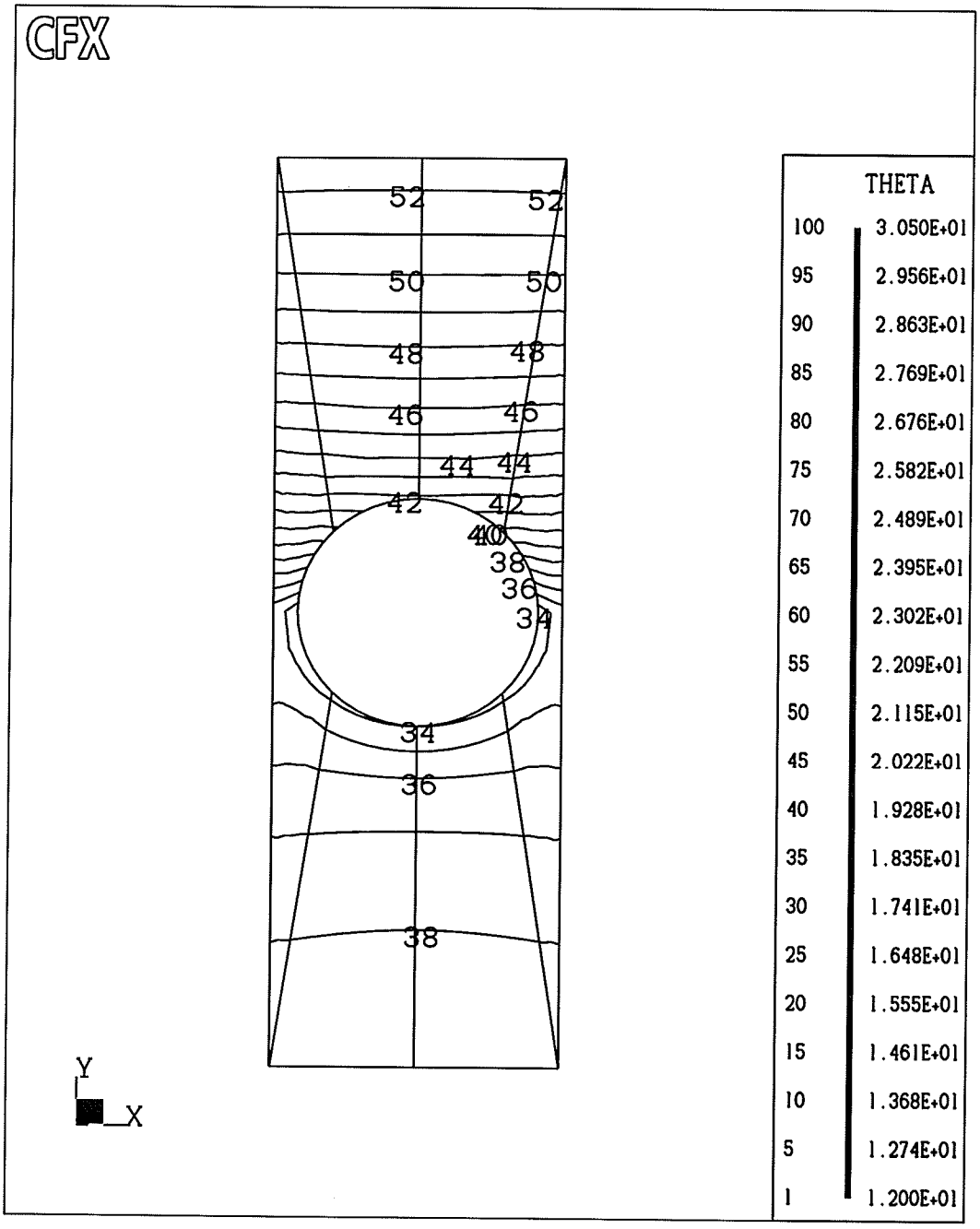

Figure 6.4 Isotherms Near the Inlet of a Microchannel (N=10) with $B/D = 1.2$ and $H/D = 4$

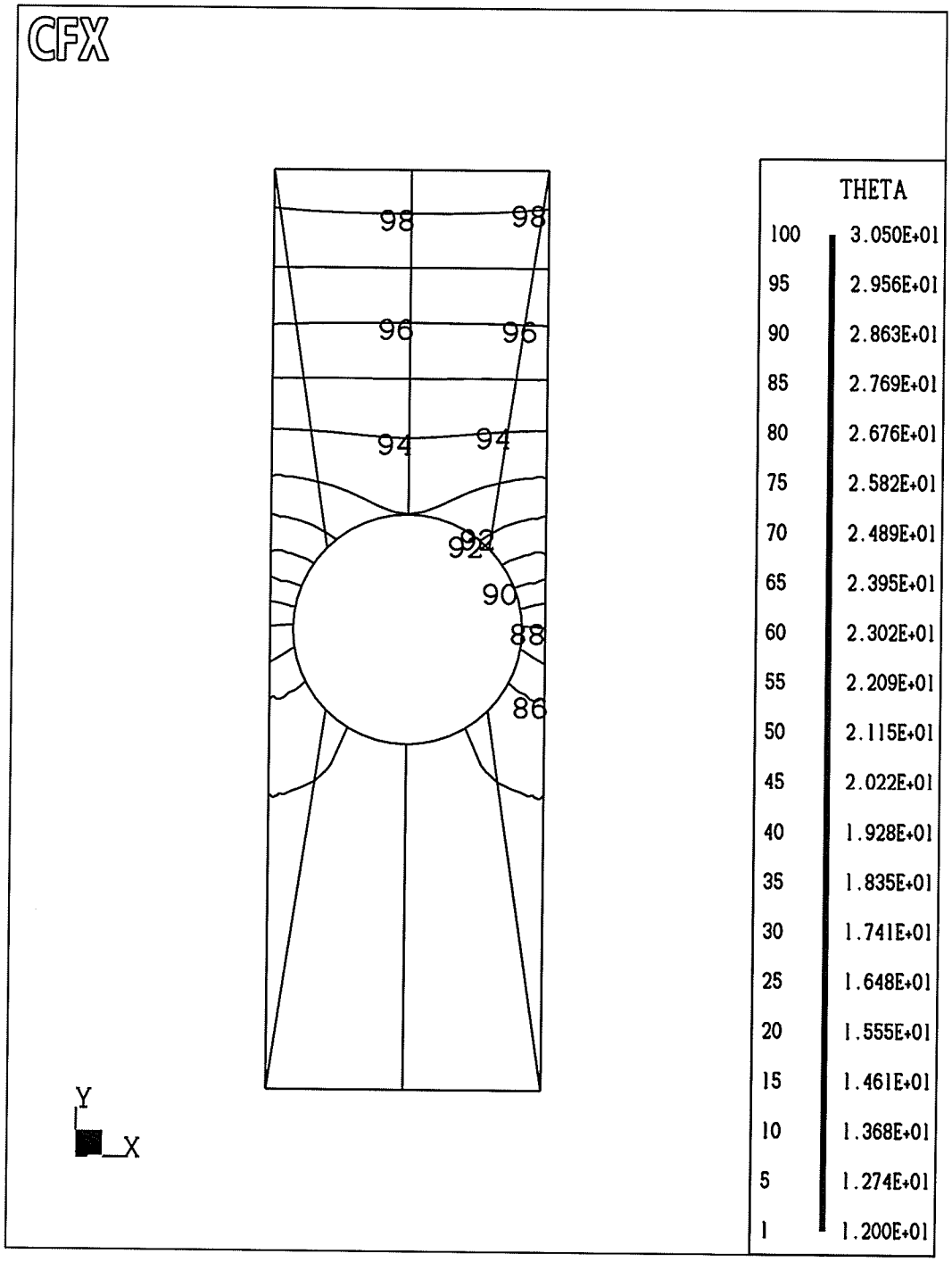

Figure 6.5 Isotherms Near the Outlet of a Microchannel (N=200) with B/D = 1.2 and H/D = 4

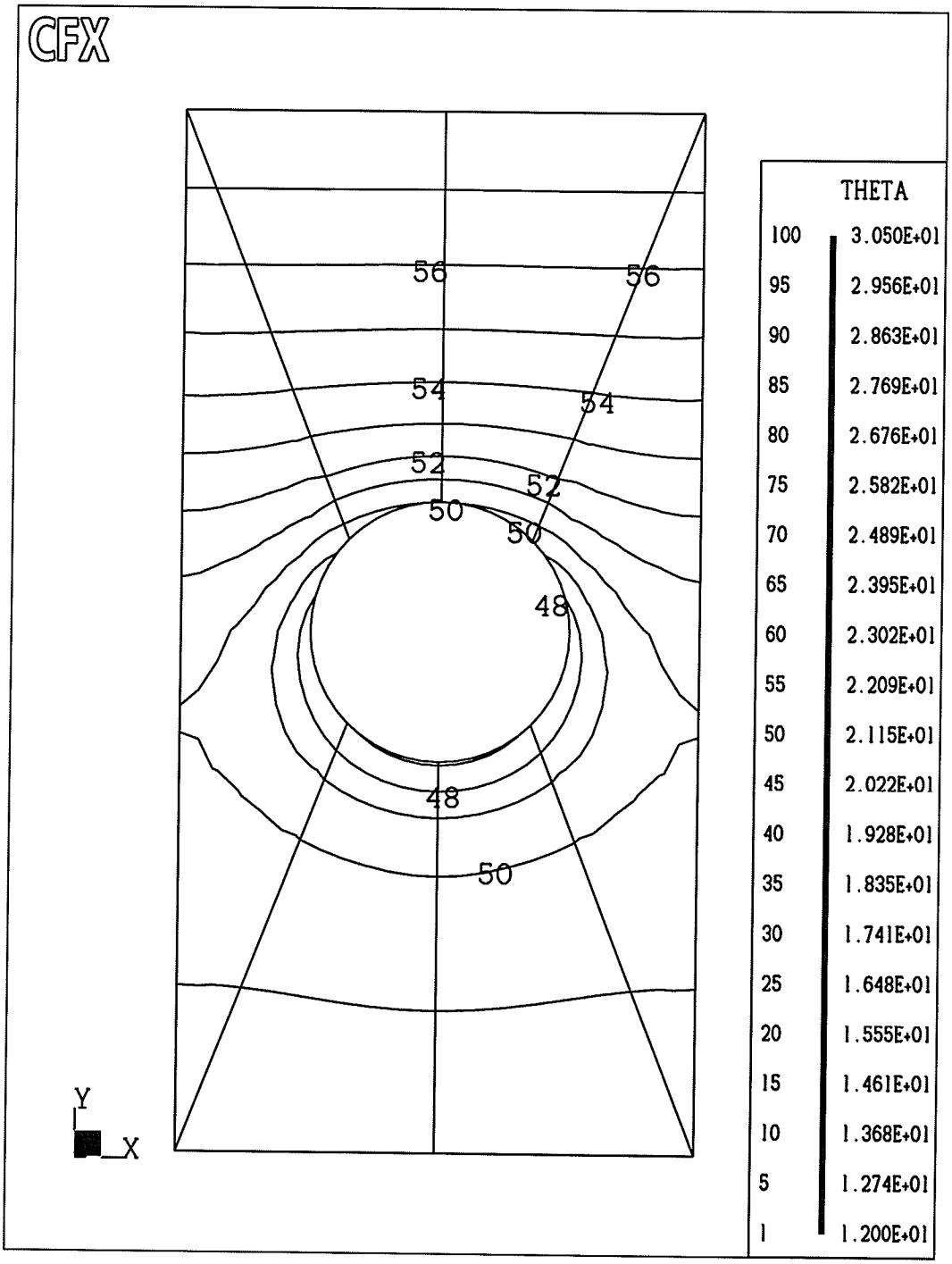

Figure 6.6 Isotherms Near the Inlet of a Microchannel (N=10) with $B/D = 2$ and $H/D = 4$

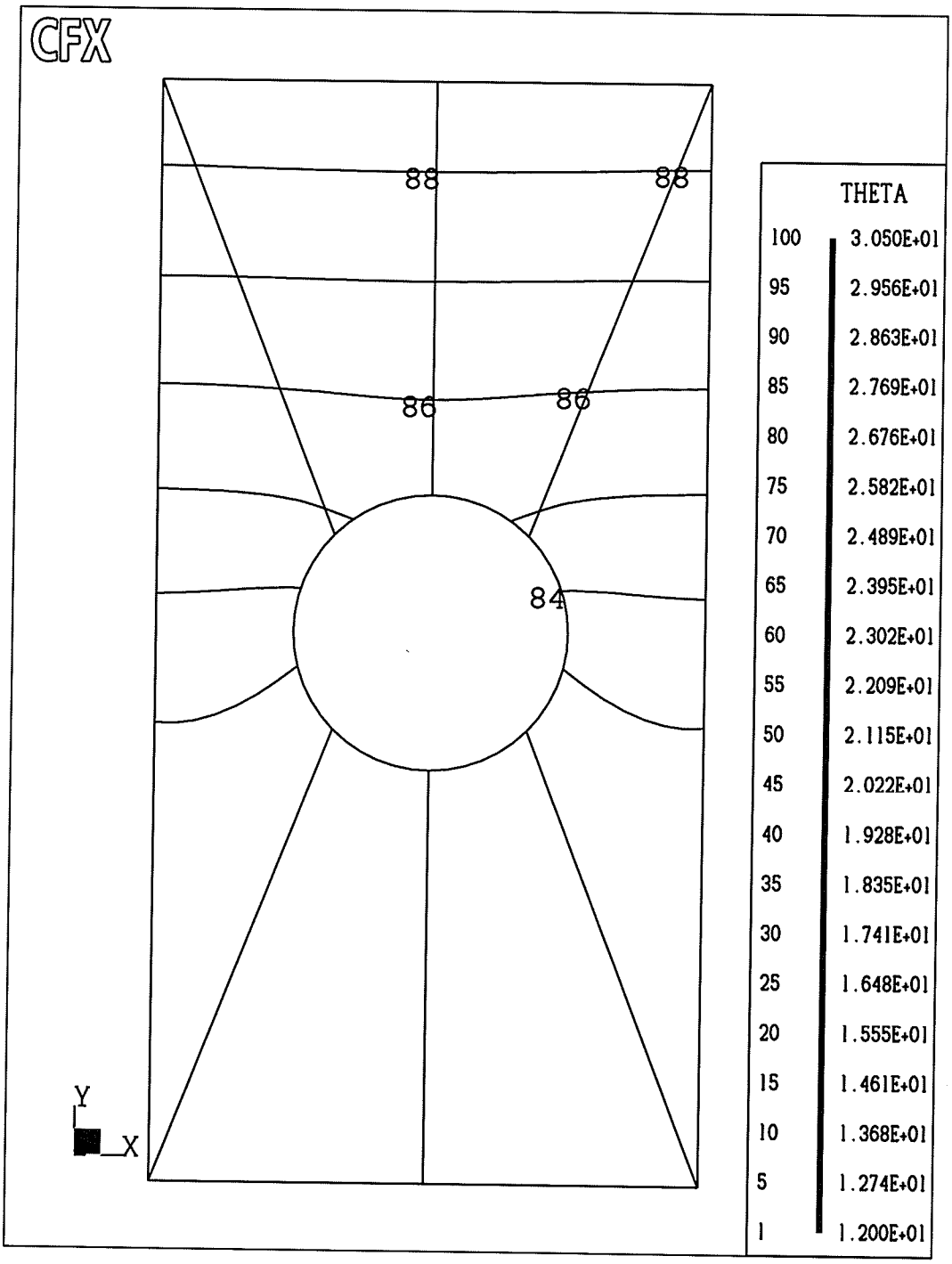

Figure 6.7 Isotherms Near the Outlet of a Microchannel (N=200) with $B/D = 2$ and $H/D = 4$

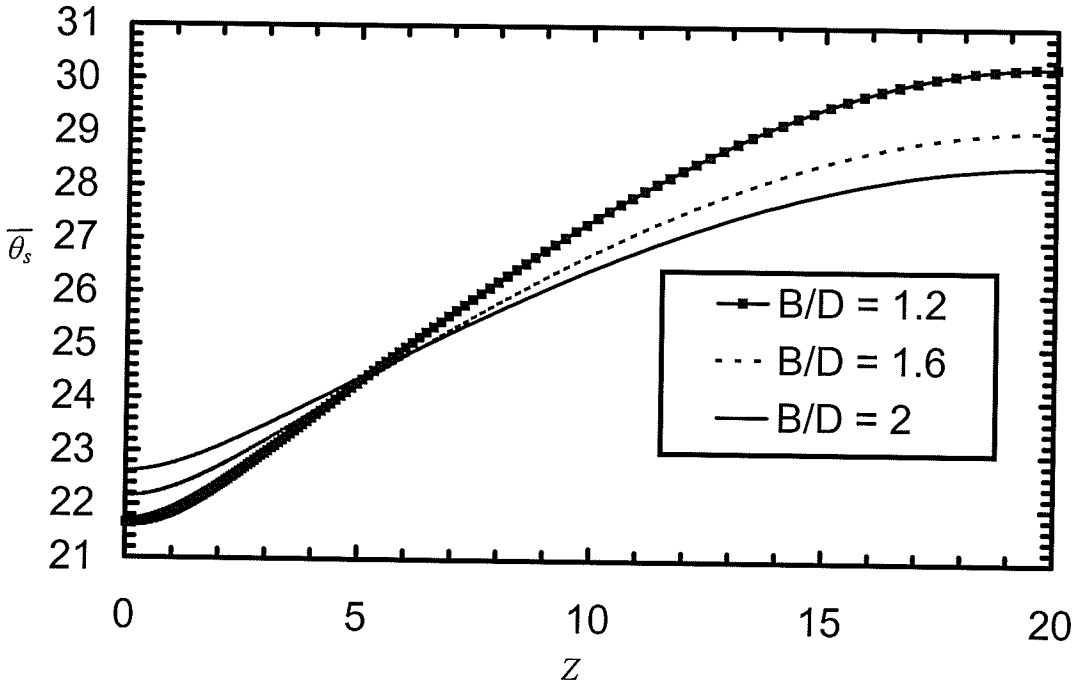

Figure 6.8 Dimensionless Temperature (Averaged Along X) of the Top Surface of Heat Sinks with various B/D values and with $H/D = 4$

Qu and Mudawar (2002) found that the axial temperature variation was much smaller in the solid below the microchannel than above. This smaller variation indicates that the thickness of the material above the solid is more important for heat transport into the heat sink than below. This phenomenon is visible in all right symmetry plane isotherm plots presented in this thesis. Two examples of these types of plots are Figures 6.9 and 6.10.

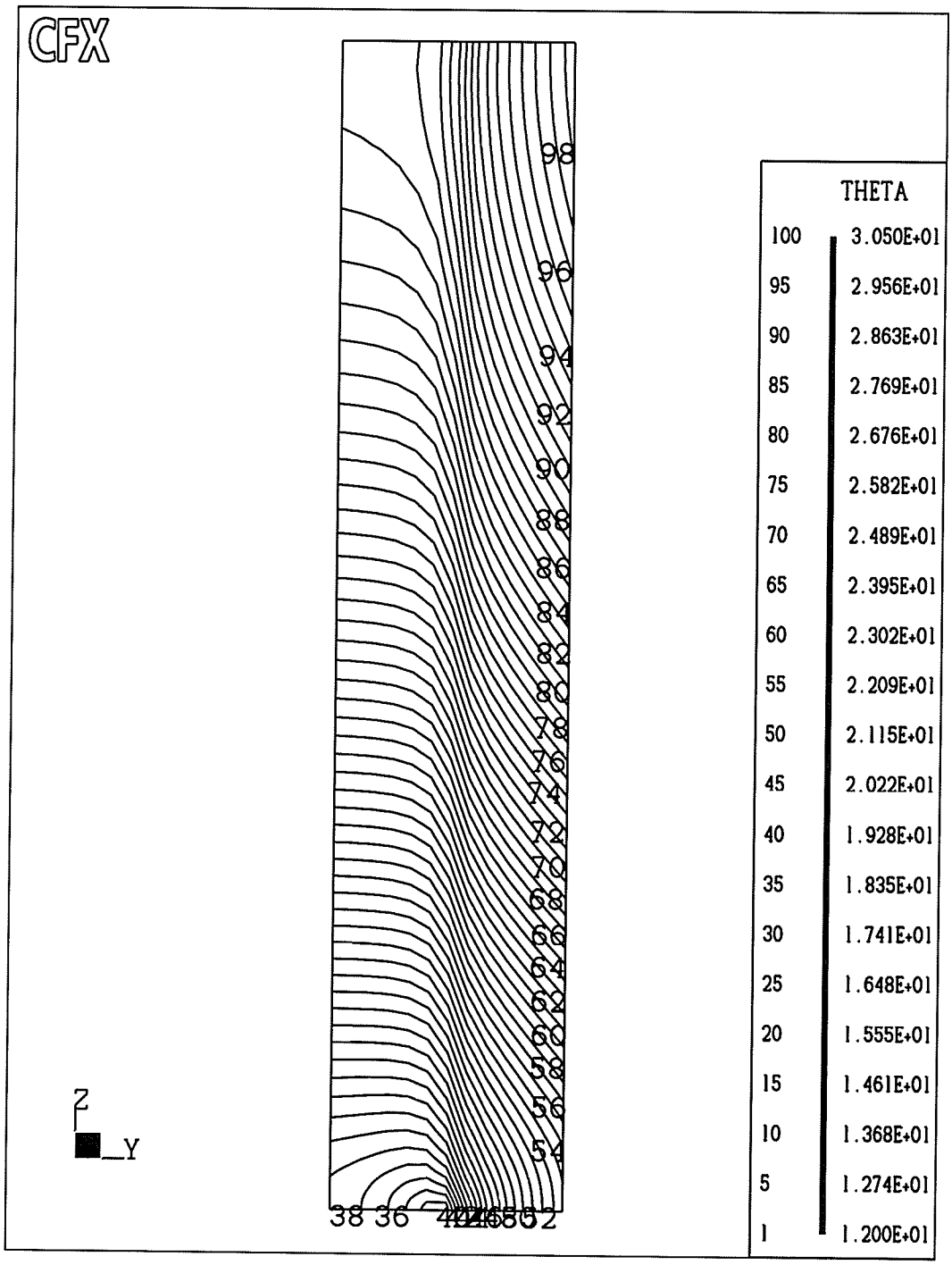

Figure 6.9 Side View of Isotherms Along a Heat Sink with $B/D = 1.2$ and $H/D = 4$ at Right Symmetry Plane ($X = B/(2D)$)

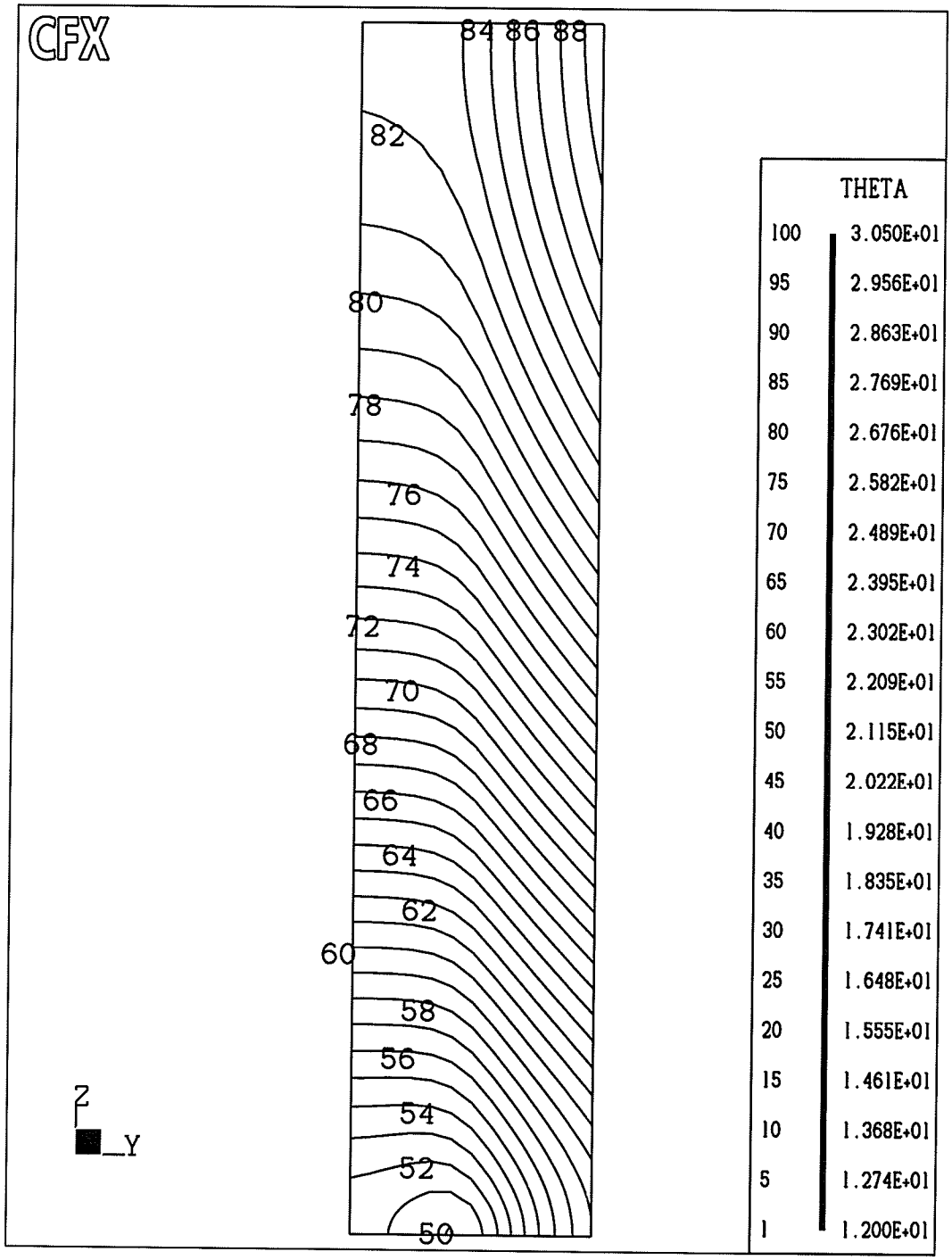

Figure 6.10 Side View of Isotherms Along a Heat Sink with $B/D = 2$ and $H/D = 4$ at Right Symmetry Plane ($X = B/(2D)$)

Finally, Table 6.2 shows the change in the overall dimensionless thermal resistance with changing *B/D* and *H/D* for a Reynolds number of 500 and copper-water as working materials (k_s/k_f = 668.3). A significant decrease in Γ^* occurs with decreased *B/D* (approximately by 36% for all cases of *H/D*). This decrease indicates that the smaller the web thickness between the microchannels, the lower the overall thermal resistance of the microchannel heat sink. The effects of *H/D* on the overall heat sink performance will be examined in Section 6.3.

The significant decrease in overall thermal resistance with *B/D* agrees with Ryu et al. (2002), who found that the most crucial quantity in dictating the performance of a microchannel heat sink was the channel width. A heat sink with less material between the microchannels has a higher channel surface area to heat sink solid volume ratio. This higher ratio ensures less heat transfer resistance from the heat sink surface through the solid volume and into the channels through the channel walls.

Table 6.2 Values of Γ^* for Various *B/D* and *H/D* for *Re* = 500 and k_s/k_f = 668.3

B/D	H/D = 2	H/D = 3	H/D = 4
1.2	1.56	1.53	1.51
1.6	2.00	1.96	1.94
2	2.44	2.39	2.37

6.3 Effect of Varying *H/D*

Figure 6.11 relates to the axial variation of normalized heat input, and it shows that near the inlet of the microchannel, the higher the *H/D* ratio, the higher the rate of heat absorbed by the fluid per unit length (back-heating). This higher heat transfer rate

continues until a Z of about 6. After this point, the axial variation of heat flux is slightly higher for decreasing H/D as it should be for overall energy conservation. Eventually the heat sinks reach a point where the incident heat flux ratio is identical, and can be seen as an intersection on the graph.

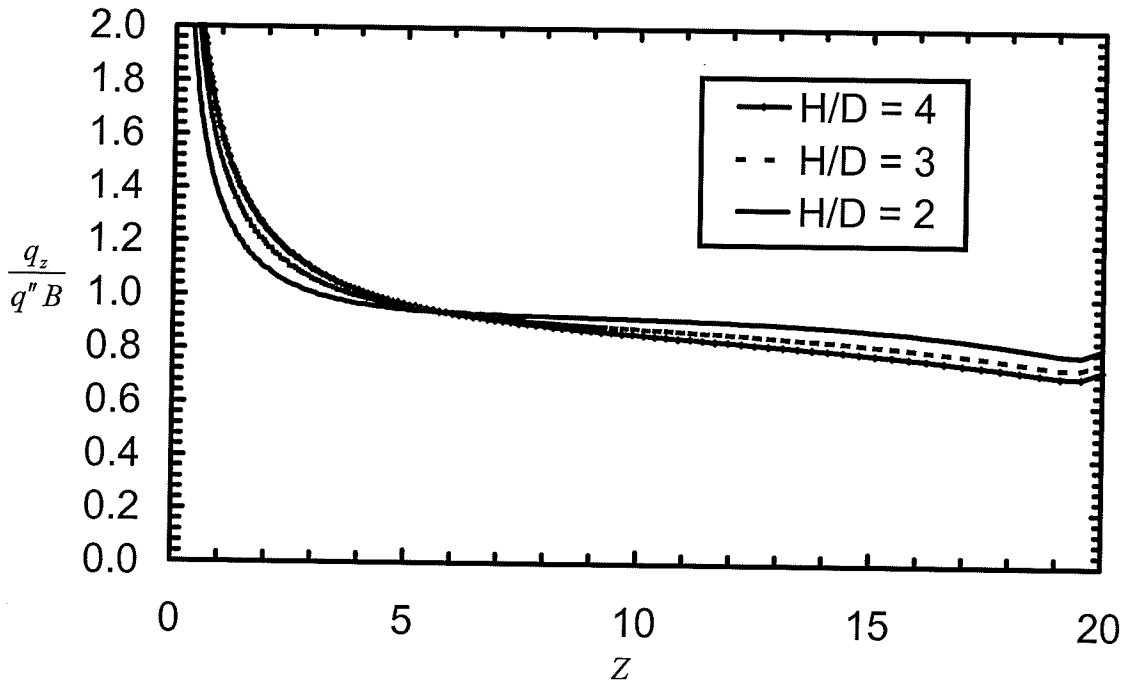

Figure 6.11 Effect of H/D on the Axial Variation of q_z for $B/D = 1.2$

Variation of the dimensionless bulk temperature along the microchannel for different values of H/D is shown in Figure 6.12. It is apparent that for increasing H/D, the bulk temperature along the microchannel also increases. Again, the trends in both the bulk temperature and axial distribution of heat input are similar for all values of B/D.

From Figure 6.13, it is visible that the angular variation of the heat flux at the solid-fluid interface reduces along Z, particularly away from the inlet of the microchannel. The magnitude of the interfacial flux ratio increases with increasing H/D however, and this is

consistent with the axial heat input plot of Figure 6.11 where higher *H/D* case experiences a higher rate of heat absorbed by the fluid per unit length near the inlet.

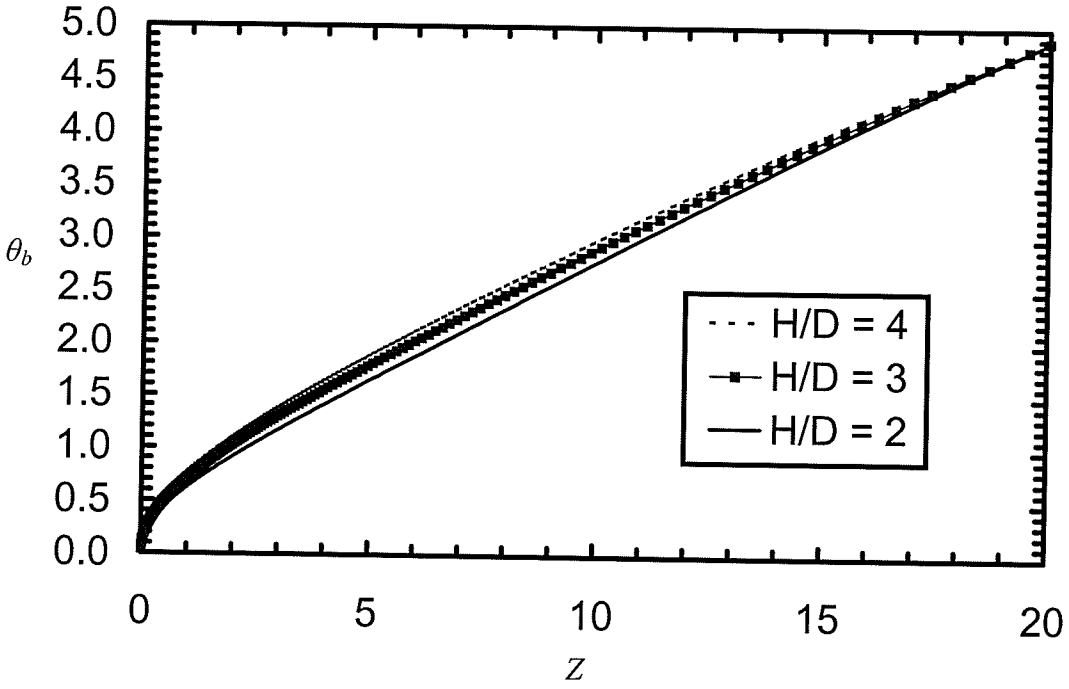

Figure 6.12 Effect of *H/D* on θ_b for *B/D* = 1.2

Figures 6.14 and 6.15 show isotherms in the heat sink near the inlet and near the outlet, respectively, for a heat sink with *H/D* = 2 and *B/D* = 1.2. Isotherms in the channel are omitted for clarity; however, all isotherms entering the channel trace the top wall tightly, and match up with the corresponding isotherm value on the opposite side of the heat sink. The difference in θ_s between the bottom and top regions of the *H/D* = 2 case is 2.06, while the *H/D* = 4 (Figure 6.4) case has a difference of 2.80. The same trend occurs at the outlets of the two heat sinks with the *H/D* = 4 case (Figure 6.5) having a difference of 2.43 and the *H/D* = 2 case having a difference of 1.31 between maximum and minimum isotherms. Isotherms for the *H/D* value of 4 are higher than those for the *H/D* of 2 near

the inlet, and the reverse occurs at the outlet, matching the results presented in Figure 6.11. A higher interfacial heat flux in the $H/D = 4$ case at the inlet corresponds to a higher temperature at the inlet. Likewise, a lower interfacial heat flux in the $H/D = 2$ case at the outlet corresponds to a lower temperature at the outlet than in the $H/D = 2$ case. In Figure 6.14 and 6.15, lines of constant heat flux (not shown) which are perpendicular to the isotherms suggest that heat enters the top of the channel relatively straight down from the surface. Lines of constant heat flux turn into the microchannel on the sides and bottom after travelling straight down from the surface. This trend is similar for all H/D cases.

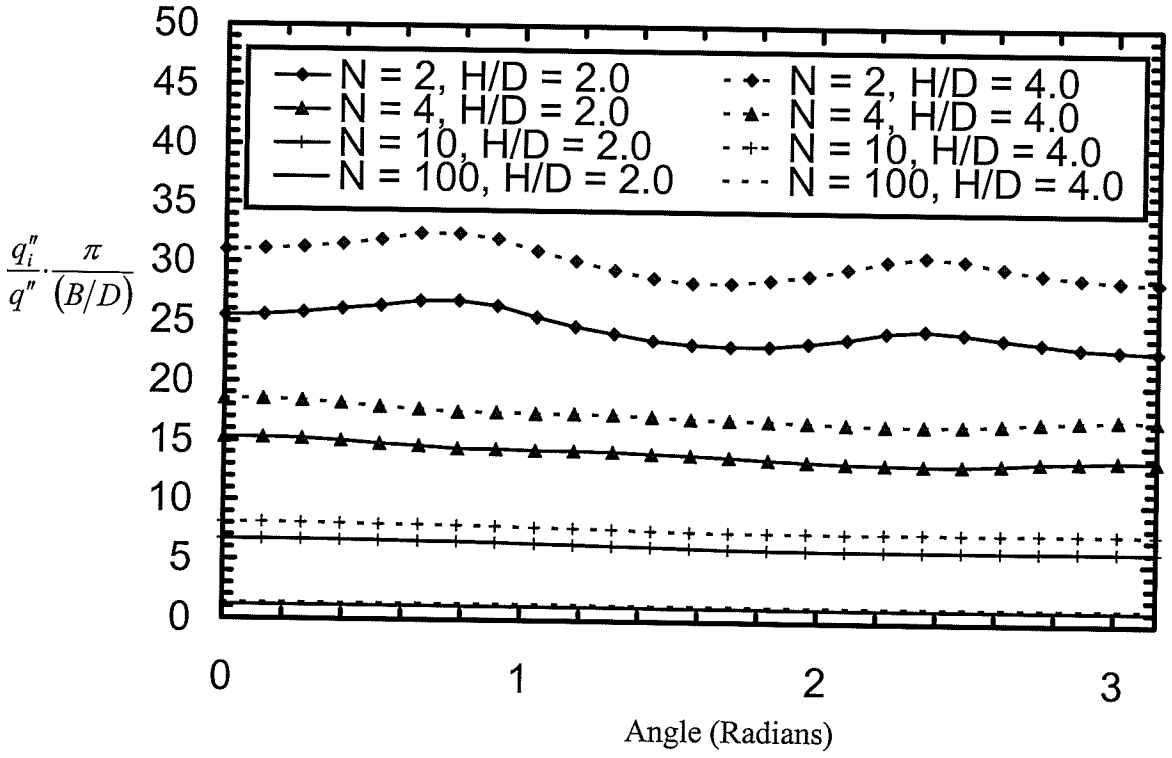

Figure 6.13 Effect of H/D on Angular Distribution of Heat Flux Around a Microchannel at Various Locations Along a Heat Sink with $B/D = 1.2$ (Angle = 0 at Top of Channel)

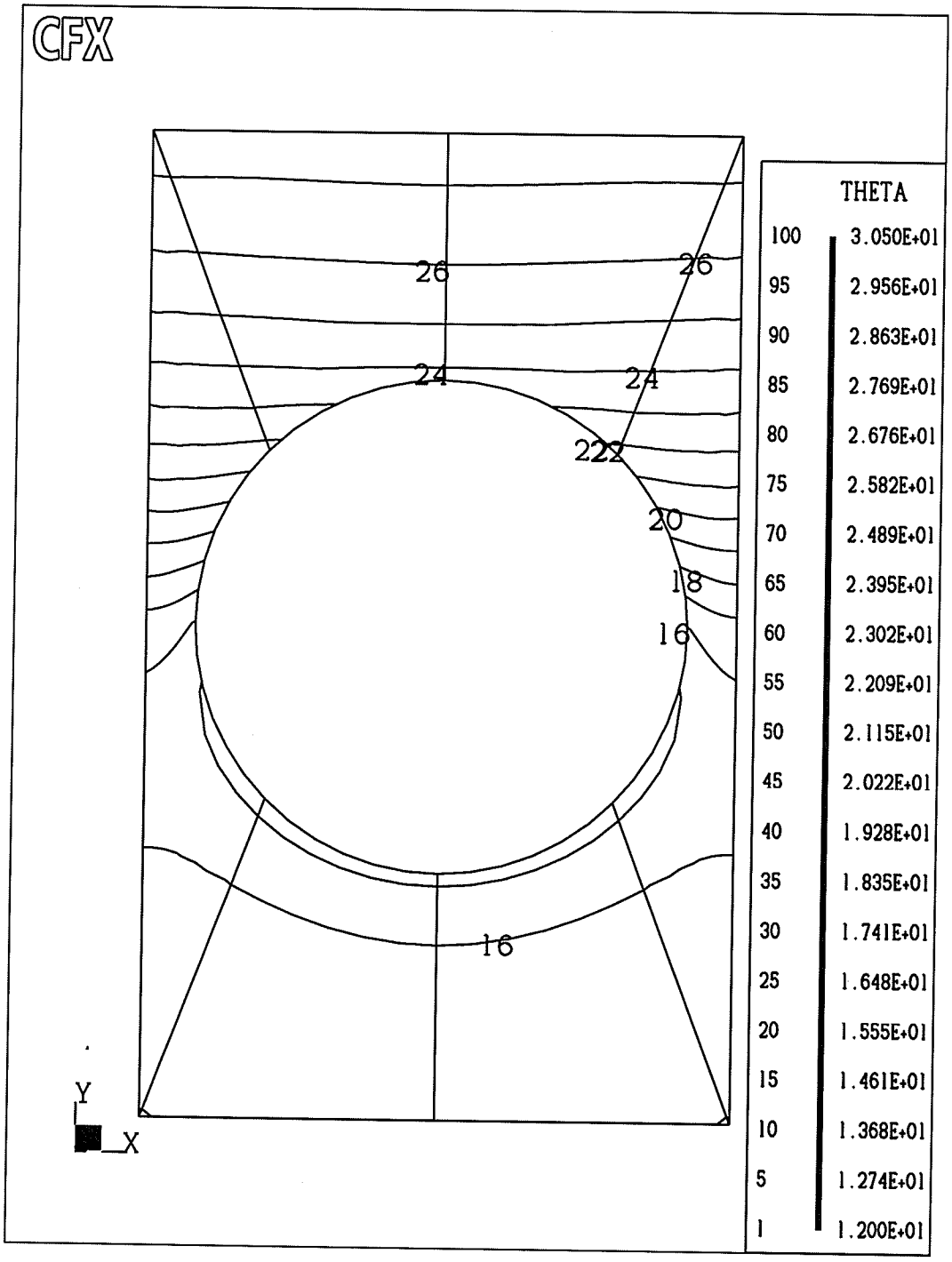

Figure 6.14 Isotherms Near the Inlet of a Microchannel (N=10) with $B/D = 1.2$ and $H/D = 2$

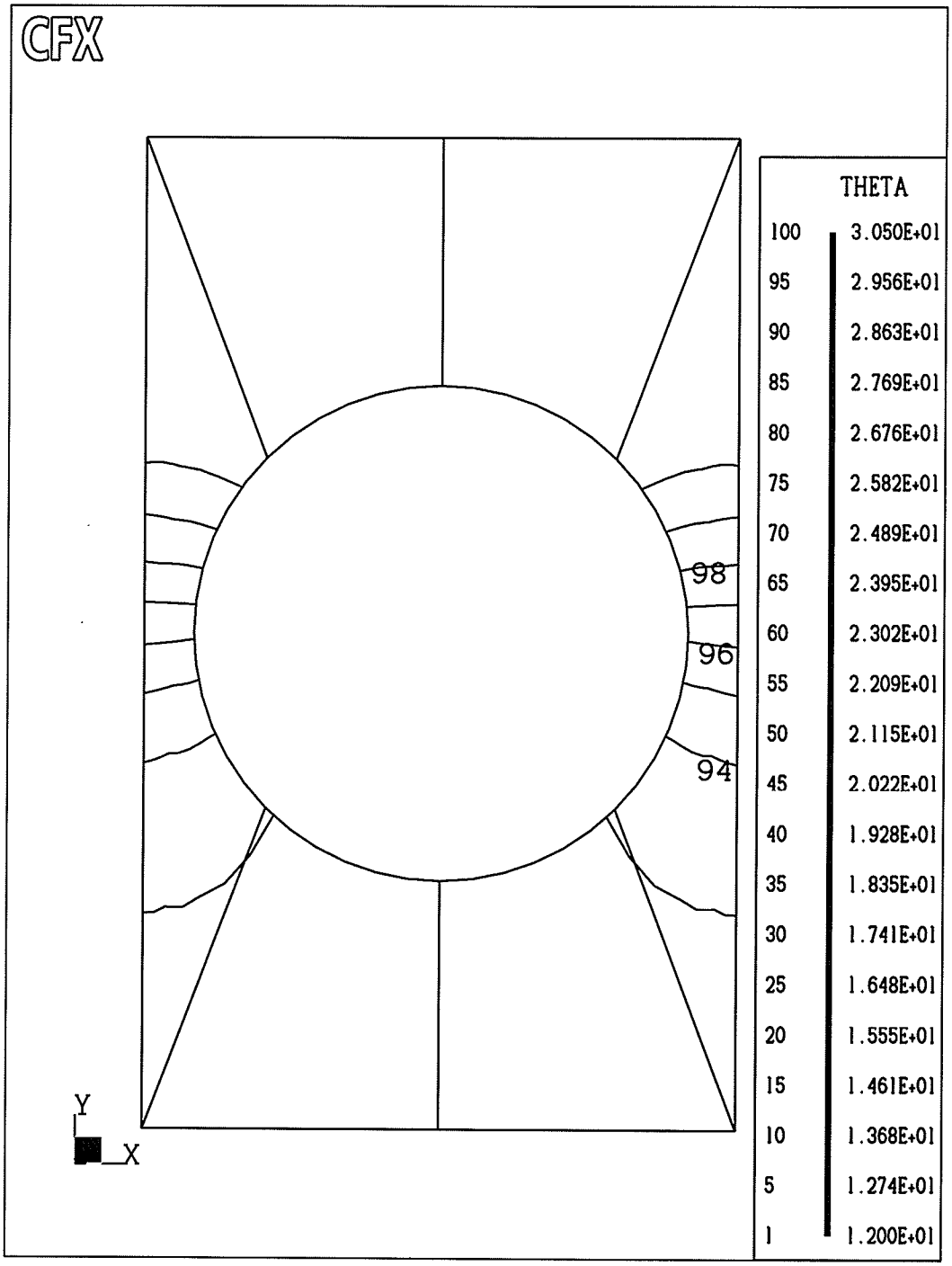

Figure 6.15 Isotherms Near the Outlet of a Microchannel (N=200) with $B/D = 1.2$ and $H/D = 2$

Figure 6.16 shows that increasing *H/D* creates a more uniform surface temperature of the heat sink solid; however, the surface temperature is the lowest along most of the heat sink in the axial direction for the *H/D* = 2 case. The *H/D* = 4 case produces an 8.6 change in $\overline{\theta_s}$ over the surface compared to a change of 14.2 in the *H/D* = 2 case. The highest value of $\overline{\theta_s}$ at the surface of the *H/D* = 4 case is 30.6, which is the lowest temperature at the outlet of the three cases.

When comparing the isotherms shown in Figure 6.17 with those in Figure 6.9, it is seen qualitatively that the axial temperature variation in the heat sink solid does change appreciably with the *H/D* ratio. The axial isotherm distribution in the *H/D* = 4 case is coarser than that of the *H/D* = 2 case. The *H/D* = 4 case has a relatively small θ_s difference between the bottom of the heat sink and top surface of 2.62, while the *H/D* = 2 case also has a relatively small difference of 1.87 in the axial (flow) direction in the y-z plane.

From the above analysis, we can see that the variation in surface temperature is large with varying *H/D*. If a low surface temperature variation and low ultimate temperature are of utmost importance, a higher *H/D* value should be chosen. It is not immediately clear which *H/D* value should be chosen to reduce the temperature variation in the heat sink. Higher *H/D* values produce lower axial temperature variation in the heat sink, while lower *H/D* values produce lower transverse temperature variation, as explained above.

Table 6.2 (section 6.2) shows quantitatively how changing the *H/D* ratio affects the heat sink overall thermal performance. Higher values of *H/D* yield lower thermal resistances but the effect is very minimal. Doubling the *H/D* ratio produces a mere 3.2% decrease in thermal resistance for a copper heat sink with $Re = 500$ and a *B/D* ratio of 1.2.

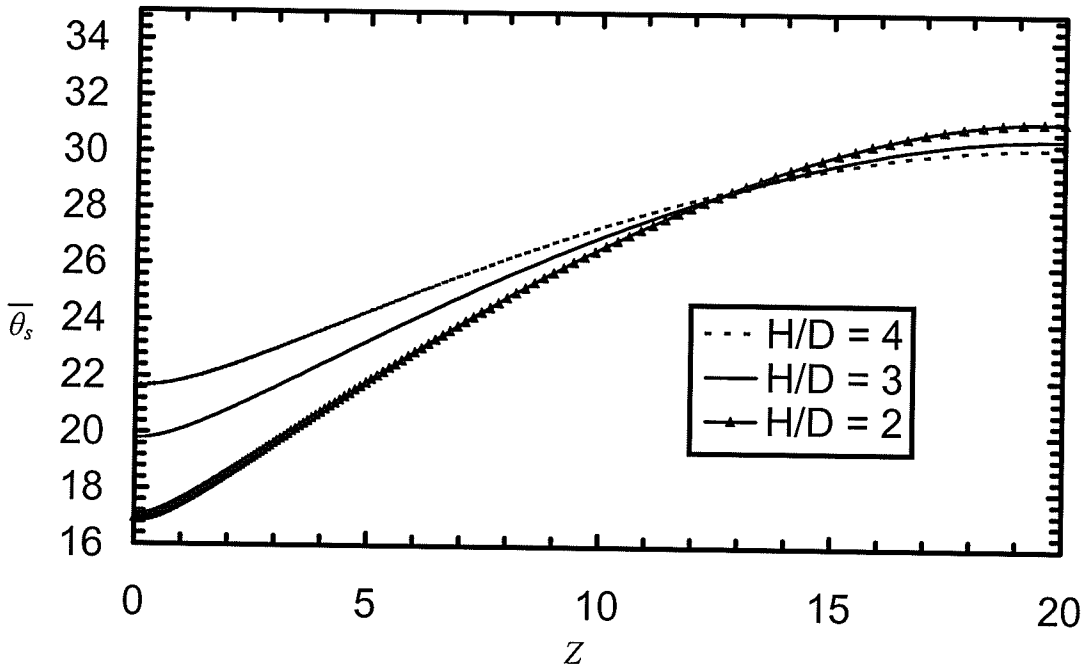

Figure 6.16 Dimensionless Temperature (Averaged Along X) of the Top Surface of Heat Sinks with Various *H/D* values and *B/D* = 1.2

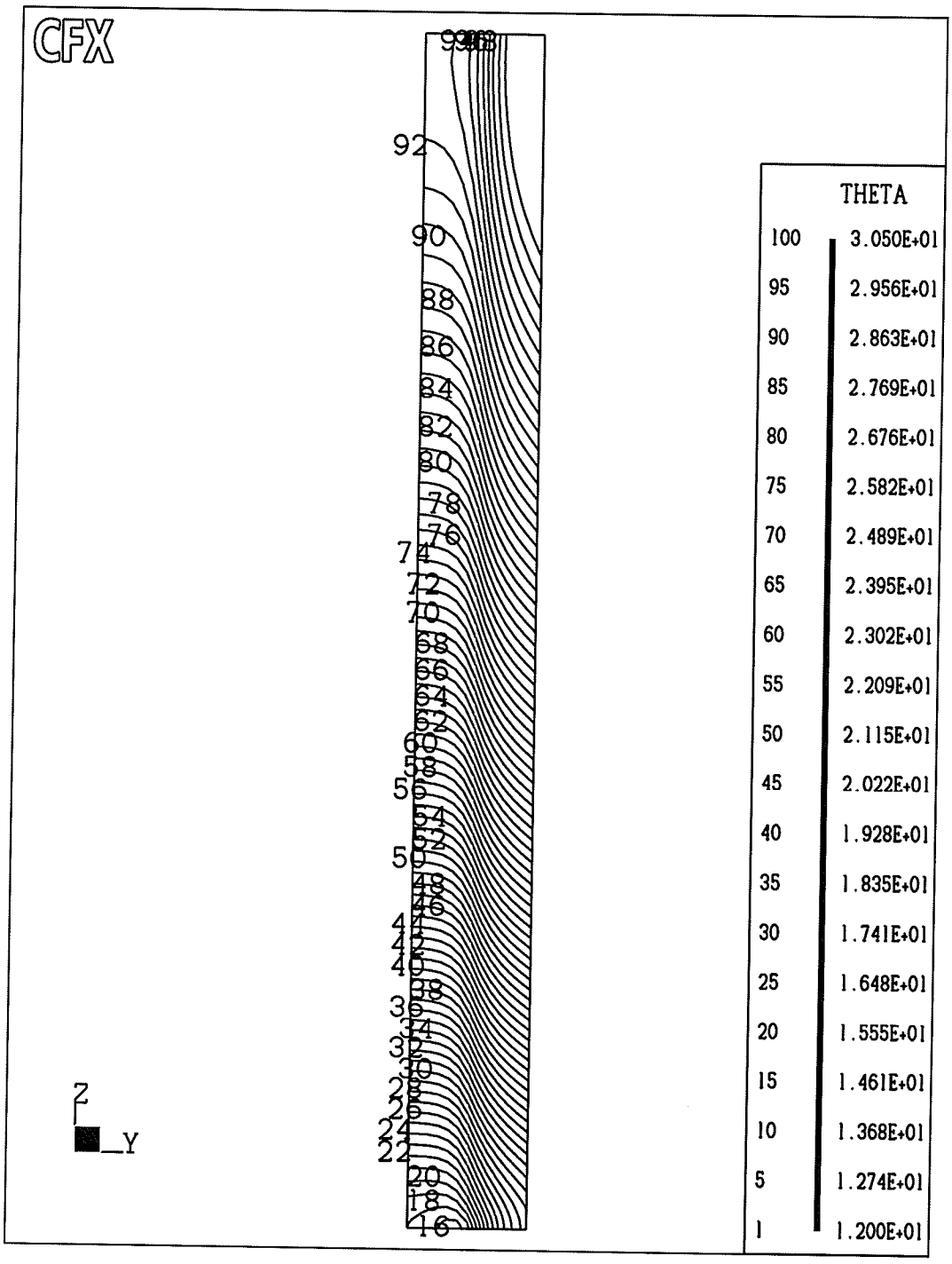

Figure 6.17 Side View of Isotherms Along a Heat Sink with $B/D = 1.2$ and $H/D = 2$ at Right Symmetry Plane ($X = B/(2D)$)

6.4 Effect of Varying *Re*

Traditionally, increasing the Reynolds number in the fluid increases the heat transfer coefficient and therefore decreases the thermal resistance for internal flow. This is indeed the case when looking at the data presented in Figure 6.18. The predicted Nu_z for Re = 1000 is higher than that for the Re = 500 case. It is also noted that both curves agree well with Nu_z for developing flow with a constant temperature boundary condition as given in Table 5.5 (a). These data also agree with Ambatipudi and Rahman (2000) as they reported very large Nusselt numbers at the inlet due to the development of the thermal boundary layer, and an increase in heat transfer coefficient inside the channel with increasing Reynolds number.

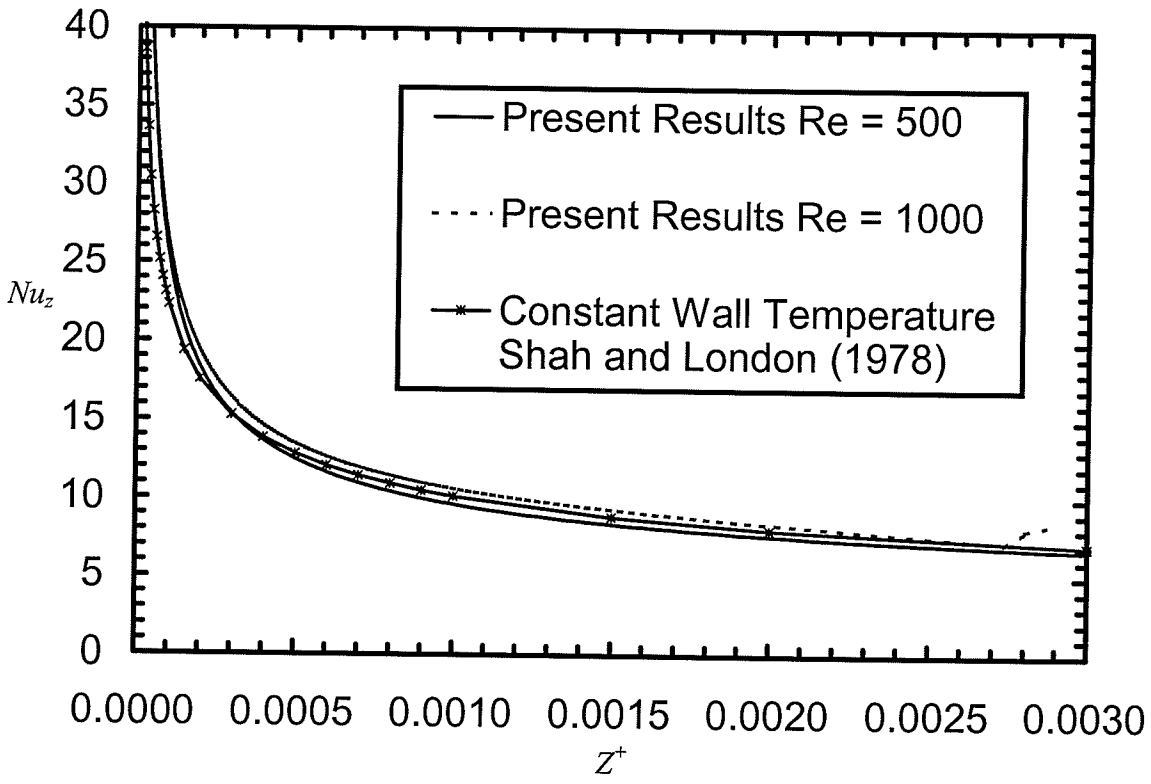

Figure 6.18 Comparison of Predictions for Nu_z vs. Z^+ for a Microchannel with H/D = 4 and B/D = 2 for Re = 500 and Re = 1000

The Nusselt number in the higher Reynolds case may be higher over the entire heat sink, however, this fact does not ensure more back-heating in the microchannel. In fact, the opposite is true. From Figure 6.19 we see that near the inlet of the microchannel, more of the energy applied at the top of the heat sink travels upstream to enter the fluid for the lower Reynolds number case.

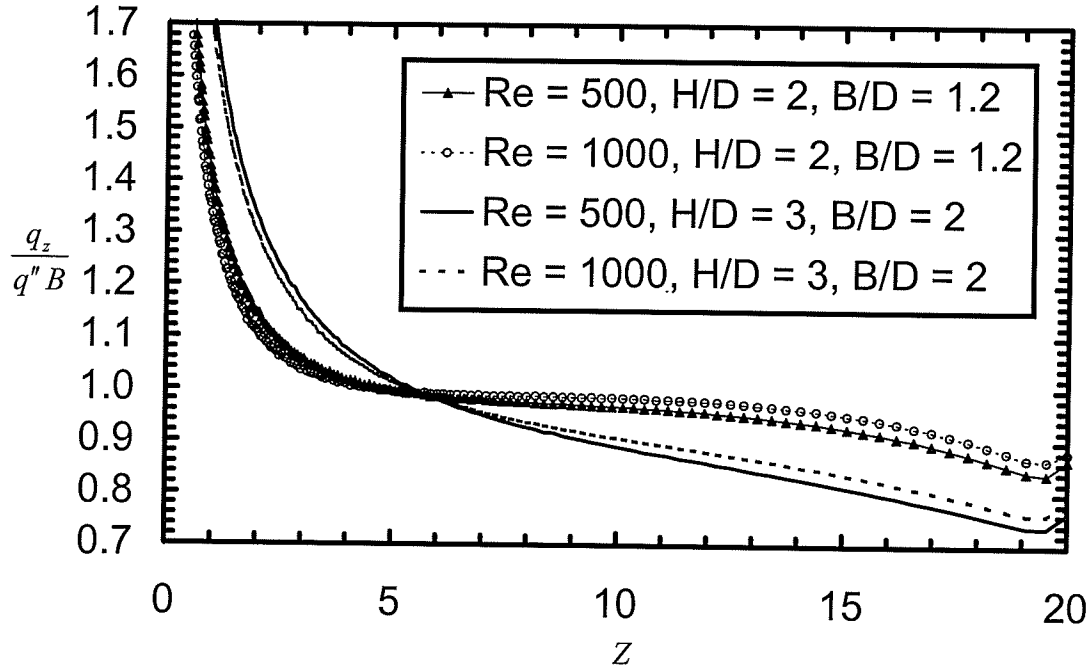

Figure 6.19 Effect of *Re* on the Axial Variation of q_z for *B/D* = 1.2 and *H/D* = 2, and *B/D* = 2 and *H/D* = 3

This phenomenon is thought to be a result of a smaller thermal boundary layer thickness along the entire microchannel with higher Reynolds number as illustrated in Figure 6.20. The thermal resistance at the inlet of the channel is proportionally lower than that of the rest of the microchannel compared to a lower Reynolds number case. Thus, the heat input is spread out more along the channel with higher Reynolds number.

This above argument can be expressed in the terms of areas. The area under each curve in Figure 6.19 must equal 20 (=*L/D*) because all of the input heat flux must enter the fluid. Since the thermal boundary layer thickness along the entire higher Reynolds number microchannel is lower, the area under the curve must be larger for most of the channel length, therefore, the area at the inlet must be lower.

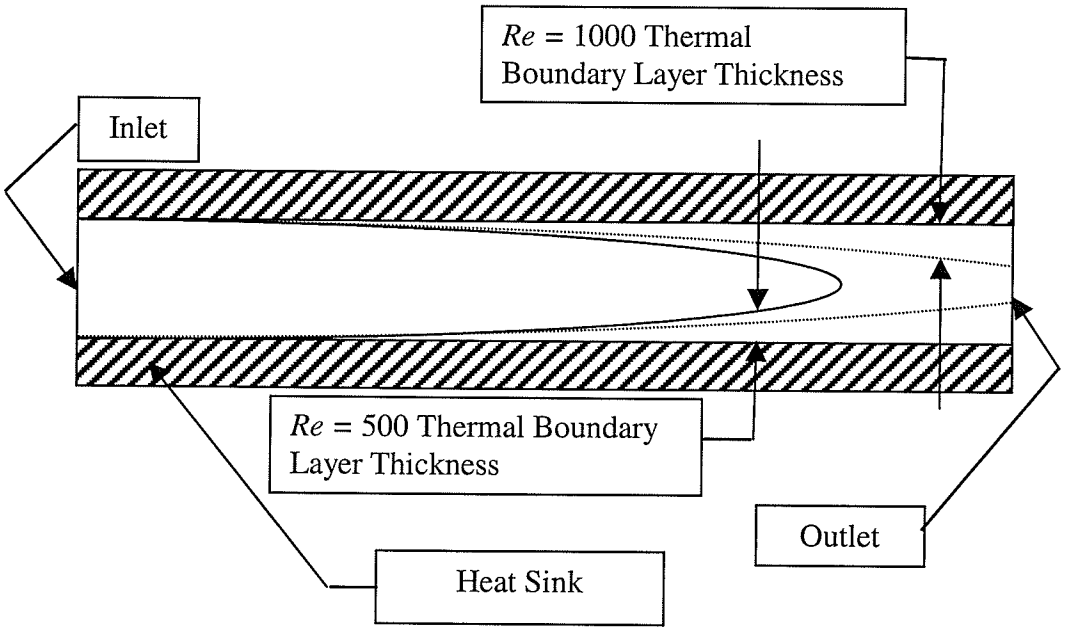

Figure 6.20 Boundary Layer Growth Representations for Varying Reynolds Numbers in a Circular Microchannel

Figure 6.21 presents dimensionless bulk temperature along the microchannel for two different Reynolds numbers and geometries. It is clear that increasing the Reynolds number dramatically decreases the bulk temperature along the microchannel. This is to be expected since Eq. (6.4) shows that dimensionless bulk temperature at the outlet is inversely proportional to the Reynolds number.

Figure 6.22 shows the angular variation in the channel-wall heat flux along the microchannel for two different Reynolds numbers. At the inlet of the microchannel, increasing Reynolds number tends to decrease the magnitude of the inlet heat flux ratio which agrees with Figure 6.19. The trend from Figure 6.22 suggests that everywhere else along the channel, changing the Reynolds number has little or no effect on the magnitude of this ratio, or its angular variation. Angular temperature variation and bulk temperature trends for varying *Re* were similar in all geometries analyzed.

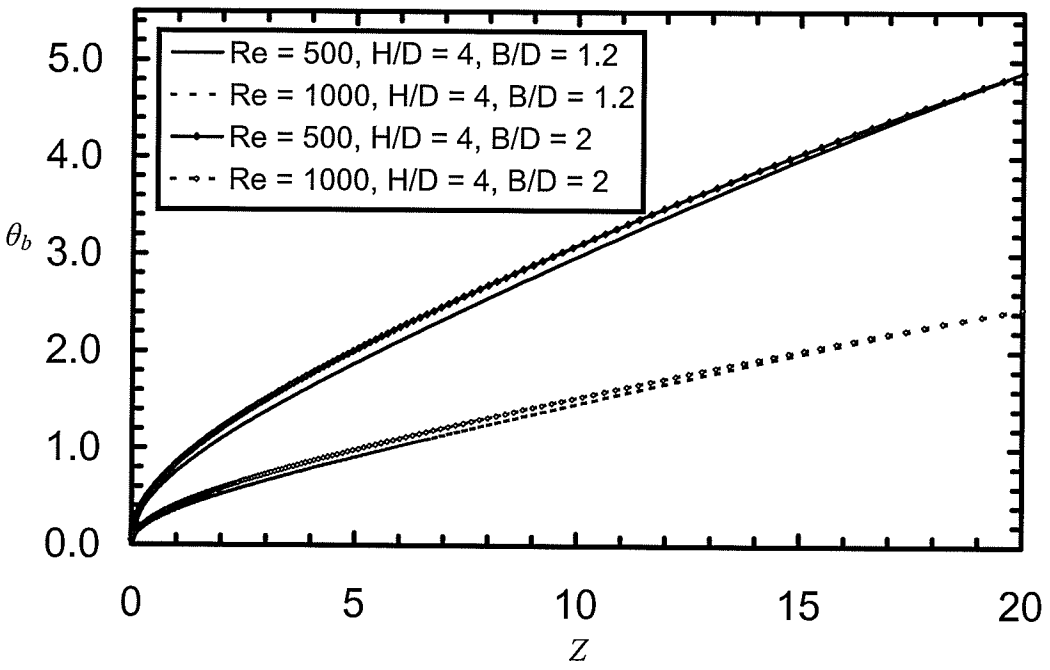

Figure 6.21 Effect of *Re* on θ_b for *H/D* = 4 and *B/D* = 1.2, and *H/D* = 4 and *B/D* = 2

Isotherms presented in Figures 6.23 and 6.24 are consistent with the dimensionless bulk temperature data presented in Figure 6.21. Temperatures in the heat sink solid for the *Re* = 1000 case are lower than the *Re* = 500 case shown in Figures 6.4 and 6.5. The temperature distribution in the two *Re* = 500 and *Re* = 1000 cases are almost identical

with a variation of θ_s of approximately 2.62 at the inlet and approximately 2.43 at the outlet for both cases. This small variation indicates Reynolds number has little effect on temperature distribution in the transverse direction throughout the heat sink. These trends do not match Figure 6.19 because the mass flow rates are different for the two Reynolds number cases. Isotherms in the channel are not shown for clarity, however, all isotherms entering the channel trace the top wall tightly, and match up with the corresponding isotherm value on the opposite side of the heat sink. Lines of constant heat flux (not shown) suggest that heat enters the top of the channel relatively straight down from the surface and turn into the microchannel on the sides and bottom after travelling straight down from the surface. This trend is similar for both *Re* cases.

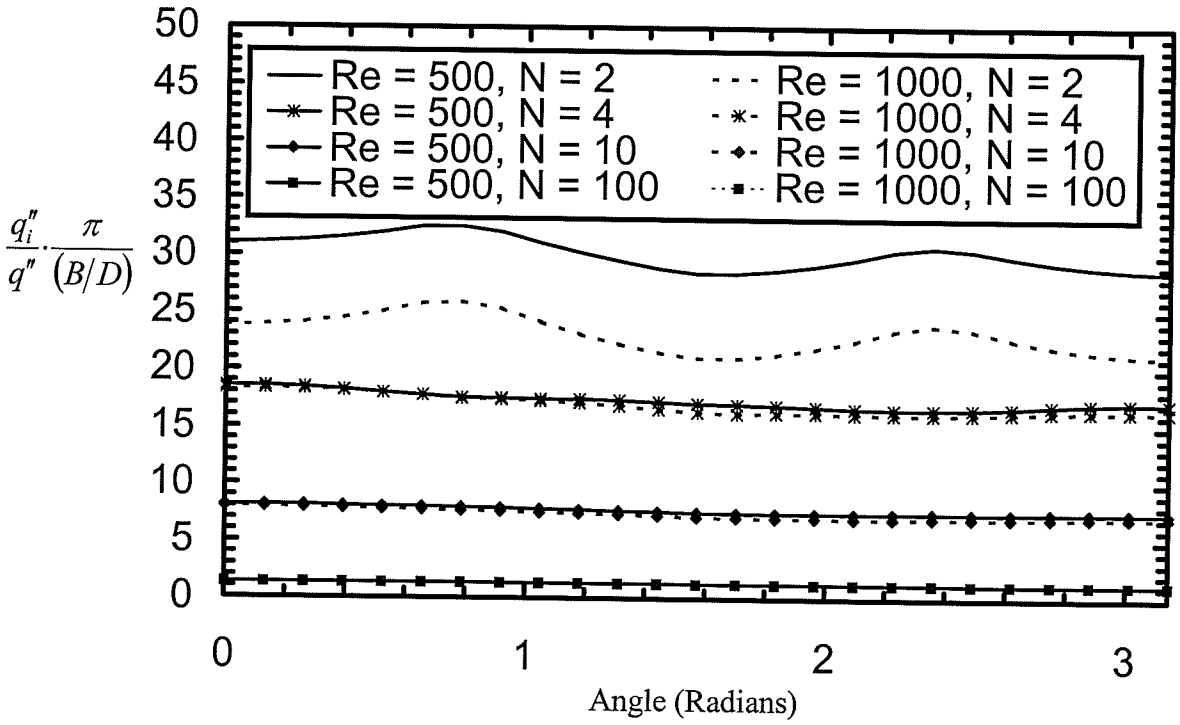

Figure 6.22 Effect of *Re* on Angular Distribution of Heat Flux Around a Microchannel at Various Axial Locations Along a Heat Sink with $H/D = 4$ and $B/D = 1.2$ (Angle = 0 at Top of Channel)

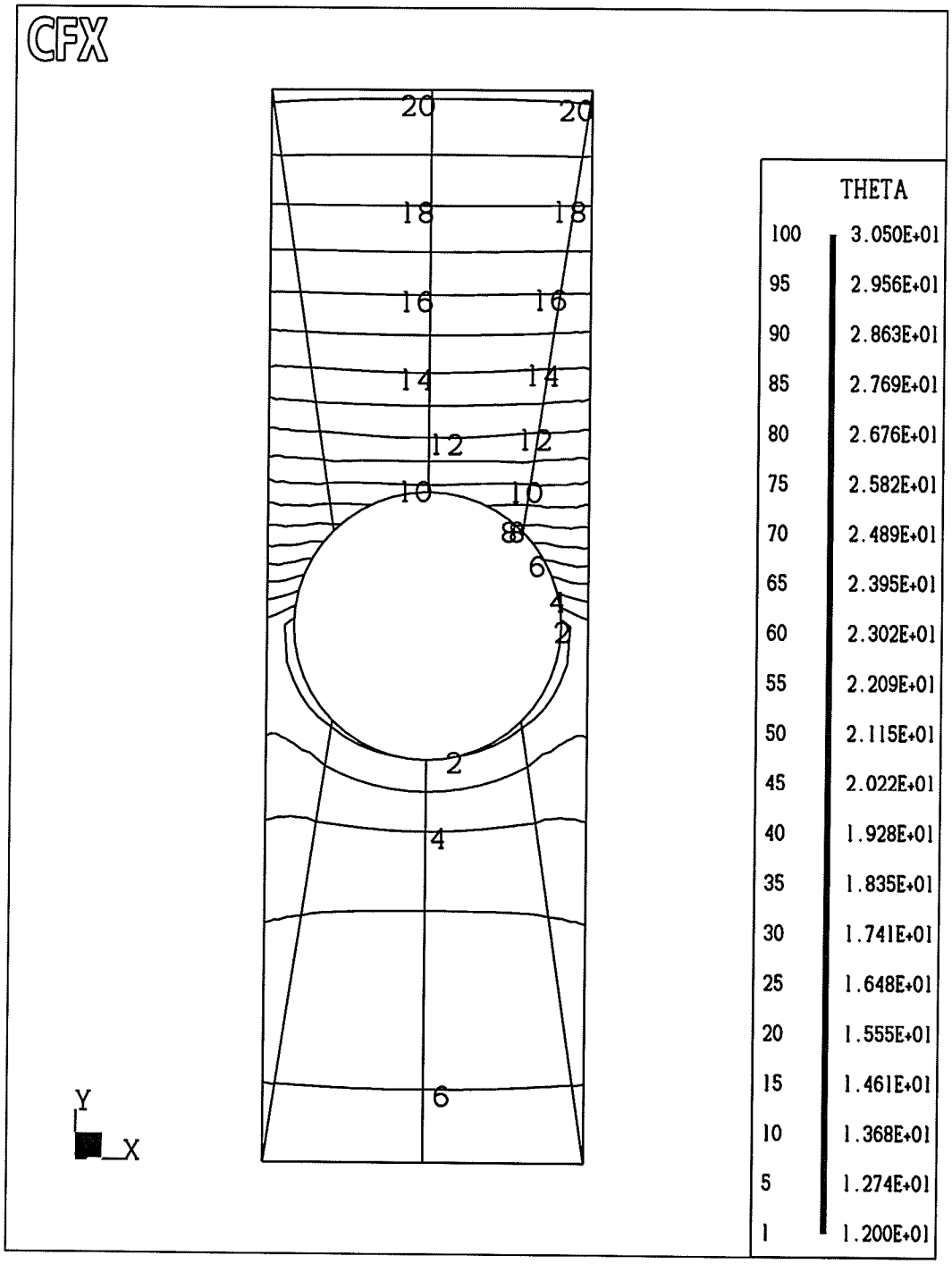

Figure 6.23 Isotherms Near the Inlet of a Microchannel (N=10) with $B/D = 1.2$ and $H/D = 4$, ($Re = 1000$)

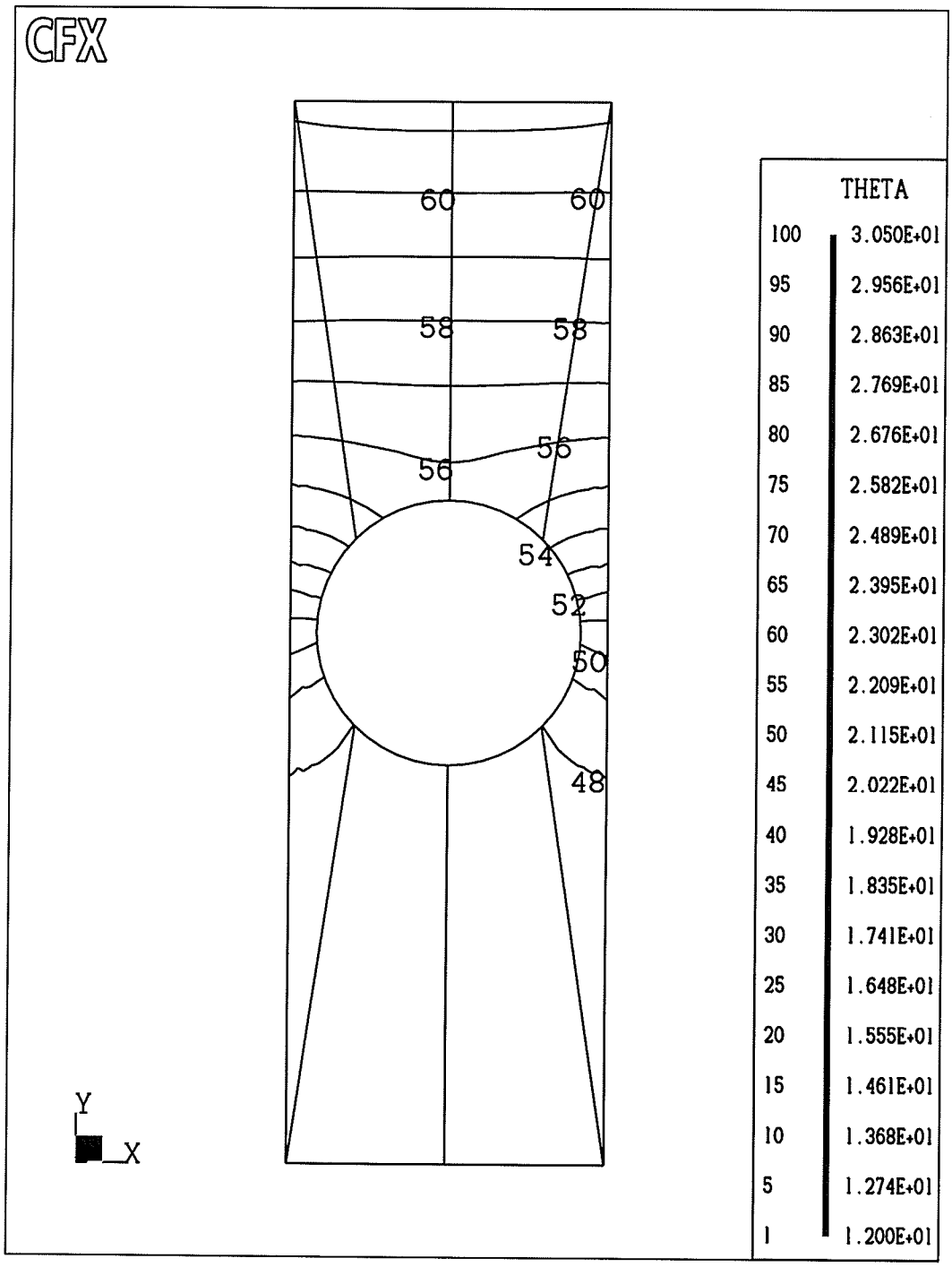

Figure 6.24 Isotherms Near the Outlet of a Microchannel (N=200) with $B/D = 1.2$ and $H/D = 4$, ($Re = 1000$)

Increasing the Reynolds number has very limited effect on the design parameter of surface temperature variation. Figure 6.25 shows that a higher Reynolds number marginally decreases the axial variation of $\overline{\theta_s}$ at the top surface. The total change from inlet to outlet in the Re = 500 case is 1.61 while the Re = 1000 case has a difference of 1.44. It is clear that increasing the Reynolds number decreases the surface temperature. The higher Reynolds number case has a maximum average top surface θ_s of 23.3 compared to 30.3 for the lower Reynolds number case.

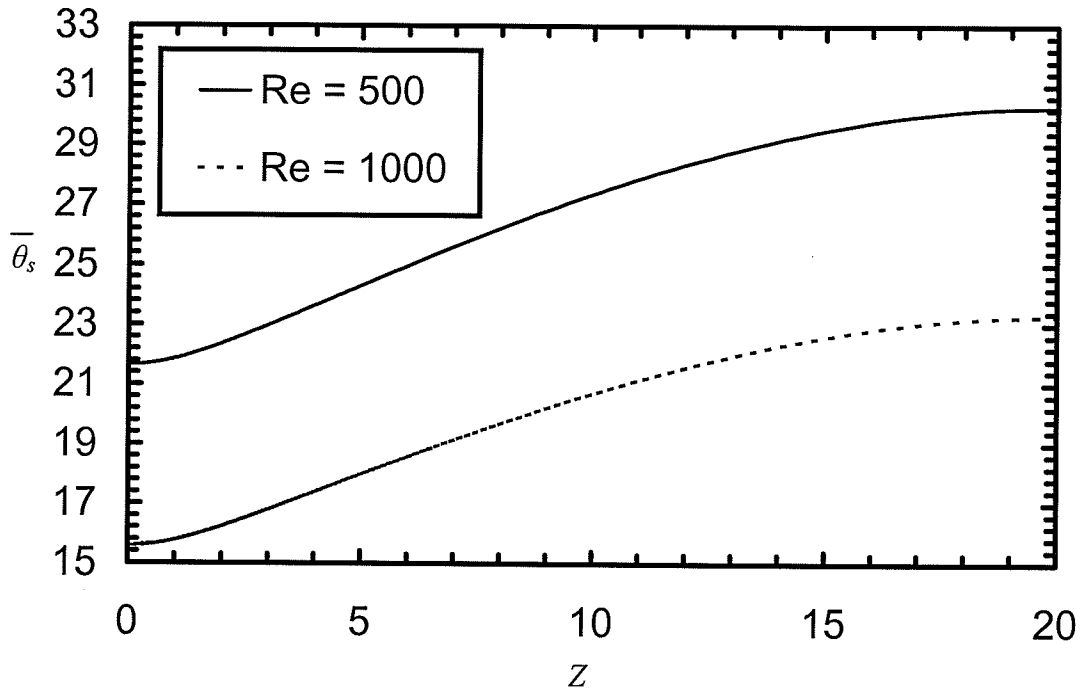

Figure 6.25 Effect of Re on Dimensionless Temperature (Averaged Along X) of the Top Surface of a Heat Sink with H/D = 4 and H/D = 1.2

Figure 6.26 shows that Reynolds number has a marginal effect on axial temperature variation. Qualitatively, when compared to the Re = 500 case in Figure 6.9, the isotherms have very similar spacing throughout the heat sink solid. Both Re = 500 and Re = 1000

heat sinks have approximately the same difference in dimensionless temperature between the bottom and top surfaces (approximately 2.62) in the axial direction in the y-z plane.

The effect of doubling the Reynolds number from 500 to 1000 on the overall thermal resistance of the heat sink is presented in Table 6.3. By comparing these values with those in Table 6.1, we can see that increasing Reynolds number from 500 to 1000 decreases the overall thermal resistance in all cases tested by approximately 30% relative to the $Re = 1000$ values. These percent changes are summarized Table 6.4.

Table 6.3 Dimensionless Heat Sink Overall Thermal Resistance for Various *B/D* and *H/D,* Reynolds Number of 1000, and Copper Heat Sink ($k_s/k_f = 668.3$)

B/D	H/D = 2	H/D = 3	H/D = 4
1.2	1.19	1.17	1.16
1.6	1.52	1.49	1.48
2	1.85	1.81	1.80

Table 6.4 Percentage Decrease in Dimensionless Overall Heat Sink Thermal Resistance Due to Increased Reynolds Number (*Re* = 1000 vs. *Re* = *500*) for Heat Sinks with $k_s/k_f = 668.3$ (Copper-Water)

B/D	H/D = 2	H/D = 3	H/D = 4
1.2	30.8%	30.3%	30.0%
1.6	31.5%	31.2%	31.1%
2	31.8%	31.8%	31.7%

We can define pumping power, or the work needed to move the fluid through the microchannel, in [W], as:

$$P_{WR} = \frac{\dot{m}}{\rho}(P_{inlet} - P_{outlet}) \tag{6.11}$$

Using this definition of pumping power, it was found that the ratio of pumping power required for the *Re = 500* microchannel heat sink to that of *Re = 1000* heat sink to be

0.20. Therefore, even though doubling the Reynolds number in the microchannel produces an approximate 30% decrease in overall thermal conductivity, the same process increases the required pumping power by a factor of 5.

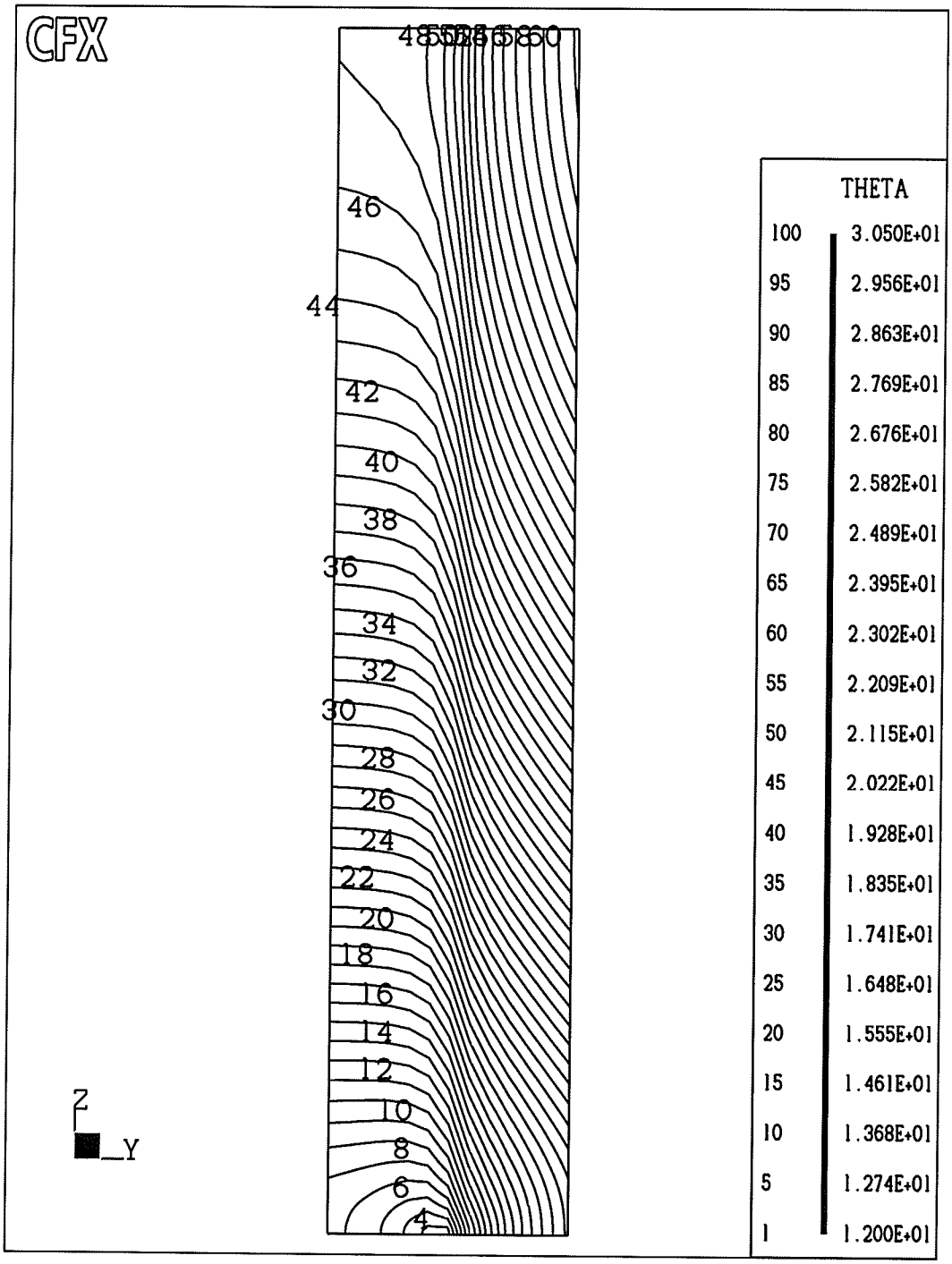

Figure 6.26 Side View of Isotherms Along a Heat Sink with $B/D = 1.2$ and $H/D = 4$, and $Re = 1000$ at Right Symmetry Plane ($X = B/(2D)$)

6.5 Effect of Varying Solid Thermal Conductivity

While increasing the thermal conductivity of the heat sink material is expected to increase the thermal performance, it is not immediately known to what extent this affects heat sinks with circular microchannels. Figures 6.27 to 6.36 show the effects of the thermal conductivity in circular microchannel heat sinks. In all cases, the thermal conductivity is non-dimensionalized by dividing the conductivity of the solid by that of the fluid.

The axial variation of heat input for two different values of k_s/k_f is presented in Figure 6.27 for a single geometry. The rate of heat gain by the fluid is higher for the k_s/k_f = 668.3 ratio at the microchannel inlet but is lower than the k_s/k_f = 247.9 after a Z of about 6. The heat sink with a k_s/k_f of 668.3 experiences higher back-heating than the heat sink with a k_s/k_f = 247.9. Eventually both heat sinks reach a point where the input heat flux is identical, and can be seen as an intersection on the graph.

To better study the effects of dimensionless thermal conductivity changes, the dimensionless temperature results for the varying k_s/k_f cases must be multiplied by k_f/k_s. This operation ensures the results correctly predict the actual physical trends while maintaining a dimensionless analysis. For example, the dimensionless bulk temperature decreases with lower k_s/k_f ratios, as seen in Figure 6.28. The outlet temperatures of the two geometries are not the same due to different thermal conductivities in the heat sink, which is part of the definition of θ, presented in Chapter 3. If the alternate way of plotting the data by multiplying θ_b by k_f/k_s is used, the effect of varying the k_s/k_f ratio on the bulk

temperature along Z can be seen, given the same inlet and outlet bulk temperatures in Figure 6.29. From Eq. (6.4) we see that multiplying θ_b by k_f/k_s does not modify the fixed inlet value, but the fixed outlet value of the bulk temperature becomes:

$$\theta_b = \theta_{b,out} = \frac{\left(\frac{4}{\pi}\right)\left(\frac{L}{D}\right)}{Re\,Pr} \text{ at } Z = L/D \tag{6.12}$$

Figure 6.29 shows that the bulk temperature of the higher k_s/k_f ratio is still higher than that of the lower k_s/k_f ratio, even when using the alternative plotting approach. This is to be expected as a lower thermal conductivity in the solid ensures a higher thermal resistance which hinders heat transfer from the top surface of the heat sink to the fluid in the channel.

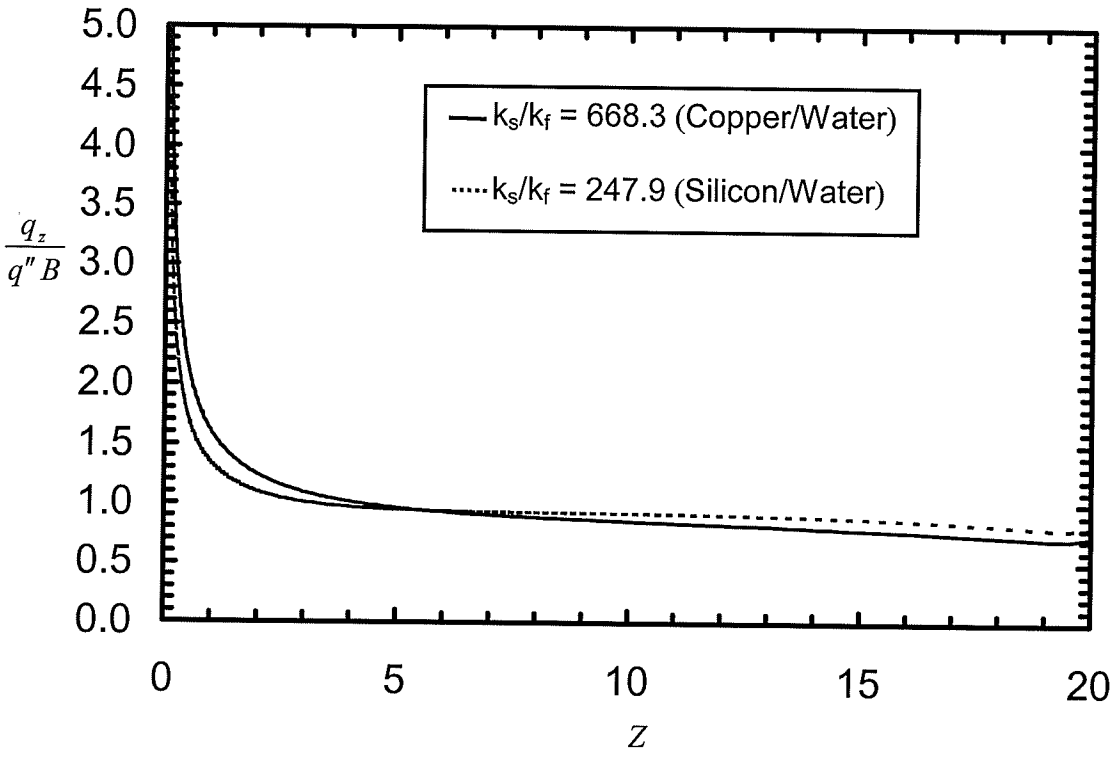

Figure 6.27 Effect of k_s/k_f on the Axial Variation of q_z for $H/D = 4$ and $B/D = 1.2$

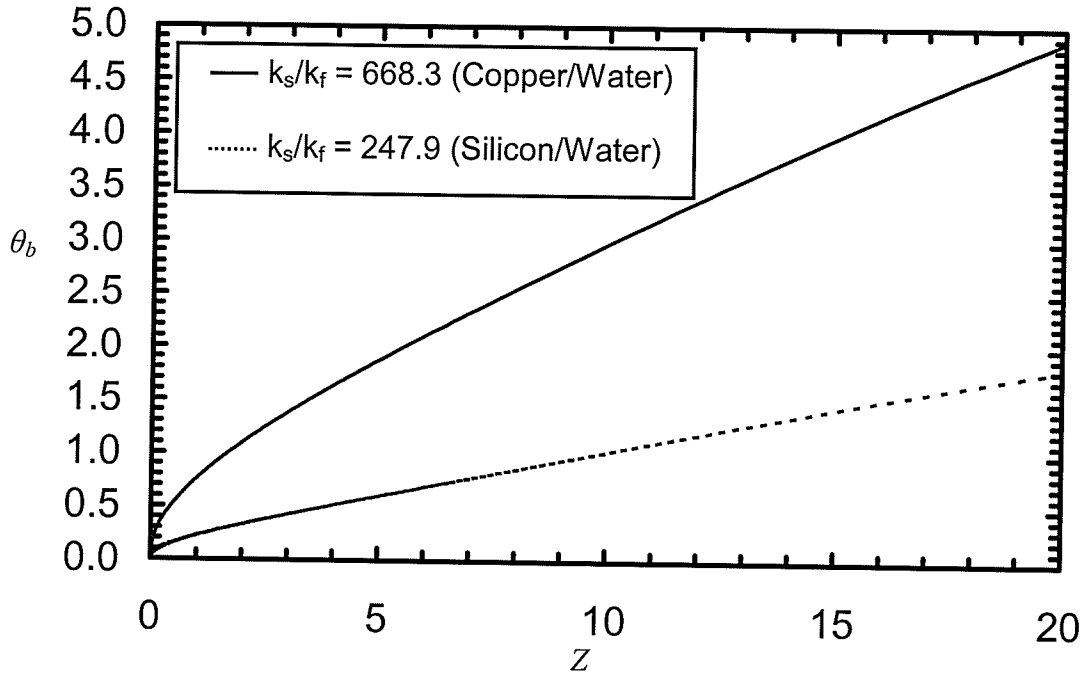

Figure 6.28 Effect of k_s/k_f on θ_b for $H/D = 4$ and $B/D = 1.2$

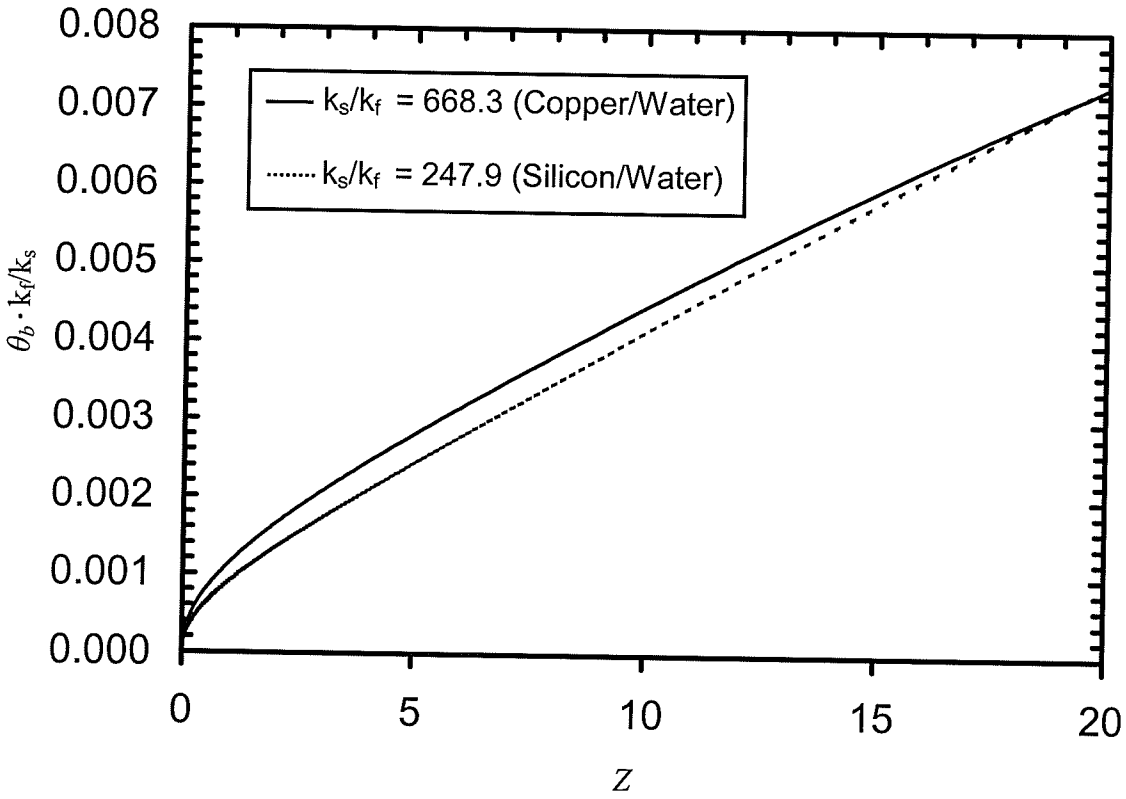

Figure 6.29 Effect of k_s/k_f on $\theta_b \cdot k_f/k_s$ for $H/D = 4$ and $B/D = 1.2$

Figure 6.30 shows the angular variation of the normalized heat flux at the solid-fluid interface along the microchannel. Increasing the k_s/k_f ratio causes a general increase in magnitude of the heat flux ratio at the inlet of the microchannel, which agrees with Figure 6.27. The angular variation of the heat flux does change appreciably with changing thermal conductivity, particularly near the inlet. The k_s/k_f = 668.3 case has a peak-to-trough difference of 4.03, while the k_s/k_f = 247.9 case has a peak-to-trough difference of 6.32. Angular temperature variation and bulk temperature variation for varying k_s/k_f ratios were similar for all geometries analyzed.

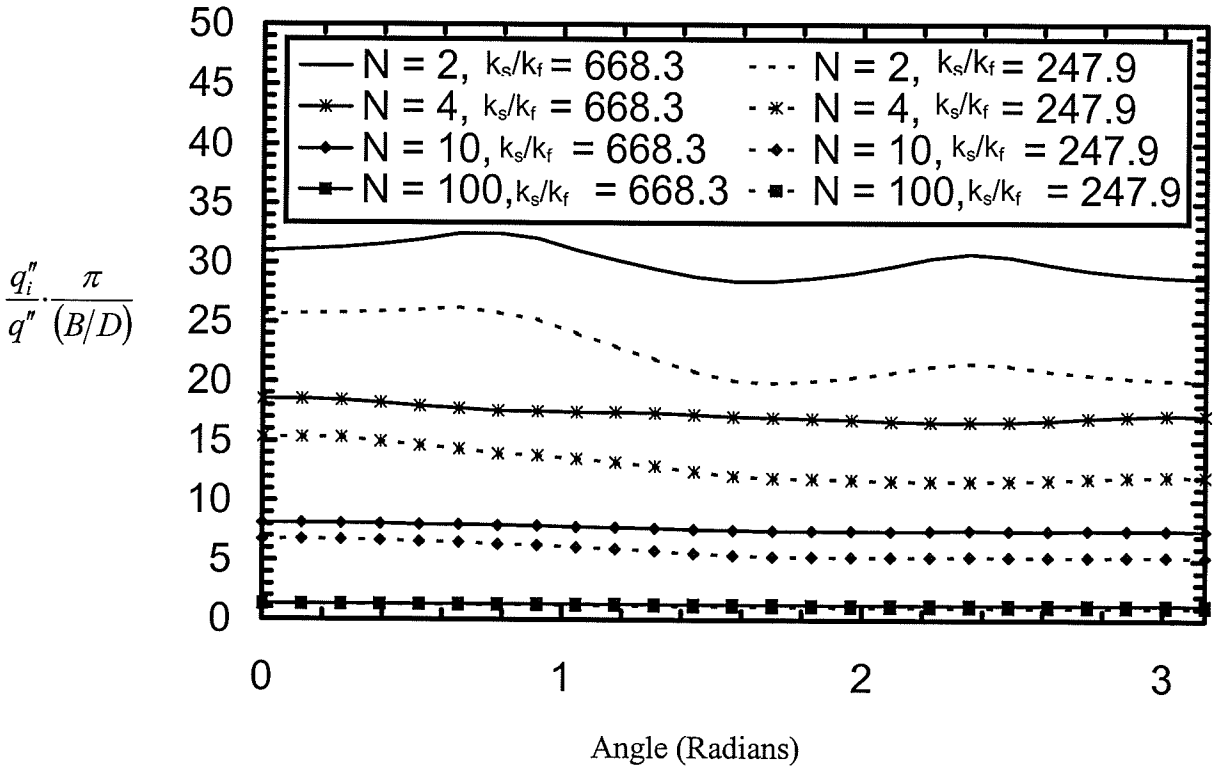

Figure 6.30 Effect of k_s/k_f on Angular Distribution of Input Heat Flux Around a Microchannel at Various Locations Along a Heat Sink with H/D = 4 and B/D = 1.2 (Angle = 0 at Top of Channel)

Figures 6.31 to 6.34 show isotherms of a modified dimensionless temperature (θ_s multiplied by k_f/k_s) in a heat sink along the microchannel near the inlet and near the

outlet for two different k_s/k_f values (copper/water and silicon/water). It is evident that the modified dimensionless temperature is lower in the $k_s/k_f = 247.9$ case near the inlet and near the outlet of the microchannel. At the inlet of the $k_s/k_f = 247.9$ case there is a dimensionless temperature difference of 0.007 between maximum and minimum isotherms compared to 0.004 in the $k_s/k_f = 668.3$ case. This comparison indicates a lower transverse temperature variation in the solid at the inlet for the $k_s/k_f = 668.3$ heat sink. The 0.007 difference in dimensionless temperature in the $k_s/k_f = 247.9$ case is only over approximately half of the heat sink looking at the x-y plane (see Figure 6.31), thus making the temperature difference twice as extreme as it would be if it was spread out from the bottom surface to the top surface. In the $k_s/k_f = 247.9$ case near the inlet, the material below the top of the channel is at a relatively uniform dimensionless temperature of .025, which is due to the lower conductivity of the solid inhibiting heat transfer to all areas.

In Figure 6.32, it is seen that the dimensionless temperature difference between minimum and maximum isotherms at the outlet is approximately .010, which is much higher than the $k_s/k_f = 668.3$ case of 0.004. The fact that the temperature variation at near the inlet and near the outlet of the $k_s/k_f = 247.9$ case is higher than that of the $k_s/k_f = 668.3$ case suggests that increasing the k_s/k_f ratio decreases transverse temperature variation throughout the heat sink solid.

Lines of constant heat flux (not shown) in the $k_s/k_f = 247.9$ case are not similar to the $k_s/k_f = 668.3$ case at the inlet. In this case, heat flux lines indicate that more of the heat

transferred from the top heat sink surface to the fluid flows into the top of the channel. In the $k_s/k_f = 668.3$ case, heat flows into the channel from the sides and from the bottom, similar to the cases mentioned previously. At the outlet, however, the lines of constant heat flux are similar in that lines of constant heat flux turn into the microchannel on the sides and below the channel after travelling straight down from the surface. These trends are similar for both k_s/k_f cases.

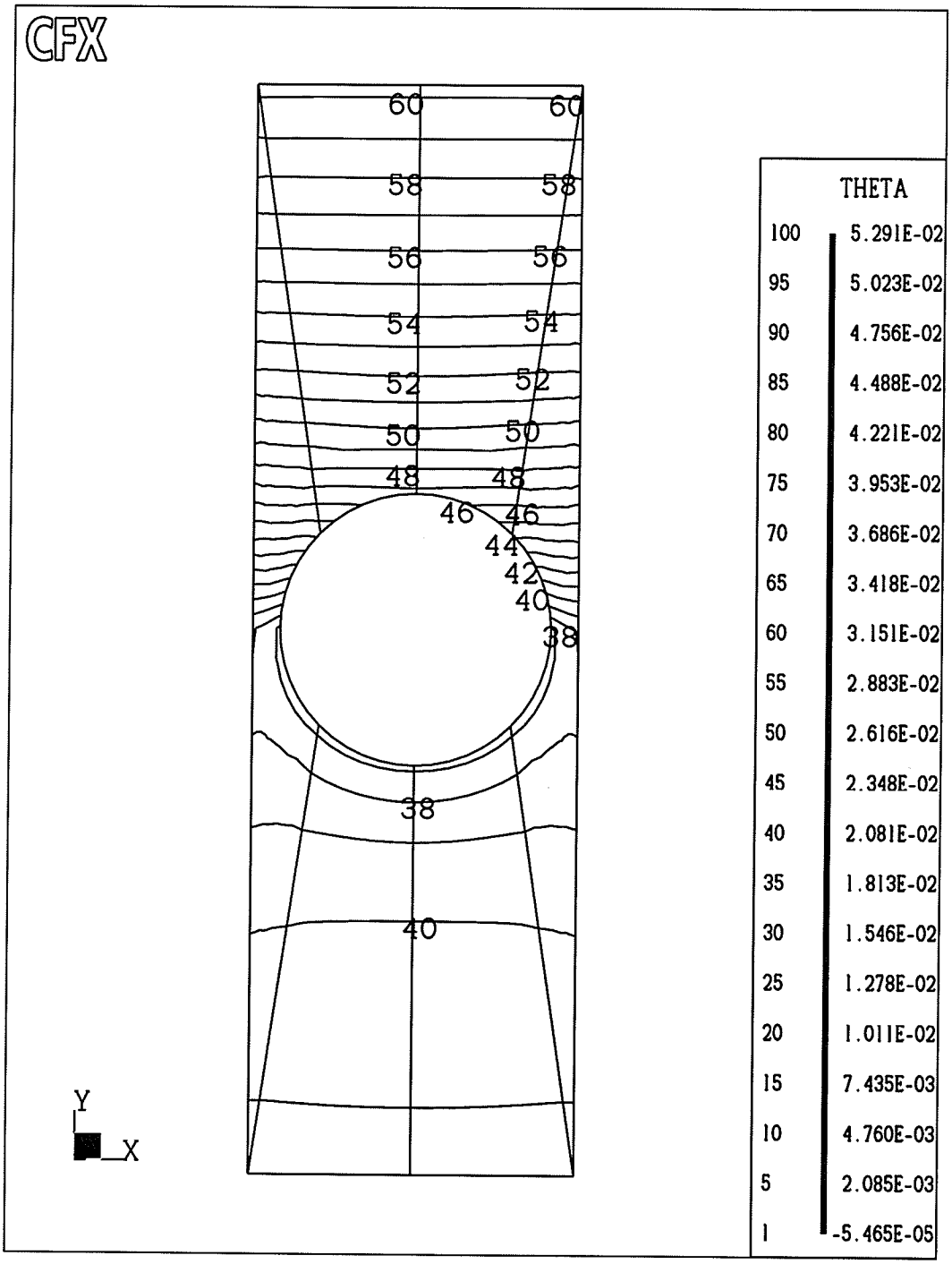

Figure 6.31 Isotherms (θ_s· k_f/k_s) Near the Inlet of a Microchannel (N=10) with B/D = 1.2, H/D = 4, and k_s/k_f = 247.9 (Silicon/Water)

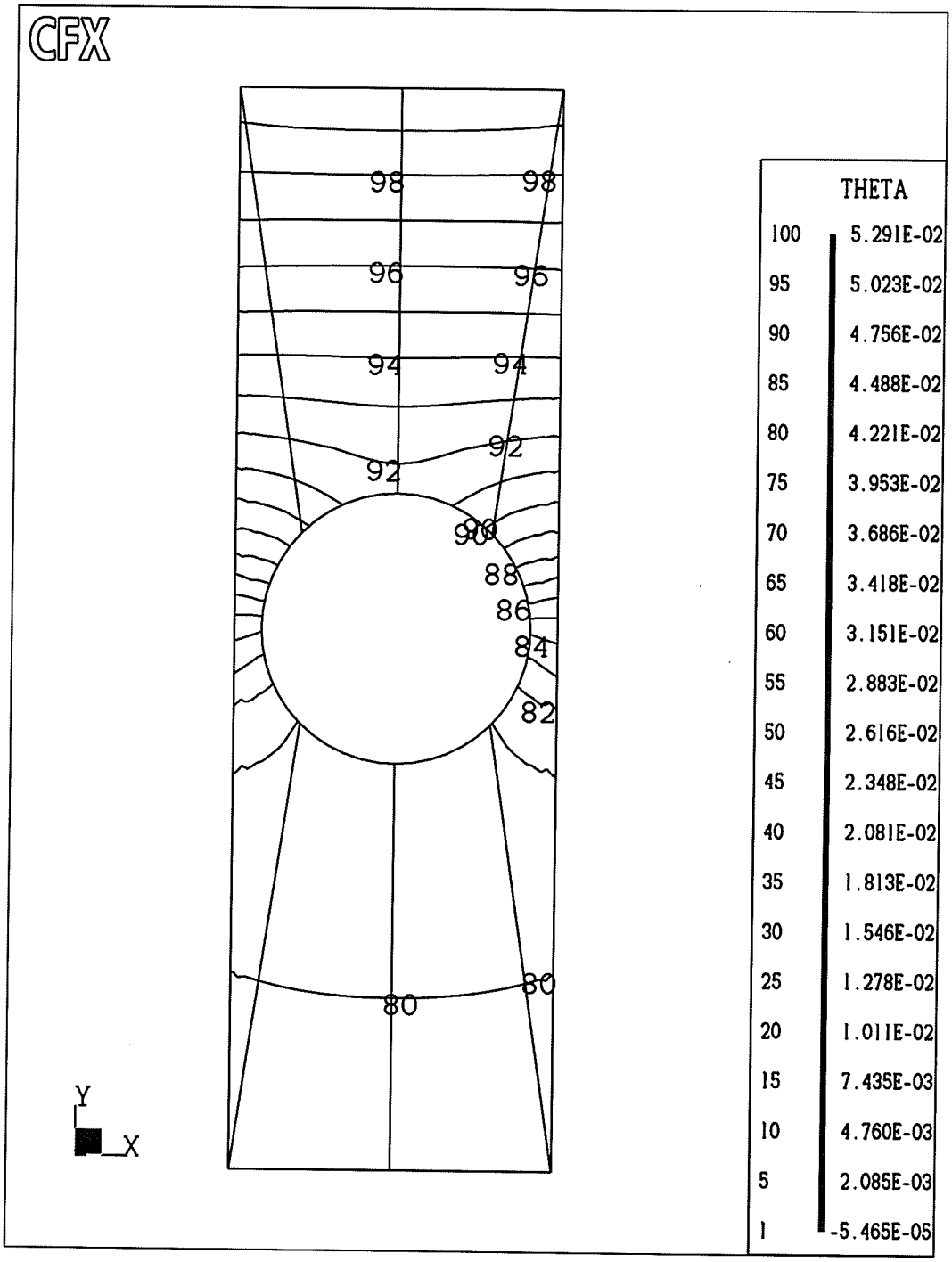

Figure 6.32 Isotherms (θ_s· k_f/k_s) Near the Outlet of a Microchannel (N=200) with B/D = 1.2, H/D = 4, and k_s/k_f = 247.9 (Silicon/Water)

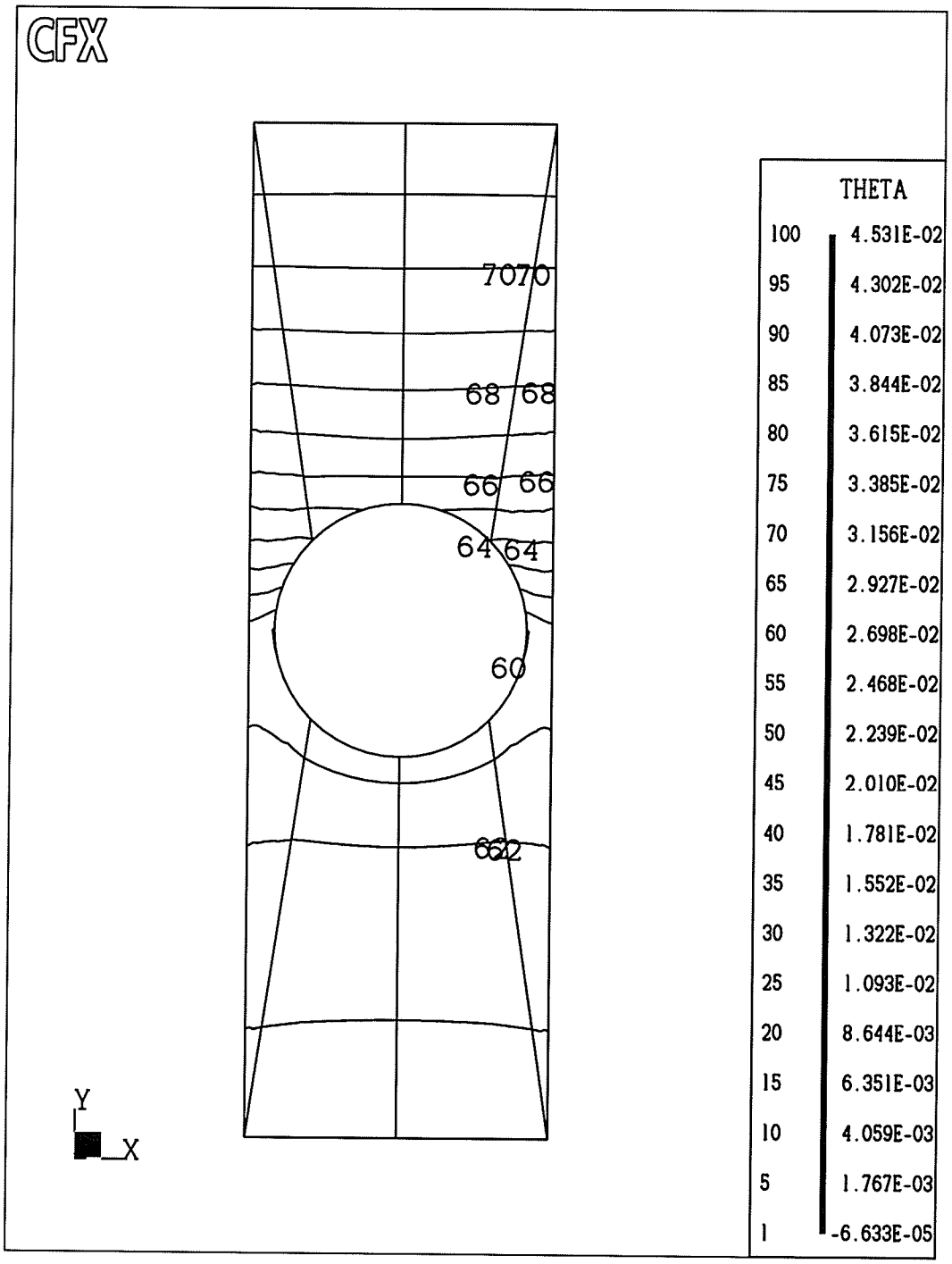

Figure 6.33 Isotherms (θ_s· k_f/k_s) Near the Inlet of a Microchannel (N=10) with B/D = 1.2, H/D = 4, and k_s/k_f = 668.3 (Copper-Water)

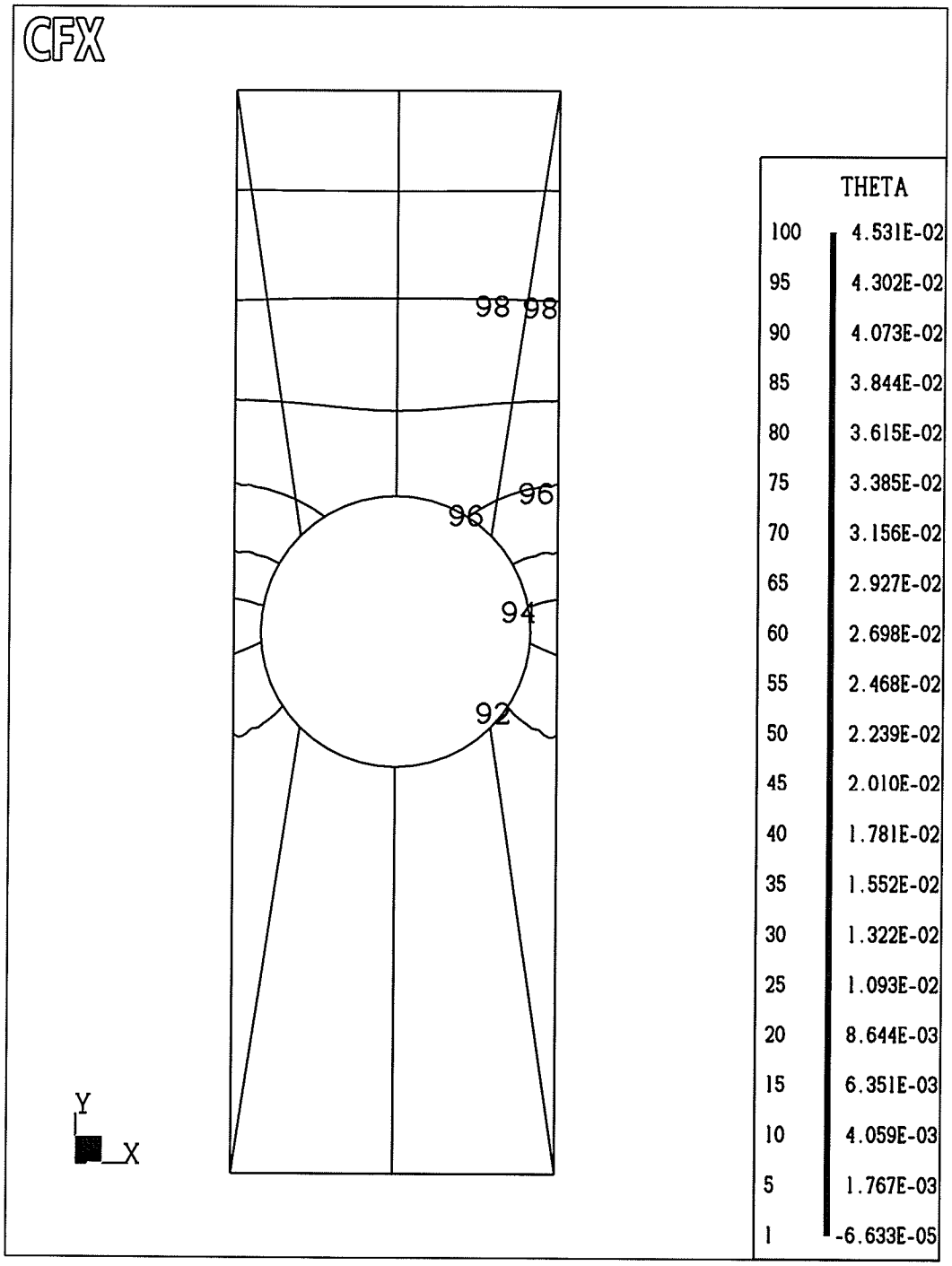

Figure 6.34 Isotherms (θ_s· k_f/k_s) Near the Outlet of a Microchannel (N=200) with B/D = 1.2, H/D = 4, and k_s/k_f = 668.3 (Copper-Water)

Figure 6.35 shows that increasing the k_s/k_f ratio results in a more uniform average temperature distribution along the top surface of the microchannel. The higher k_s/k_f case has a $\overline{\theta_s}$ variation of 0.0129 while the lower case has a variation of 0.0212. The k_s/k_f = 668.3 case has a maximum surface dimensionless temperature of 0.0453. As mentioned above, increasing the k_s/k_f ratio decreases the transverse temperature variation at the microchannel inlet as well. Therefore, if paramount design parameters include top surface constancy and minimal transverse temperature variation in the heat sink, k_s/k_f should be as high as possible.

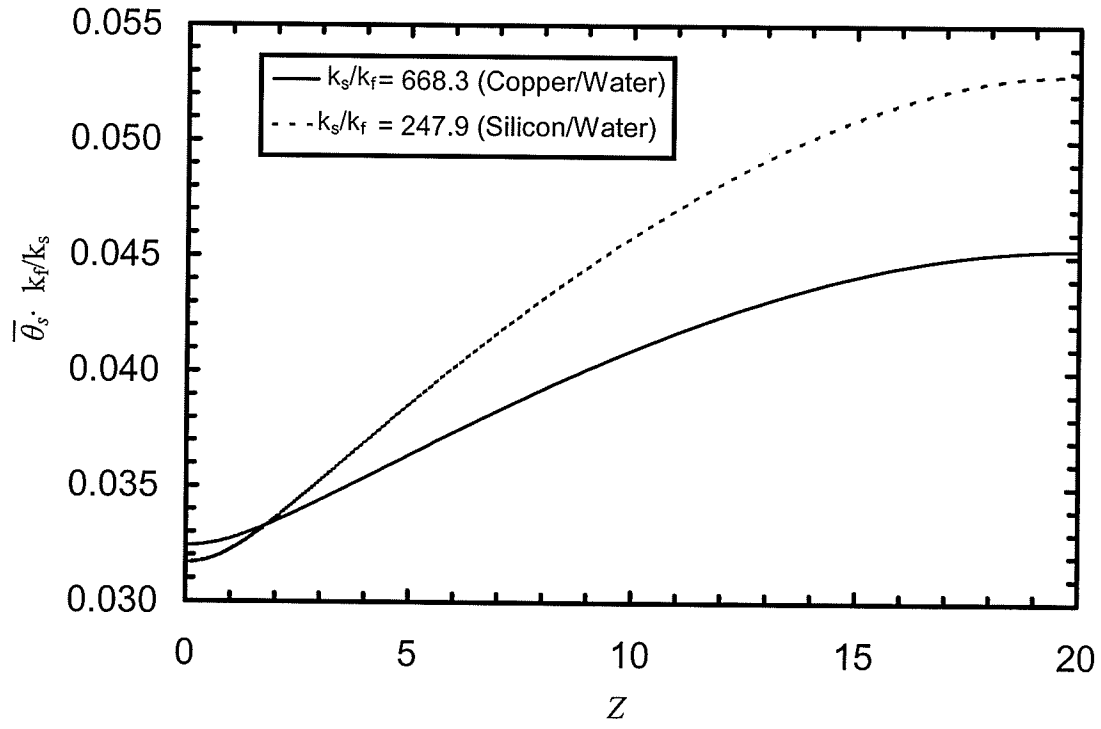

Figure 6.35 Effect of k_s/k_f on $\theta_s \cdot k_f/k_s$ (Averaged Along X) Along the Top Surface of a Heat Sink with H/D = 4 and B/D = 1.2

Figures 6.36 and 6.37 show isotherms of $\theta_s \cdot k_f/k_s$ along heat sinks at the right symmetry plane with a k_s/k_f = 247.9 and a k_s/k_f = 668.3 respectively. Compared to a heat sink with k_s/k_f = 668.3, the k_s/k_f = 247.9 case has much higher temperature variations between the

bottom surface and top surface of the heat sink for the entire length. The inlet θ_s variation for the $k_s/k_f = 247.9$ case is 0.006 compared to 0.004 for the $k_s/k_f = 668.3$ case, and at the outlet, the $k_s/k_f = 247.9$ case has a θ_s variation of 0.009 compared to 0.003 for the $k_s/k_f = 668.3$ case. Qualitatively, the isotherms are much closer together for the $k_s/k_f = 247.9$ case which indicates a much higher temperature variation in the solid.

Table 6.5 shows the effect of varying k_s/k_f on the overall thermal resistance in circular microchannel heat sinks. Due to the definition of Γ^*, a higher dimensionless thermal resistance actually represents lower dimensional thermal resistances. This effect can be seen by starting with Eq. (6.9):

$$\Gamma = \frac{1}{k_s L}\left[\overline{\theta_s\left(Y=\frac{H}{D}, Z=\frac{L}{D}\right)}\right] \tag{6.9}$$

which has units of $\left[\frac{K}{W}\right]$.

Table 6.5 Dimensionless Heat Sink Overall Thermal Resistance for Varying *B/D* and *H/D* for a Silicon Heat Sink ($k_s/k_f = 247.9$)

	Re = 500			*Re* = 1000		
B/D	H/D = 2	H/D = 3	H/D = 4	H/D = 2	H/D = 3	H/D = 4
1.2	0.65	0.65	0.66	0.50	0.51	0.52
1.6	0.81	0.81	0.82	0.62	0.63	0.64
2	0.98	0.98	0.98	0.75	0.76	0.76

A more convenient way of representing the overall thermal resistance which better illustrates the difference between heat sinks with different conductivities is:

$$\Gamma_R = \frac{\Gamma_{copper-water}}{\Gamma_{silicon-water}} = \frac{k_{s,silicon}\left[\overline{\theta_s\left(Y=H/D, Z=L/D\right)}\right]_{copper-water}}{k_{s,copper}\left[\overline{\theta_s\left(Y=H/D, Z=L/D\right)}\right]_{silicon-water}} \tag{6.13}$$

Table 6.6 shows the overall thermal resistance data in this new format. Here we see that as the ratio of the dimensional overall thermal resistance for a $k_s/k_f = 668.3$ heat sink to a $k_s/k_f = 247.9$ heat sink is consistently less than 1. This result shows that as the conductivity of the solid increases, the overall thermal resistance of the heat sink decreases. This phenomenon is to be expected as a higher conductivity in the solid allows easier heat transfer through the solid to the fluid (Incropera and DeWitt, 1996).

Table 6.6 Ratios of Dimensional Thermal Resistance of a $k_s/k_f = 668.3$ (Copper/Water) Heat Sink to a $k_s/k_f =$ 247.9 (Silicon/Water) Heat Sink

	Re = 500			*Re* = 1000		
B/D	H/D = 2	H/D = 3	H/D = 4	H/D = 2	H/D = 3	H/D = 4
1.2	0.90	0.87	0.86	0.88	0.85	0.83
1.6	0.91	0.89	0.88	0.90	0.88	0.86
2	0.92	0.90	0.90	0.91	0.89	0.88

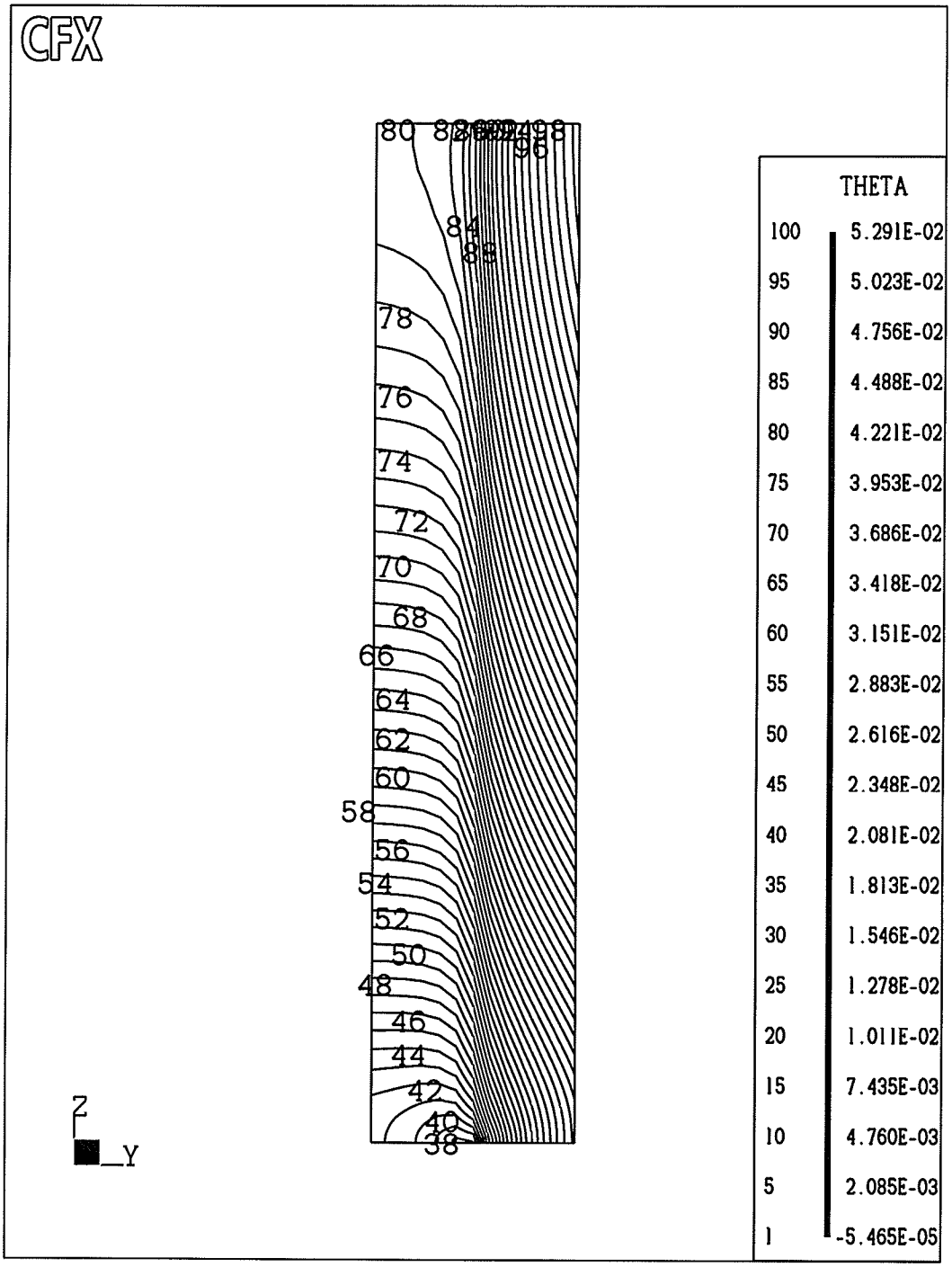

Figure 6.36 Side View of Isotherms ($\theta_s \cdot k_f/k_s$) Along a Heat Sink with $B/D = 1.2$, $H/D = 4$, and $k_s/k_f = 247.9$ (Silicon/Water) at Right Symmetry Plane ($X = B/(2D)$)

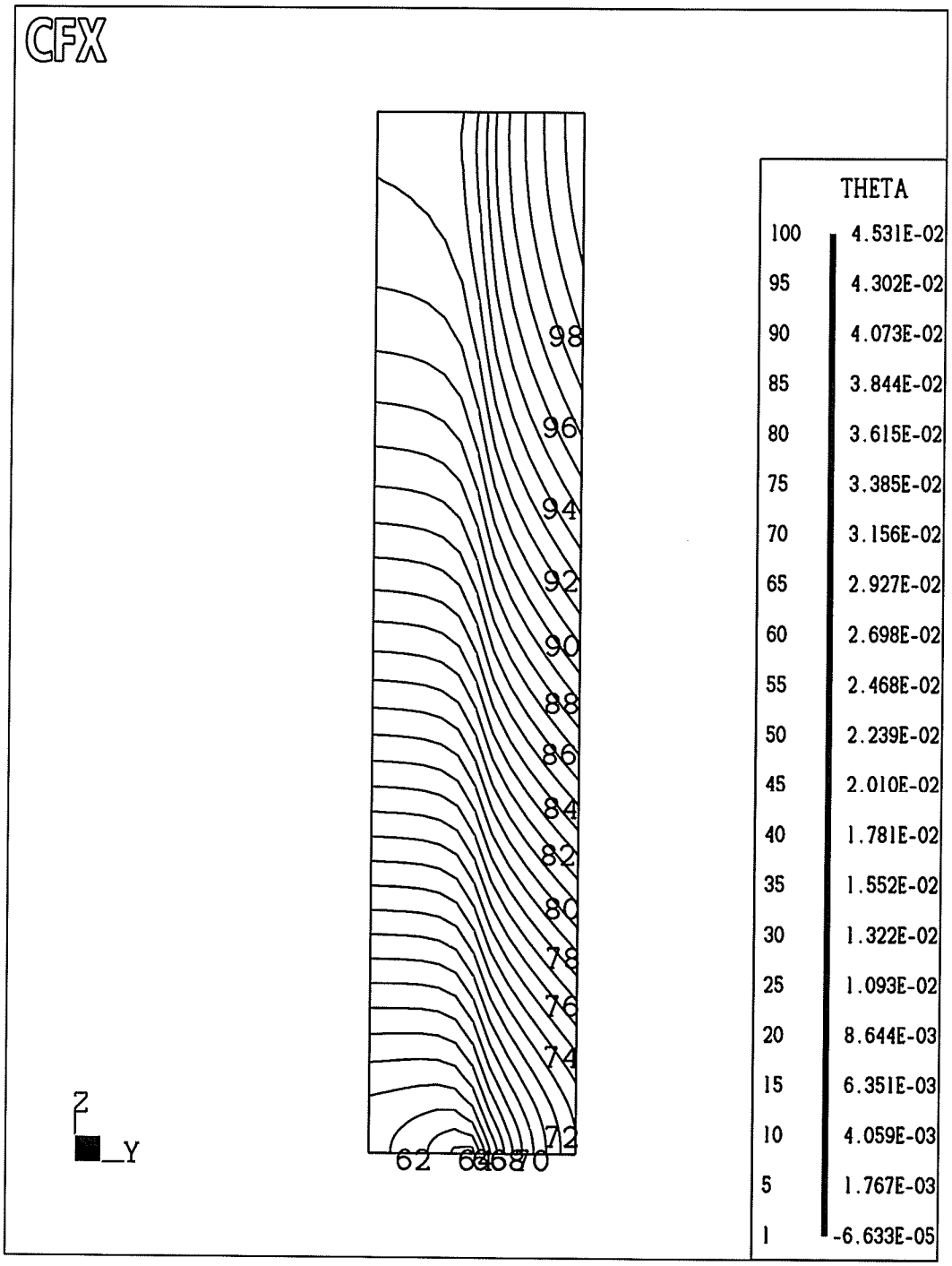

Figure 6.37 Side View of Isotherms (θ_s· k_f/k_s) Along a Heat Sink with $B/D = 1.2$, $H/D = 4$, and $k_s/k_f = 668.3$ (Copper/Water) at Right Symmetry Plane ($X = B/(2D)$)

6.6 Rectangular Microchannel Pumping Power and Overall Thermal Resistance Comparison

As mentioned in Chapter 2, most of the work with microchannels to date has focussed on rectangular geometries. Rectangular microchannels are typically easy to manufacture, which probably accounts for their abundance as well as the abundance of available information. The goal of this section of the thesis is to evaluate the differences between rectangular and circular microchannel geometries in terms of pumping power and overall thermal resistance.

Three different rectangular geometries were compared with one circular microchannel geometry and their general form is outlined in Figure 6.38 with channel width L_1, channel height L_2, and with other parameters similar to Figure 3.2 with conditions listed in Eqs. (6.14) to (6.17). Table 6.7 lists the parameters for each of the rectangular geometries used. The circular microchannel used was case #3 from Table 6.1 (H/D = 4 and B/D = 1.2), and is the circle being referred to in all comparison results.

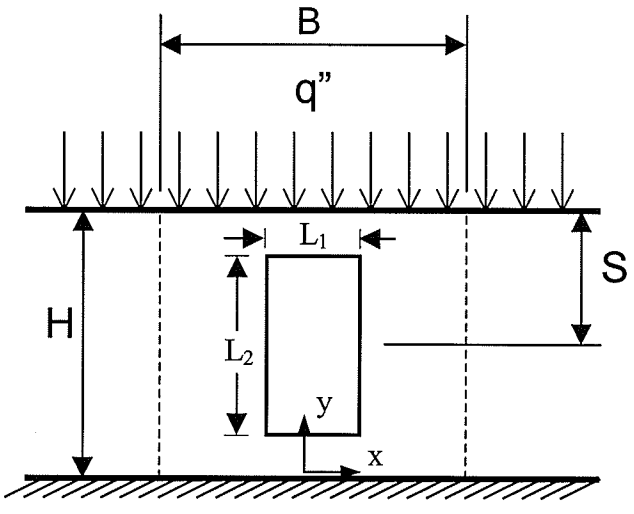

Figure 6.38 Schematic Diagram of a Rectangular Unit Cell

$H = H_{circle}$ for all rectangular geometries (6.14)

$B = B_{circle}$ for all rectangular geometries (6.15)

$S = 0.5H$ (distance from the top of the heat sink to the midpoint of L_2) (6.16)

$$D_h = \frac{4L_1 L_2}{2(L_1 + L_2)} = D_{circle} \quad (6.17)$$

$\alpha = L_2/L_1$ (6.18)

Table 6.7 Parameters for Rectangular Microchannels

Rectangle	L_1	L_2	α
1	D	D	1
2	$2D/3$	$2D$	3
3	$0.6D$	$3D$	5

All rectangular models also had an L/D ratio, Reynolds number, k_s/k_f ratio identical to that of case #3.

The number of nodes in the meshes created for each of the rectangles was equal to or greater than the medium circular microchannel mesh as outlined in Table 5.3. The friction factor fRe was plotted in Figure 6.39 with respect to Z/Re along with accepted data for rectangular channels from Shah and London (1978). These data are presented in Table 6.8. The maximum deviation for all three of the rectangular channels is approximately 17% above values from Table 6.8 at Z/Re = 0.001. This error percentage was considered to indicate adequate agreement with the accepted values.

As seen in section 5.3.1, the grid dependence for temperature required a coarser grid than for the friction factor grid dependence. Thus, it was decided that the meshes for each of

the rectangular geometry cases were acceptable due to the friction factor values being in adequate agreement with Shaw and London (1978).

The meshes used for the rectangular channel geometry were as follows. The mesh for the channel with aspect ratio of 1 had a total of 1351 two-dimensional elements in each cross-section, with a total of 271 551 three-dimensional elements. In the case of the channel with an aspect ratio of 3, in each cross-section there were 1019 two-dimensional elements and a total of 204 819 three-dimensional elements. Finally, the mesh for the channel with an aspect ratio of 5 had a total of 1394 two-dimensional elements in each cross-section, with a total of 280 194 three-dimensional elements.

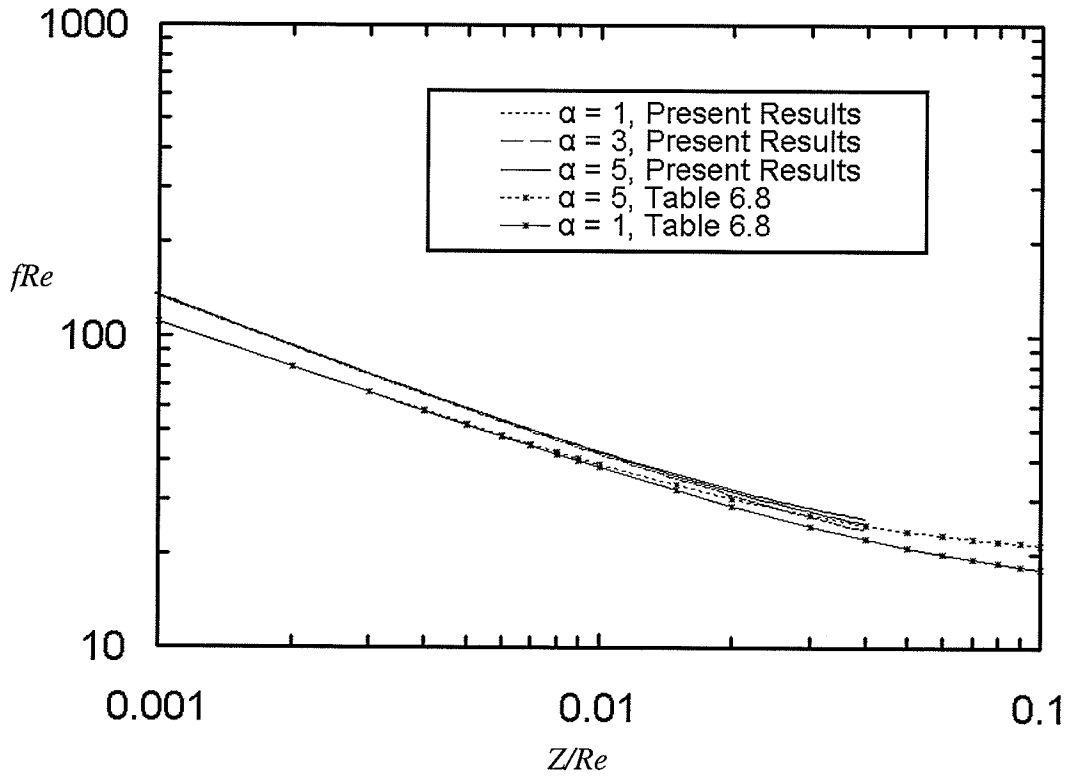

Figure 6.39 Comparison of Predictions for *fRe* as a Function of *Z/Re* for Rectangular Ducts

Table 6.8 Values of fRe with Varying Z/Re for Rectangular Channels with Various Aspect Ratios, as Reported in Shah and London (1978)

Z/Re	$\alpha = 1$	$\alpha = 5$
0.001	111.0	111.0
0.002	80.2	80.2
0.003	66.0	66.1
0.004	57.6	57.9
0.005	51.8	52.5
0.006	47.6	48.4
0.007	44.6	45.3
0.008	41.8	42.7
0.009	39.9	40.6
0.010	38.0	38.9
0.015	32.1	33.3
0.020	28.6	30.2
0.030	24.6	26.7
0.040	22.4	24.9
0.050	21.0	23.7
0.060	20.0	22.9
0.070	19.3	22.4
0.080	18.7	22.0
0.090	18.2	21.7
0.100	17.8	21.4

Using Eq. (6.11), the pumping power required for each rectangular microchannel case can be compared with that of the corresponding circular microchannel case. Overall thermal resistance for the rectangular channels can still be defined using Eq. (6.9) and compared with the circular microchannel results if it is still assumed that an entire microchannel heat sink consists of 12 channels ($B_T/D = 24$).

Figure 6.40 shows both the ratios of overall thermal resistance of a rectangular channel to a circular channel as well as the ratio of pumping power for a rectangular channel to a circular channel. Because the circular value is constant (case #3), these curves show the trends of the rectangular channel directly. It is evident from this figure that while the overall thermal resistance of a rectangular microchannel decreases approximately linearly (within the aspect ratios of 1 to 5) with aspect ratio, the pumping power increases almost linearly (within the aspect ratios of 1 to 5) with aspect ratio. An optimal point exists at an aspect ratio of approximately 3.5 where a minimum overall thermal resistance is achieved with a minimum amount of pumping power for a rectangular microchannel. Under equal conditions of Reynolds number, heat sink thermal conductivity and hydraulic diameter, a rectangular microchannel geometry will deliver a lower overall thermal resistance than a circular microchannel; however, a circular microchannel will require less pumping power.

Figure 6.41 shows the ratio of heat flux input to pumping power required for a circular microchannel to that of a rectangular microchannel. From the curve we can see that a circular microchannel will allow more heat transfer per unit pumping power than a rectangular microchannel, given the same hydraulic diameter and Reynolds number.

The above comparison between rectangular and circular microchannels indicates that the selection of either geometry should be based on the design requirement. If pumping power is of no concern due to an inexpensive supply or overabundance, then a rectangular geometry should be chosen as it would deliver a lower overall thermal

resistance to the heat sink. If pumping power is of concern, then selecting a circular microchannel geometry would be the better choice as more heat can be input to the fluid per unit of pumping power than a rectangular microchannel of equal hydraulic diameter operating with the same boundary conditions.

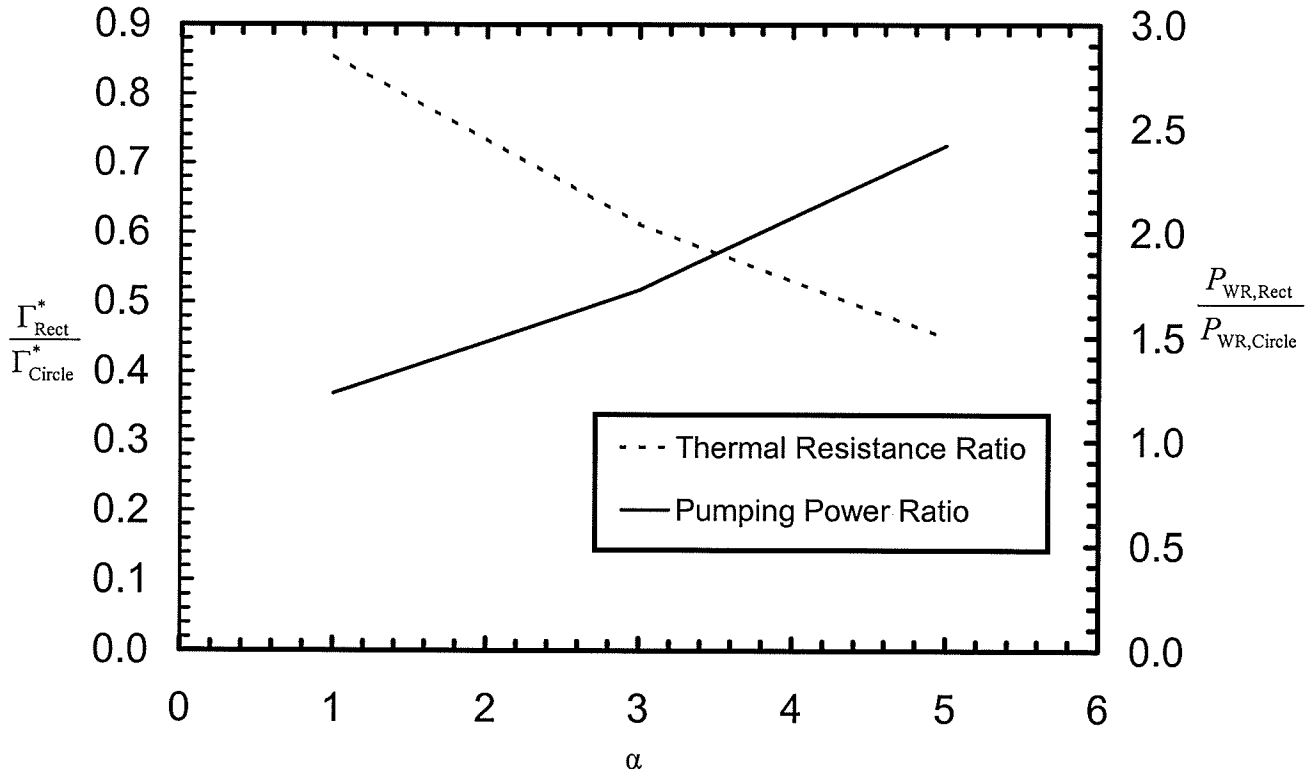

Figure 6.40 Overall Rectangular Channel Thermal Resistance to Overall Circular Channel Thermal Resistance Ratio and Rectangular Channel Pumping Power to Circular Channel Pumping Power Ratio for Various Rectangular Channel Aspect Ratios

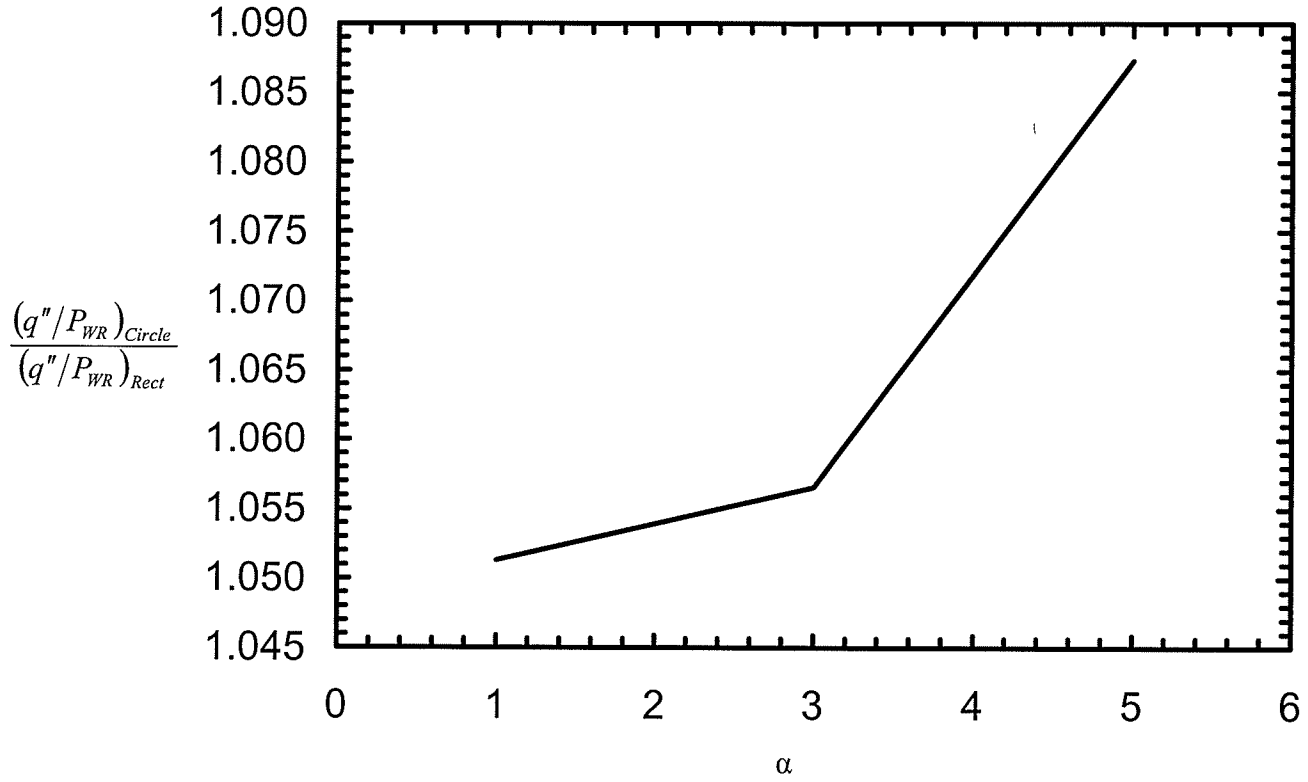

Figure 6.41 Input Heat Flux to Pumping Power Ratio for Circular Channels over Input Heat Flux to Pumping Power Ratio for Rectangular Channels for Various Rectangular Channel Aspect Ratios

Chapter 7

SUMMARY, CONCLUSIONS, AND RECOMMENDATIONS

7.1 Summary

A numerical analysis was conducted in order to solve for the temperature, heat flux, fluid velocity, and pressure distributions in three dimensional microchannel heat sinks with circular and rectangular shaped channels. The effects of numerous geometric parameters on thermal performance and other design features (e.g. surface temperature, bulk temperature, and temperature variation in the heat sink solid) were studied in detail for the circular geometry. Developing flow in the microchannel was assumed, and good agreement between code predictions and experimental data for both rectangular and circular microchannels were achieved. Rectangular microchannel heat sinks of various aspect ratios were compared to circular microchannel heat sinks by analyzing the pumping power and thermal performance under the same conditions of hydraulic diameter and Reynolds number.

This thesis presents new conjugate, three-dimensional, developing flow analyses of circular microchannel heat sinks and presents performance data in dimensionless form to facilitate its use over a wide range of design cofigurations. This thesis also contributes to the knowledge of the applicability of the Navier-Stokes equations to microchannel analyses.

7.2 Conclusions

The following conclusions were drawn for the circular microchannel geometry:

1. Decreasing the *B/D* ratio significantly decreases the overall thermal resistance of a heat sink, indicating that the ideal heat sink would have a web thickness as close to zero as possible; however, manufacturability is a limiting factor. A trade-off occurs with decreased thermal resistance in that smaller *B/D* ratios result in higher transverse temperature variations in the heat sink solid and higher temperature variations at the surface. Lower rates of back-heating and lower bulk temperature are also associated with decreased *B/D* values.

2. Increasing the *H/D* ratio marginally decreases the thermal resistance of the heat sink. Increasing this ratio results in lower axial temperature variation in the solid, while increasing transverse solid temperature variation. Larger values of *H/D* also create a more uniform heat sink surface temperature. Other trends with increasing *H/D* include higher rates of back-heating and higher bulk temperatures.

3. Increasing the Reynolds number significantly reduces the thermal resistance of the heat sink. Heat sink channels with higher values of *Re* also have higher Nusselt numbers, lower rates of back-heating, and lower bulk temperatures. Reynolds number has little effect on temperature variation at the surface of the heat sink and throughout the solid itself.

4. Increasing the k_s/k_f ratio decreases the heat sink thermal resistance. Higher values of k_s/k_f also produce lower temperature variations at the heat sink surface and transverse

temperature variations in the solid overall. Back-heating rates and bulk temperature both increase with increasing k_s/k_f ratios.

5. From conclusions 1 and 2 we can conclude that higher rates of back-heating occur with larger heat sink volumes.

6. From conclusions 1 through 4 we can conclude that the amount of back-heating in the microchannel is not indicative of the microchannel overall thermal resistance.

It was also concluded that under equal operating conditions (for Reynolds number and hydraulic diameter), heat sinks with rectangular microchannels have less thermal resistance than those with circular microchannels. Heat sinks with rectangular microchannels also have lower thermal resistance with increasing aspect ratio. Under the same operating conditions, however, heat sinks with circular microchannels require less pumping power per unit of heat removed by the fluid.

7.3 Recommendations

Recommendations for future work with microchannel heat exchangers with circular channels are as follows:

1. Experimental verification of the results produced in this thesis.
2. Study the effect of turbulent flow in circular microchannels with varying geometries.
3. Study the effect of two-phase flow in circular microchannels with varying geometries.

4. Extend the data produced in this thesis to microchannels with larger *L/D* ratios.
5. Develop Nusselt number correlations that account for k_s/k_f, *Re,* and varying geometries.

REFERENCES

Adams, T.M., Abdel-Khalik, S.I., Jeter, S.M., and Qureshi, Z.H., 1998, An Experimental Investigation of Single-Phase Forced Convection in Microchannels, *International Journal of Heat and Mass Transfer,* Vol. 41, pp. 851-857.

Ambatipudi, K.K., and Rahman, M.M., 2000, Analysis of Conjugate Heat Transfer in Microchannel Heat Sinks, *Numerical Heat Transfer, Part A,* Vol. 37, pp. 711-731.

Ameel, T.A., Wang, X., Barron, R.F., and Warrington, Jr., R.O., 1997, Laminar Forced Convection in a Circular Tube With Constant Heat Flux and Slip Flow, *Microscale Thermophysical Engineering,* Vol. 1, pp. 303-320.

ASHRAE, 1976, *Thermophysical Properties of Refrigerants*, ASHRAE Inc., New York.

Bowers, M.B., and Mudawar, I., 1994, High Flux Boiling in Low Flow Rate, Low Pressure Drop Mini-Channel and Micro-Channel Heat Sinks, *International Journal of Heat and Mass Transfer,* Vol. 37, pp. 321-332.

Fedorov, A.G., and Viskanta, R., 2000, Three-Dimensional Conjugate Heat Transfer in the Microchannel Heat Sink for Electronic Packaging, *International Journal of Heat and Mass Transfer,* Vol. 43, pp. 399-415.

Gao, P., Le Person, S., and Favre-Marinet, M., 2002, Scale Effects on Hydrodynamics and Heat Transfer in Two-Dimensional Mini and Microchannels, *International Journal of Thermal Sciences,* Vol. 41, pp. 1017-1027.

Guo, Z.Y., and Li, Z.X., 2003, Size Effect on Microscale Single-Phase Flow and Heat Transfer, *International Journal of Heat and Mass Transfer,* Vol. 46, pp. 149-159.

Incropera, F.P., and DeWitt, D.P., 1996, *Fundamentals of Heat and Mass Transfer* Fourth Edition, John Wiley & Sons Inc., New York.

Kandlikar, S.G., and Grande, W.J., 2003, Evolution of Microchannel Flow Passages – Thermohydraulic Performance and Fabrication Technology, *Heat Transfer Engineering,* Vol. 24 No. 1, pp. 3-17.

Kawano, K., Minakami, K., Iwasaki, H., and Ishizuka, M., 1998, Micro Channel Heat Exchanger for Cooling Electrical Equipment, *Application of Heat Transfer in Equipment, Systems, and Education,* ASME HTD-Vol. 361-3/PID-Vol. 3, pp. 173-180.

Kroeker, C.J., Soliman, H.M., and Ormiston, S.J., 2003, Three-Dimensional Thermal Analysis of Heat Sinks With Circular Cooling Micro-Channels, *ASME Proceedings of the First International Conference on Microchannels and Minichannels,* Rochester N.Y., pp. 731-738.

Obot, N.T., 2002, Toward a Better Understanding of Friction and Heat/Mass Transfer in Microchannels – A Literature Review, *Microscale Thermophysical Engineering,* Vol. 6, pp. 155-173.

Owhaib, W., and Palm, B., 2003, Experimental Investigation of Single-Phase Convective Heat Transfer in Circular Microchannels, *Experimental Thermal and Fluid Science*, To Appear.

Patankar, S.V., 1980, *Numerical Heat Transfer and Fluid Flow,* Hemisphere Publishing Corporation, New York.

Prakash, C., and Patankar, S.V., 1985, A Control-Volume-Based Finite-Element Method for Solving the Navier-Stokes Equations Using Equal-Order Velocity-Pressure Interpolation, *Numerical Heat Transfer*, Vol. 8, pp. 259-280.

Qu, W., and Mudawar, I., 2002, Analysis of Three-Dimensional Heat Transfer in Micro-Channel Heat Sinks, *International Journal of Heat and Mass Transfer,* Vol. 45, pp. 3973-3985.

Ryu, J.H., Choi, D.H., and Kim, S.J., 2002, Numerical Optimization of the Thermal Performance of a Microchannel Heat Sink, *International Journal of Heat and Mass Transfer,* Vol. 45, pp. 2823-2827.

Schneider, G.E., and Raw, M.J., 1987, Control-Volume Finite-Element Method for Heat Transfer and Fluid Flow Using Co-located Variables – 1. Computational Procedure, *Numerical Heat Transfer,* Vol. 11, pp. 363-390.

Shah, R.K., and London, A.L., 1978, *Laminar Flow Forced Convection in Ducts,* Academic Press, New York.

Toh, K.C., Chen, X.Y., and Chai, J.C., 2002, Numerical Computation of Fluid Flow and Heat Transfer in Microchannels, *International Journal of Heat and Mass Transfer,* Vol. 45, pp. 5133-5141.

Tuckerman, D.B., 1984, Heat Transfer Microstructures for Integrated Circuits, Ph.D. Thesis, Stanford University, Stanford, California.

Tunc, G., and Bayazitoglu, Y., 2002, Heat Transfer in Rectangular Microchannels, *International Journal of Heat and Mass Transfer,* Vol. 45, pp. 765-773.

Appendix A

THERMOPHYSICAL PROPERTIES

A.1 Water Properties

Source: CFX-TASCflow Internal Library. Properties @ 290 K and 101.3 kPa.

$k = 0.597$ [W/m K] $\rho = 998.2$ [kg/m^3]

$Cp = 4182$ [J/kg K] $\mu = 0.000993$ [N s/m^2]

$Cv = 4182$ [J/kg K]

A.2 Copper Properties

Source: CFX-TASCflow Internal Library. Properties @ 300 K.

$k = 399$ [W/m K]

$Cp = 383$ [J/kg K]

$\rho = 8933$ [kg/m^3]

A.3 Silicon Properties

Source: Incropera and DeWitt (1996). Properties @ 300K.

$k = 148$ [W/m K]

$Cp = 712$ [J/kg K]

$\rho = 2330$ [kg/m^3]

A.4 Nickel Properties

Source: Incropera and DeWitt (1996). Properties @ 300K.

$k = 90.7$ [W/m K]

$Cp = 444$ [J/kg K]

$\rho = 8900$ [kg/m^3]

A.5 R-113 Properties

Source: ASHRAE (1976). Properties @ 311K.

$k = 0.0753$ [W/m K]

$Cp = 971$ [J/kg K]

$Cv = 971$ [J/kg K]

$\rho = 1531$ [kg/m^3]

$\mu = 0.000586$ [N s/m^2]

Appendix B

CFX-TASCflow PARAMETERS

The following parameters were modified as shown to create converged solutions for the 36 cases as described in Chapter 5:

- ERTIME = 1.0 x 10^{-7} (maximum value of the sum of the absolute dimensionless residuals of the discretized equations)
- DTIME_CHT_SOLID = 1 (time step in solid)
- ISKEW = 3 (modified linear profile with physical advection correction)
- RELAX_BC_AP = 0.6 (relaxation normal component of momentum [wall, symmetry])
- RLXBND = 0.25 (boundary condition relaxation factor)
- RELAX_PTOTAL = 0.75 (relaxation for total pressure inlet)
- TIMESTEP_CHOICE = 1 (fluid time step)
- RELAX_MASS = 0.5 (mass relaxation for solver)
- KNTIME = 1000 (maximum number of iterations – never reached for the cases studied, typical number of iterations to convergence was <100)

Appendix C

RELATIONSHIP BETWEEN N AND z/L

N	z/L
1	0.000000
2	0.000224
3	0.000460
4	0.000702
5	0.000950
6	0.001203
7	0.001462
8	0.001728
9	0.002000
10	0.002278
11	0.002562
12	0.002853
13	0.003151
14	0.003456
15	0.003768
16	0.004088
17	0.004415
18	0.004749
19	0.005091
20	0.005442
21	0.005800
22	0.006167
23	0.006543
24	0.006927
25	0.007321
26	0.007723
27	0.008135
28	0.008557
29	0.008988
30	0.009430
31	0.009882
32	0.010345
33	0.010818
34	0.011302
35	0.011798
36	0.012306
37	0.012825
38	0.013356
39	0.013900
40	0.014457
41	0.015027
42	0.015609
43	0.016206
44	0.016817
45	0.017442
46	0.018081
47	0.018736
48	0.019405
49	0.020091
50	0.020792
51	0.021510
52	0.022245
53	0.022997
54	0.023767
55	0.024554
56	0.025360
57	0.026185
58	0.027030
59	0.027894
60	0.028778
61	0.029683
62	0.030609
63	0.031557
64	0.032526
65	0.033519
66	0.034535
67	0.035575
68	0.036639
69	0.037728
70	0.038842
71	0.039983
72	0.041150
73	0.042345

N	z/L
74	0.043567
75	0.044818
76	0.046099
77	0.047409
78	0.04875
79	0.050123
80	0.051527
81	0.052965
82	0.054436
83	0.055942
84	0.057482
85	0.059059
86	0.060673
87	0.062325
88	0.064015
89	0.065745
90	0.067515
91	0.069327
92	0.071181
93	0.073079
94	0.075021
95	0.077009
96	0.079043
97	0.081124
98	0.083255
99	0.085435
100	0.087667
101	0.08995
102	0.092287
103	0.094679
104	0.097127
105	0.099632
106	0.102195
107	0.104819
108	0.107504
109	0.110252
110	0.113065
111	0.115943
112	0.118888
113	0.121903
114	0.124988
115	0.128145
116	0.131377
117	0.134684
118	0.138068
119	0.141531
120	0.145076
121	0.148704
122	0.152416
123	0.156216
124	0.160104
125	0.164083
126	0.168156
127	0.172324
128	0.17659
129	0.180955
130	0.185423
131	0.189995
132	0.194674
133	0.199463
134	0.204364
135	0.209379
136	0.214512
137	0.219766
138	0.225142
139	0.230644
140	0.236275
141	0.242037
142	0.247935
143	0.253971
144	0.260148
145	0.266469
146	0.272939

N	z/L
147	0.27956
148	0.286336
149	0.293271
150	0.300368
151	0.307631
152	0.315064
153	0.322672
154	0.330457
155	0.338425
156	0.346579
157	0.354924
158	0.363464
159	0.372205
160	0.38115
161	0.390304
162	0.399673
163	0.409261
164	0.419074
165	0.429116
166	0.439393
167	0.449911
168	0.460676
169	0.471692
170	0.482966
171	0.494504
172	0.506312
173	0.518397
174	0.530765
175	0.543422
176	0.556375
177	0.569632
178	0.583199
179	0.597084
180	0.611293
181	0.625836
182	0.640719
183	0.65595
184	0.671538
185	0.687491
186	0.703817
187	0.720525
188	0.737625
189	0.755125
190	0.773035
191	0.791364
192	0.810122
193	0.829319
194	0.848966
195	0.869073
196	0.88965
197	0.910709
198	0.932261
199	0.954318
200	0.976891
201	0.999993